N°d'ordre NNT : 2020LYSEI022

THESE de DOCTORAT DE L'UNIVERSITE DE LYON
opérée au sein de
L'Institut National des Sciences Appliquées de Lyon

Ecole Doctorale 160
Électronique, Électrotechnique, Automatique

Spécialité/ discipline de doctorat :
Traitement du Signal et de l'Image

Soutenue publiquement/à huis clos le 24/03/2020, par :
Pei NIU

Multi-energy image reconstruction in spectral photon-counting CT

Devant le jury composé de :

HELBERT David	Habilité à diriger des recherches, Univ Poitiers	Rapporteur
DESVIGNES Michel	Professeur, Grenoble INP	Rapporteur
USSON Yves	Chargé de Recherche CNRS, Grenoble Alpes	Examinateur
KAFTANDJIAN Valérie	Professeur, INSA Lyon	Examinatrice
DUVAUCHELLE Philippe	Maître de Conférences, INSA Lyon	Examinateur
ZHU Yuemin	Directeur de Recherche CNRS, INSA Lyon	Directeur de thèse

Département FEDORA – INSA Lyon - Ecoles Doctorales – Quinquennal 2016-2020

SIGLE	ECOLE DOCTORALE	NOM ET COORDONNEES DU RESPONSABLE
CHIMIE	**CHIMIE DE LYON** **http://www.edchimie-lyon.fr** Sec. : Renée EL MELHEM Bât. Blaise PASCAL, 3e étage **secretariat@edchimie-lyon.fr** INSA : R. GOURDON	M. Stéphane DANIELE Institut de recherches sur la catalyse et l'environnement de Lyon IRCELYON-UMR 5256 Équipe CDFA 2 Avenue Albert EINSTEIN 69 626 Villeurbanne CEDEX **directeur@edchimie-lyon.fr**
E.E.A.	**ÉLECTRONIQUE, ÉLECTROTECHNIQUE, AUTOMATIQUE** **http://edeea.ec-lyon.fr** Sec. : M.C. HAVGOUDOUKIAN **ecole-doctorale.eea@ec-lyon.fr**	M. Gérard SCORLETTI École Centrale de Lyon 36 Avenue Guy DE COLLONGUE 69 134 Écully Tél : 04.72.18.60.97 Fax 04.78.43.37.17 **gerard.scorletti@ec-lyon.fr**
E2M2	**ÉVOLUTION, ÉCOSYSTÈME, MICROBIOLOGIE, MODÉLISATION** **http://e2m2.universite-lyon.fr** Sec. : Sylvie ROBERJOT Bât. Atrium, UCB Lyon 1 Tél : 04.72.44.83.62 INSA : H. CHARLES **secretariat.e2m2@univ-lyon1.fr**	M. Philippe NORMAND UMR 5557 Lab. d'Ecologie Microbienne Université Claude Bernard Lyon 1 Bâtiment Mendel 43, boulevard du 11 Novembre 1918 69 622 Villeurbanne CEDEX **philippe.normand@univ-lyon1.fr**
EDISS	**INTERDISCIPLINAIRE SCIENCES-SANTÉ** **http://www.ediss-lyon.fr** Sec. : Sylvie ROBERJOT Bât. Atrium, UCB Lyon 1 Tél : 04.72.44.83.62 INSA : M. LAGARDE **secretariat.ediss@univ-lyon1.fr**	Mme Emmanuelle CANET-SOULAS INSERM U1060, CarMeN lab, Univ. Lyon 1 Bâtiment IMBL 11 Avenue Jean CAPELLE INSA de Lyon 69 621 Villeurbanne Tél : 04.72.68.49.09 Fax : 04.72.68.49.16 **emmanuelle.canet@univ-lyon1.fr**
INFOMATHS	**INFORMATIQUE ET MATHÉMATIQUES** **http://edinfomaths.universite-lyon.fr** Sec. : Renée EL MELHEM Bât. Blaise PASCAL, 3e étage Tél : 04.72.43.80.46 Fax : 04.72.43.16.87 **infomaths@univ-lyon1.fr**	M. Luca ZAMBONI Bât. Braconnier 43 Boulevard du 11 novembre 1918 69 622 Villeurbanne CEDEX Tél : 04.26.23.45.52 **zamboni@maths.univ-lyon1.fr**
Matériaux	**MATÉRIAUX DE LYON** **http://ed34.universite-lyon.fr** Sec. : Marion COMBE Tél : 04.72.43.71.70 Fax : 04.72.43.87.12 Bât. Direction **ed.materiaux@insa-lyon.fr**	M. Jean-Yves BUFFIÈRE INSA de Lyon MATEIS - Bât. Saint-Exupéry 7 Avenue Jean CAPELLE 69 621 Villeurbanne CEDEX Tél : 04.72.43.71.70 Fax : 04.72.43.85.28 **jean-yves.buffiere@insa-lyon.fr**
MEGA	**MÉCANIQUE, ÉNERGÉTIQUE, GÉNIE CIVIL, ACOUSTIQUE** **http://edmega.universite-lyon.fr** Sec. : Marion COMBE Tél : 04.72.43.71.70 Fax : 04.72.43.87.12 Bât. Direction **mega@insa-lyon.fr**	M. Jocelyn BONJOUR INSA de Lyon Laboratoire CETHIL Bâtiment Sadi-Carnot 9, rue de la Physique 69 621 Villeurbanne CEDEX **jocelyn.bonjour@insa-lyon.fr**
ScSo	**ScSo*** **http://ed483.univ-lyon2.fr** Sec. : Viviane POLSINELLI Brigitte DUBOIS INSA : J.Y. TOUSSAINT Tél : 04.78.69.72.76 **viviane.polsinelli@univ-lyon2.fr**	M. Christian MONTES Université Lyon 2 86 Rue Pasteur 69 365 Lyon CEDEX 07 **christian.montes@univ-lyon2.fr**

*ScSo : Histoire, Géographie, Aménagement, Urbanisme, Archéologie, Science politique, Sociologie, Anthropologie

Acknowledgement

These 40 months for the Ph. D thesis, are a significant stage for my whole life. This is the first time I stayed so far away from my hometown in a new country for further study. During this period, I learned to think more independently and objectively, to live alone, to get along with the people from different countries, to understand and respect the culture for each country, etc. It is said that studying for a Ph.D degree is more an experience than a result. From this point of view, I acquired too much in the process.

First, I would like to present my deep gratitude towards my director – Yuemin ZHU. He provides me a free research environment and encourages me to do what I believe. When I feel confused and disappointed, he will always try his best to help me find solutions. In addition, he offered me many opportunities to discuss with the researcher from all over the world, including international Summer School, international conference and international cooperation, which gave me the chance to learn the most advanced development of my field, to present my idea and discuss with the scientists. His serious attitudes to the research work, sense of responsibility, diligence and so many shining characteristics teaches me a lot, which will have a strong impact to the whole rest of my life. I would also like to thank Professor Lihui WANG in Guizhou University. During the four months international exchange in China, she helped me a lot not in both life and study. Her enthusiasm to the research, her direction and concern to the masters is an excellent example for me in the next years. What's more, I would like to express my thanks to the colleague Bingqing XIE, who is with the different but relative thesis with me. Without the discussion with him, I could not have the solutions and so many ideas.

Then, I would like acknowledge the support for my Ph. D thesis. The Chinese Scholarship Council, the finance support, makes me concentrate on my thesis. CREATIS, our Lab, provided an agreeable environment for the research. Thanks to Philippe DUVAUCHELLE and Valérie KAFTANDJIAN for providing the simulation software Virtual X-ray Imaging (VXI), and Philippe DOUEK for providing the real data collected from the Philips IQON spectral CT system. Thanks to the financial, lab and data support, I could finish my Ph.D thesis.

Meanwhile, thanks a lot to the friends in Lyon. Thanks for the share of happiness and sorrow with each other, the accompany in homesick, and the help in difficulties. Without these friends, the Ph. D period would not be as happy as it is. Although we have to go our separate ways, I will never forget this time.

Last but not the least, thanks to my parents for their continuous support and encouragement. Whatever decision I make, they will always be my side.

Contents

Abstract

Spectral photon-counting CT (sCT) appeared recently as a new imaging technique presenting fundamental advantages with respect to conventional CT and duel-energy CT. However, due to the reduced number of photons in each energy bin of sCT and various artifacts, image reconstruction becomes particularly difficult. This thesis focuses on the reconstruction of multi-energy images in sCT. First, we propose to consider the ability of sCT to achieve simultaneously both anatomical (aCT) and functional imaging (fCT) in one single acquisition through reconstruction and material decomposition. aCT function of sCT is studied under the same configuration as that of conventional CT, and fCT function of sCT is investigated by applying material decomposition algorithms to the same acquired multi-energy data. Then, since noise is a particularly acute problem due to the largely reduced number of photons in each energy bin of sCT, we introduce denoising mechanism in the image reconstruction to perform simultaneous reconstruction and denoising. Finally, to improve image reconstruction, we propose to reconstruct the image at a given energy bin by exploiting information in all other energy bins. The key strategy in such approach consists of grouping the similar pixels from the reconstruction of all the energy bins into the same class, fitting within each class, mapping the fitting results into each energy bin, and denoising with the mapped information. It is used both as a post-denoising operation to demonstrate its effectiveness and as a regularization term or a combined regularization term for simultaneous reconstruction and denoising. All the above methods are evaluated on both simulation and real data from a pre-clinical sCT system.

Keywords: X-ray computed tomography, Spectral photon-counting CT, anatomical CT, functional CT, reconstruction, denoising.

Résumé

Le scanner CT spectral à comptage de photons (sCT) est apparu récemment comme une nouvelle technique d'imagerie présentant des avantages fondamentaux par rapport au scanner CT classique et au scanner CT à double énergie. Cependant, en raison du nombre réduit de photons dans chaque bande d'énergie du scanner sCT et des artéfacts divers, la reconstruction des images devient particulièrement difficile. Cette thèse se concentre sur la reconstruction d'images multi-énergie en sCT. Tout d'abord, nous proposons d'étudier la capacité du scanner sCT à réaliser simultanément une imagerie anatomique (aCT) et fonctionnelle (fCT) en une seule acquisition par reconstruction et décomposition des matériaux. La fonction aCT du scanner sCT est étudiée dans la même configuration que celle du scanner CT classique, et la fonction fCT du scanner sCT est étudiée en appliquant des algorithmes de décomposition de matériaux aux mêmes données multi-énergie. Ensuite, comme le bruit est un problème particulièrement aigu en raison du nombre largement réduit de photons dans chaque bande d'énergie du scanner sCT, nous introduisons un mécanisme de débruitage dans la reconstruction de l'image pour effectuer simultanément un débruitage et une reconstruction. Enfin, pour améliorer la reconstruction de l'image, nous proposons de reconstruire l'image à une bande d'énergie donnée en exploitant les informations dans toutes les autres bandes d'énergie. La stratégie clé de cette approche consiste à regrouper les pixels similaires issus de la reconstruction de toutes les bandes d'énergie en une seule classe, à les ajuster dans la même classe, à projeter les résultats de l'ajustement dans chaque bande d'énergie, et à débruiter les informations projetées. Elle est utilisée à la fois comme une opération post-débruitage pour démontrer son efficacité et comme un terme de régularisation ou un terme de régularisations combinées pour la réalisation simultanée du débruitage et de la reconstruction. Toutes les méthodes ci-dessus sont évaluées sur des données de simulation et des données réelles provenant d'un scanner sCT préclinique.

Mots-clés : Le scanner CT aux rayons X, le scanner CT spectral à comptage de photons, CT anatomique, CT fonctionnel, reconstruction, débruitage

Synthèse en français de la thèse

Depuis son introduction par Cormack et Hounsfield dans les années 1970, le scanner CT aux rayons X est devenu une méthode d'imagerie indispensable dans la routine clinique. C'est la première méthode permettant d'examiner de manière non invasive la structure interne de l'objet sans opération physique, ce qui lui permet d'être largement appliquée dans divers domaines tels que la médecine et l'industrie.

Il est connu que le CT conventionnel, équpé d'un tube aux rayons X et des détecteurs d'intégration d'énergie (EID), mesure les photons totaux à travers un objet sur tout le spectre. Outre les informations anatamiques ou structurelles de l'objet, les scientifiques s'intéressent aussi aux matériaux de composition de l'objet, que l'on pourrait appeler les informations fonctionnelles. Motivé par cette curiosité, on a introduit le CT à double énergie (dual-energy CT—DECT), qui pourrait améliorer la qualité de la reconstruction et permet entre-outre d'examiner l'objet scanné grâce aux deux informations spectrales différentes. Cependant, comme le DECT ne peut obtenir que deux séries de données à la fois, il a une capacité limitée dans l'application d'imagerie par rayons X. Ces dernières années, avec le développement du matériel, des systèmes de CT aux rayons X montés avec des détecteurs à comptage de photons (PCD) sont apparus, qui a la capacité de distinguer des photons ayant des énergies différentes et de les mesurer séparément. Ce type de système de CT est appelé le scanner CT spectral à comptage de photons (sCT). Le sCT peut mesurer plus de deux ensembles d'informations pour l'objet scanné en une seule acquisition, qui pourraient être utilisées ultérieurement pour la reconstruction de l'image, l'amélioration de l'image et la décomposition de matériaux.

Dans la présente partie, tout d'abord, nous nous concentrons sur les applications possibles du sCT, notamment l'imagerie anatomique (aCT) qui décrit la structure de l'objet scanné, et l'imagerie fonctionnelle (fCT) qui donne la composition interne de l'objet scanné. Ensuite, nous proposons un opérateur de post-traitement utilisant les informations multi-énergie pour améliorer la qualité de la reconstruction, et nous évaluons les résultats par la qualité de l'aCT et du fCT aussi bien dans un système de CT numérique (virtuel) que dans un système de CT physique. Enfin, l'opérateur de post-traitement est appliqué comme un terme de régularisation à la fonction objective, qui permet de reconstruire et de débruiter simultanément les images sCT.

Cette thèse est organisée comme suit :

Chapitre 1 : Le scanner CT aux rayons X et le scanner spectral (sCT). Les principes des interactions des rayons X avec la matière sont présentés, notamment l'absorption photoélectrique, la diffusion de Compton et la production de paires. Le développement et les principes de la tomographie assistée par ordinateur aux rayons X sont décrits, notamment le CT conventionnel intégré en énergie, le DECT et le sCT.

Chapitre 2: Reconstruction des images sCT. Un examen des méthodes de reconstruction existantes pour le CT est présenté, y compris la méthode analytique, les méthodes itératives et les méthodes d'apprentissage. Pour chaque type de méthodes, une

ou plusieurs méthodes représentatives seront présentées en détail. Certaines de ces méthodes seront également utilisées dans les chapitres suivants.

Chapitre 3: Comparaison du CT conventionnel et du sCT. L'influence des paramètres du système de CT aux rayons X est comparée quantitativement entre le CT conventionnel et le sCT à partir des mesures par une série de simulations. De plus, le nombre de bandes d'énergie du sCT est discuté afin d'équilibrer la qualité de la reconstruction et la décomposition de matériaux.

Chapitre 4: Reconstruction d'images à l'aide d'informations multi-énergie dans le sCT. Une méthode de post-traitement qui exploite la relation entre les bandes d'énergie est présentée. La méthode est validée sur des données de simulation, de fantôme physique et de lapin pour démontrer sa performance.

Chapitre 5: Reconstruction et débruitage simultanés dans le sCT. Une méthode interactive intégrant le débruitage à la fois dans une bande d'énergie et parmi toutes les bandes d'énergie est présentée et validée sur des données simulées et sur des données réelles prevenant d’un sCT physique.

Chapitre 1: Le scanner CT aux rayons X et le scanner CT spectral (sCT).

Le scanner CT aux rayons X

Le scanner (CT) est devenu l'une des méthodes les plus populaires de diagnostic médical. Bien que rayons X ait déjà été appliquée à la radiographie, elle ne pouvait obtenir que l'image de la structure de superposition. Grâce aux travaux de Cormack et Hounsfield au siècle dernier, le scanner a pu recueillir les informations de l'objet scanné sous de multiples angles, ce qui en fait la première méthode permettant d'acquérir la structure interne du corps humain sans superposition de traumatisme physique explicite. Par conséquent, le scanner CT pourrait visualiser beaucoup plus de détails en avantage de la radiographie.

Depuis la première apparition du CT pour l'examen du cerveau en 1972, il a été appliqué à tout le corps, y compris la poitrine, l'abdomen, la colonne vertébrale et les membres. Au cours des dernières années, avec le développement de la technologie matérielle, l'instrument CT s'est développé à la fois dans la méthode de scanner et dans celle de détection. Les premiers équipements CT aux rayons X utilisaient la méthode de rotation/translation pour scanner l'objet et collectaient l'information avec seulement 1~2 détecteurs, qui ne pouvaient acquérir que des données limitées, nécessitaient un long temps de travail et obtenaient des images de mauvaise qualité. Plus tard, les progrès du matériel permettent d'utiliser plus de 1000 détecteurs et l'avancée de la méthode de scanner permet de terminer le scan dans le temps imparti par le mode rotatif/stationnaire, ce qui permet de reconstruire l'image de l'objet scanné avec une qualité et une résolution de haut niveau en peu de temps. En raison du développement rapide et de l'utilisation pratique du CT aux rayons X, il a maintenant été appliqué à de nombreux domaines tels que la médecin et l'industrie.

Le système de CT aux rayons X se compose principalement de trois parties: la source génère les photons de distribution spécifique selon les paramètres donnés; les détecteurs reçoivent les photons qui pénètrent dans l'objet, et le système de calcul pour le processus d'information, comme le montre la Figure 1.

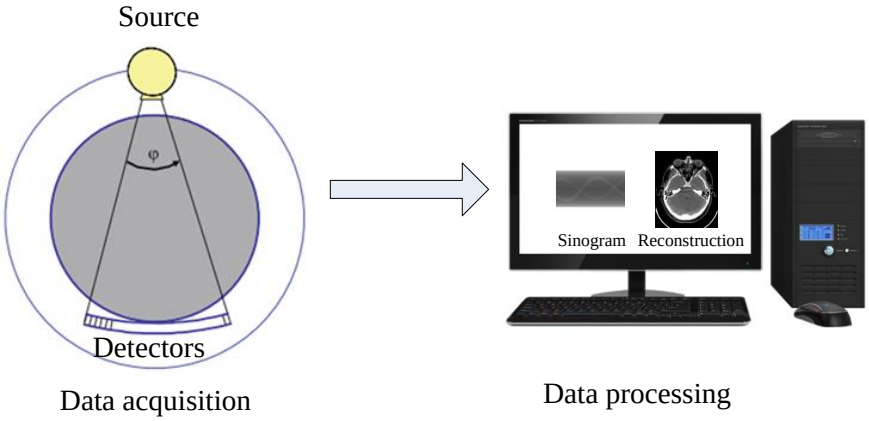

Figure 1 Système CT.

Le processus de travail du CT aux rayons X est le suivant: en fonction des différentes absorptions et transmissivités des tissus humains, les détecteurs de haute sensibilité sont appliqués pour mesurer le photon de chaque rayon X, et toutes les informations sont entrées dans l'ordinateur pour être traitées. Ensuite, l'image de la tranche ou du volume scanné peut être reconstruite pour découvrir des détials (e.g. lésion) du corps humain. Cependant, dans l'analyse médicale, en raison de la légère différence entre le tissu humain et les rayons X, il est souvent difficile de distinguer des détails minuscules. Par conséquent, la reconstruction d'une image CT de haute qualité

est une nécessité pour améliorer la précision du diagnostic.

Lorsque les rayons X pénètrent dans un objet, ils obéissent à la loi de Beer (M 2008), à savoir

$$I = I_0 e^{-\int_L \mu dl} \quad , \qquad (1)$$

où I_0 désigne le nombre de photons générés par la source, I le nombre de photons reçus par les détecteurs, et $\int_L \mu dl$ l'intégrale de la ligne de pénétration du coefficient d'atténuation des rayons X de la source au détecteur. Dans le CT des rayons X, I_0 et I sont les mesures.

La loi de Beer indique la réduction du nombre de photons des rayons X lorsqu'ils pénètrent dans l'objet. La réduction exponentielle du nombre de photons est le résultat de l'interaction des photons et de l'objet, dont les fonctions les plus importantes sont la diffusion de Compton, l'absorption photoélectrique et la production de paires.

Le CT spectral (sCT)

Au cours des dernières années, le système CT s'est développé du CT conventionnel au DECT puis au sCT, ce qui est principalement dû aux progrès de la technologie de scannage et de détection. Le sCT a remplacé les EID dans le CT conventionnel et le DECT par des PCD, ce qui lui permet d'obtenir plus de deux séries de mesures en une seule acquisition.

Dans l'EID, les rayons X incidents frappent le scintillateur supérieur et sont convertis en lumière visible. Ensuite, la lumière visible générée est absorbée par une photodiode fabriquée dans un matériau à semi-conducteur, qui peut mesurer la quantité de lumière incidente et créer un signal électrique proportionnel à l'énergie totale. Contrairement à l'EID, le PCD ne contient pas de scintillante mais est constitué d'un diode semi-conducteur sur lequel est appliquée une forte tension. Lorsque le rayon X incident atteint le semi-conducteur, il génère un nuage de charges positives et négatives. Ces charges sont rapidement arrachées sous la force de la tension et génèrent une impulsion électrique, qui est lue par un circuit électronique. Les photons qui frappent le détecteur génèrent des impulsions électriques, dont la hauteur est proportionnelle à l'énergie du photon.

Le nombre de ces impulsions est compté par le système électronique à l'aide de seuils prédéfinis, dont la portée est fixée entre l'électronique et la hauteur des impulsions. Par conséquent, dans les PCD, les photons sont classés en différentes

classes (à savoir le bande d'énergie) en fonction de leur énergie, en comparant l'impulsion électronique générée avec les seuils. Entre-temps, dans ce mécanisme, le bruit électronique présent est supprimé de l'impulsion de photon en raison du seuil plus haut. Dans les EID, l'information totale sous la courbe du signal est comptée pendant l'intervalle de mesure, ce qui fait qu'elle n'a pas la capacité de distinguer l'énergie et qu'elle contient le bruit électronique.

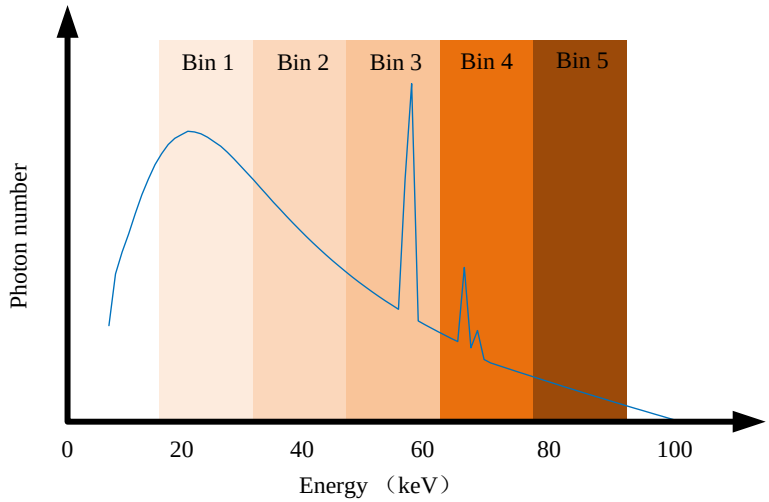

Figure 2 PCDs. Les photons ayant des énergies différentes sont classés dans plusieurs bandes d'énergie.

En raison de la capacité de distinction des PCD, le sCT offre un fort potential pour la reconstruction d'images, la décomposition de matériaux et l'amélioration d'images..

Chapitre 2: Reconstruction d'images sCT

De nombreuses recherches ont été effectuées sur la reconstruction depuis l'introduction de CT. En tant que système CT, une image sCT pourrait également être reconstruite en utilisant les méthodes de reconstruction conventionnelles. En même temps, en raison des caractéristiques de sCT, de nombreuses méthodes spécifiques ont été développées pour la reconstruction des images sCT. Au cours des dernières années, la reconstruction de CT est passée de la méthode analytique traditionnelle à des méthodes itératives et aujourd'hui à des méthodes d'apprentissage. La première est la méthode analytique, qui reconstruit l'image à partir de la formulation de la projection par transformation inverse. La seconde est la méthode itérative, qui reconstruit l'image en créant un modèle combinant les erreurs de reconstruction et les connaissances a priori. En raison de leur capacité de modélisation non linéaire, les méthodes d'apprentissage ont été appliquée à la reconstruction des images sCT sur la base d'une grande quantité de données.

La méthode représentative de la méthode analytique est la rétropropagation filtrée (FBP-Filtered back projection), qui est basée sur le théorème de Fourier–tranche et qui dit que la transformée de Fourier 1D de l'intégration de la ligne mesurée est égale à la transformée de Fourier 2D de l'image à l'angle de balayage. Ainsi, l'image originale pourrait être reconstruite par la transformée de Fourier et la transformée de Fourier inverse. FBP reconstruit l'image à partir du principe de la projection, qui est l'algorithme le plus stable et le plus rapide de la reconstruction. Par conséquent, il s'agit de la méthode la plus utilisée dans l'industrie.

Depuis l'invention du CT aux rayons X, les premières reconstructions ont été réalisées par l'ART. Bien que la FBP soit l'algorithme le plus largement appliqué, l'ART a toujours une influence significative car elle considère le problème de reconstruction comme un système linéaire d'équations, à savoir le problème inverse. En discrétisant l'intégration linéaire des rayons X, le problème peut être exprimé comme un problème inverse, à savoir

$$Y = AU\,, \qquad (2)$$

où A est également appelée la matrice du système, qui est déterminée par la géométrie du système et la façon dont il est scanné, est Y la mesure pour chaque bande d'énergie, et U pour la reconstruction pour chaque bande d'énergie.

En pratique, la solution des équations ne peut pas être obtenue facilement car le problème est mal conditionné. De très petites valeurs singulières peuvent se produire et de très petites erreurs de mesure entraîneront de grandes fluctuations dans les images reconstruites. Ainsi, dans la méthode ART, ce problème inverse est résolu par un algorithme itératif, qui commence par une hypothèse d'image initiale, et compare les valeurs calculées dans le processus jusqu'à atteindre les conditions de convergence (le nombre d'itérations maximum ou le seuil des erreurs).

L'ART tire parti de la méthode FBP pour réduire le bruit, en particulier dans le cas de données rares et incomplètes. L'essence de l'algorithme ART est de construire la

reconstruction comme un système d'équations et d'explorer la méthode itérative pour résoudre ce modèle. Inspirées par cette idée, de nombreuses méthodes ont été développées, qui incorporent les informations préalables pour améliorer les performances.

Le modèle amélioré se compose généralement de deux parties : le terme de fidélité des données pour mesurer les erreurs de reconstruction et le terme de régularisation pour indiquer les connaissances préalables. L'objectif de la méthode est de minimiser la somme du terme de fidélité des données et du terme de régularisation, à savoir la fonction objective, qui peut être représentée comme

$$U^* = \arg\min_U \left\{ \mathcal{F}(U) + \lambda \mathcal{R}(U) \right\}, \quad (3)$$

où $\mathcal{F}: \mathbb{R}^N \to \mathbb{R}^M$ est le terme de fidélité des données, qui est généralement défini comme

$$\mathcal{F}(U) = \frac{1}{2} \| Y - AU \|_2^2, \quad (4)$$

et $\mathcal{R}: \mathbb{R}^N \to \mathbb{R}^M$ définit la pénalité de régularisation comme $\lambda > 0$ étant le paramètre de régularisation qui équilibre le compromis entre les deux termes. Le terme de régularisation ne se limite pas nécessairement à une seule partie, ce qui signifie qu'il peut inclure toutes les informations préalables en plusieurs parties. Beaucoup de recherches ont été faites sur le terme de régularisation et montrent de meilleures performances, y compris la variation totale (TV-Total variation), la variation nucléaire totale (TNV-Total nuclear variation) et un modèle antérieur de rang, d'intensité et de rareté (PRISM- A prior rank, intensity and sparsity model) .

Les méthodes d'apprentissage approfondi ont attiré beaucoup d'attention ces dernières années en raison de leur efficacité, y compris pour l'imagerie médicale"; Il est certain que le grand nombre de données surtout sur fantômes pourrait être disponibles Cependant, les bonnes performances sont basées sur le grand nombre de données, ce qui en fait une application limitée à la reconstruction de sCT.

Chapitre 3: Imagerie multimodèle de sCT

En raison de sa résolution en énergie plus haute, le sCT peut être utilisé non seulement pour obtenir des images des caractéristiques anatomiques (ou structurelles) d'un objet, mais aussi pour obtenir la composition quantitative de matériaux qui constituent l'objet. En ce sens, le sCT offre la possibilité de réaliser simultanément un CT anatomique (aCT) et un CT fonctionnel (fCT), ce qui est très intéressant pour de nombreuses applications.

Dans ce chapitre, nous étudions les possibilités de sCT pour réaliser simultanément une imagerie multimodale. L'idée consiste à utiliser le sCT pour réaliser à la fois l'imagerie anatomique conventionnelle (aCT) et la nouvelle imagerie fonctionnelle (fCT). À cette fin, un système virtuel de sCT et un fantôme contenant différents matériaux de densités diverses ont été conçus. Ensuite, des données multi-énergie à différents bandes d'énergie du fantôme ont été acquises à l'aide du système sCT virtuel. Enfin, la fonction aCT du sCT a été étudiée en utilisant la même configuration que celle du CT classiquele, et, en même temps, la fonction fCT du sCT a été étudiée en appliquant des algorithmes de décomposition de matériau aux mêmes données multi-énergie acquises.

Méthodes

Pour étudier l'imagerie multimodale de sCT, nous avons conçu le fantôme illustré à la Figure 3, qui est un cylindre en PMMA d'un diamètre de 80 mm et d'une épaisseur de 0.1 mm, afin de pouvoir le reconstruire en une seule tranche. Il contient 31 trous de 6 mm de diamètre, qui sont remplis d'eau et de différents matériaux de concentrations différentes. Les trous le long de chaque rangée horizontale contiennent le même matériau mais ont des concentrations différentes. Trois agents de contraste communs ont été pris en compte : Gd, I et le fer (Fe). Les concentrations de Gd et de I ont été fixées à 5, 15, 25, 35, 45, 55 mg/cc, et celles de Fe à 30, 50, 100, 150, 200 mg/cc. Les mélanges sont remplis d'eau et des trois agents de contraste de même concentration dans la même colonne. Par exemple, le mélange $1^{\#}$ est composé d'eau, Gd de 5 mg/cc, I de 5 mg/cc et Fe de 15 mg/cc ; le mélange $6^{\#}$ contient de l'eau, Gd de 55 mg/cc, I de 55 mg/cc et Fe de 200 mg/cc.

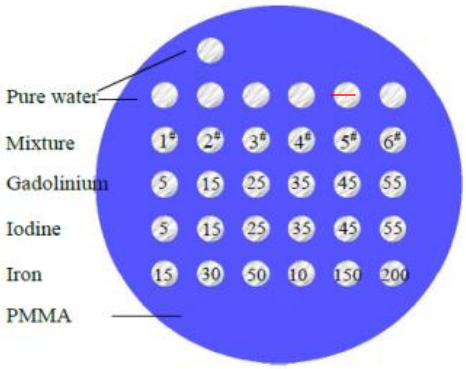

Figure 3 Le fantôme contenant différents matériaux de concentrations différentes.

Ce fantôme a été utilisé pour démontrer les capacités de l'aCT et de la fCT du sCT. L'imagerie aCT comprenait deux parties : la comparaison des images aCT avec les images CT conventionnelles, qui a été faite sous les mêmes paramètres que dans la simulation ; l'amélioration dans aCT, qui a utilisé les informations multi-énergie pour obtenir des images avec un rapport signal/bruit (SNR) et un rapport contraste/bruit (CNR) élevés dans la simulation et le CT physique. Les images fCT ont été analysées avec divers matériaux et leurs concentrations correspondantes. Toutes les images aCT ont été reconstruites par l'algorithme FBP le plus largement utilisé, et les images fCT ont été obtenues en utilisant la méthode de décomposition des matériaux de la norme L1. Enfin, le paramétrage du sCT est également abordé.

Résultats

Tout d'abord, nous voulons montrer ce que le sCT peut produire comme images anatomiques (aCT) et comparer les images sCT avec les images CT conventionnelles pour différentes configurations d'angle de projection (y compris 50, 100, 300, 600 et 1200), de courant (y compris 0.1 mA, 1 mA, 10 mA et 100 mA) et de tension (y compris 80 keV, 100 keV, 120 keV et 140 keV). La simulation est réalisée à l'aide du logiciel Virtual X-ray Imaging (VXI) de l'INSA Lyon. Un système sCT est constitué d'un PCD de 700 pixels disposés en ligne. Le spectre a été simulé sur la base du modèle de Birch & Marshall pour un matériau cible en tungstène sans filtration. Le détecteur a une capacité de résolution en énergie de 5 bandes d'énergie. Les bandes d'énergie sont 30-39, 40-49, 50-59, 60-69 et 70-79 keV.

La Figure 4 montre les résultats de la reconstruction à partir de 300 projections, avec la tension de la source fixée à 100 keV, et le courant à 0.1 mA. Le CNR a également été calculée dans les ROIs (31 trous dans le fantôme) pour le CT classique et l'aCT (Figure 4 (c)). Dans les ROIs qui consistent en eau, mélange, Gd, I, ou Fe, les ROI reconstruits à partir d'aCT ont des CNR plus élevés que ceux du CT classique, ce qui est également cohérent avec ce qui est observé visuellement. Les CNRs d'aCT sont toujours plus élevés que ceux des CT conventionnels.

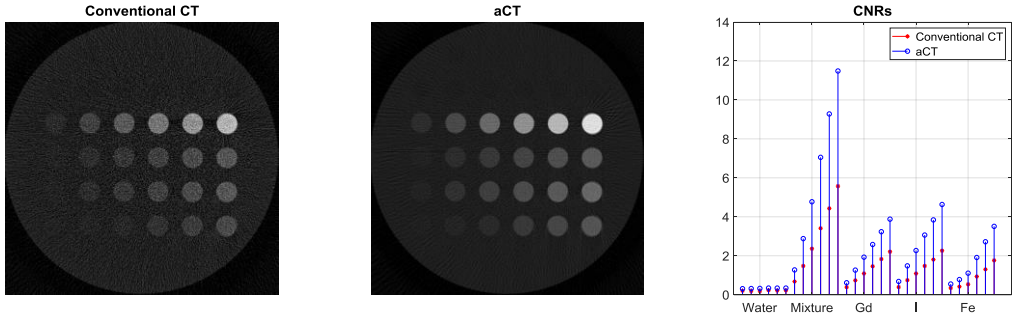

(a) (b)

Figure 4 Images reconstituées à partir : (a) du CT classique ; (b) de l'aCT, et (c) CNRs des ROIs, avec 300 projections, un courant de source de 0.1 mA et 100 kVp.

La Figure 5 compare les CNRs du CT classique et de la aCT pour différents angles de projection, différents courants de source et différentes tensions de source. Comme le montre Figure 5(a), avec l'augmentation du nombre de projections, les CNRs de l'aCT et du CT classique augmentent, mais les CNRs de l'aCT sont toujours plus élevés que ceux du CT classique, surtout dans le cas de projections moins nombreuses. La Figure 5(b) illustre les CNRs pour différents courants de source. Les CNRs de l'aCT sont toujours plus élevés que ceux du CT classique, en particulier pour les courants faibles, à savoir les faibles doses. Avec l'augmentation du courant, les CNRs de l'aCT et du CT classique augmentent, mais l'augmentation est moins importante dans le cas de projections de plus en plus nombreuses. La Figure 5(c) donne les CNRs pour différentes tensions. Les CNRs du sCT sont toujours plus élevés que ceux du CT classique. Avec l'augmentation de la tension de la source, les CNRs du sCT et du CT conventionnel augmentent.

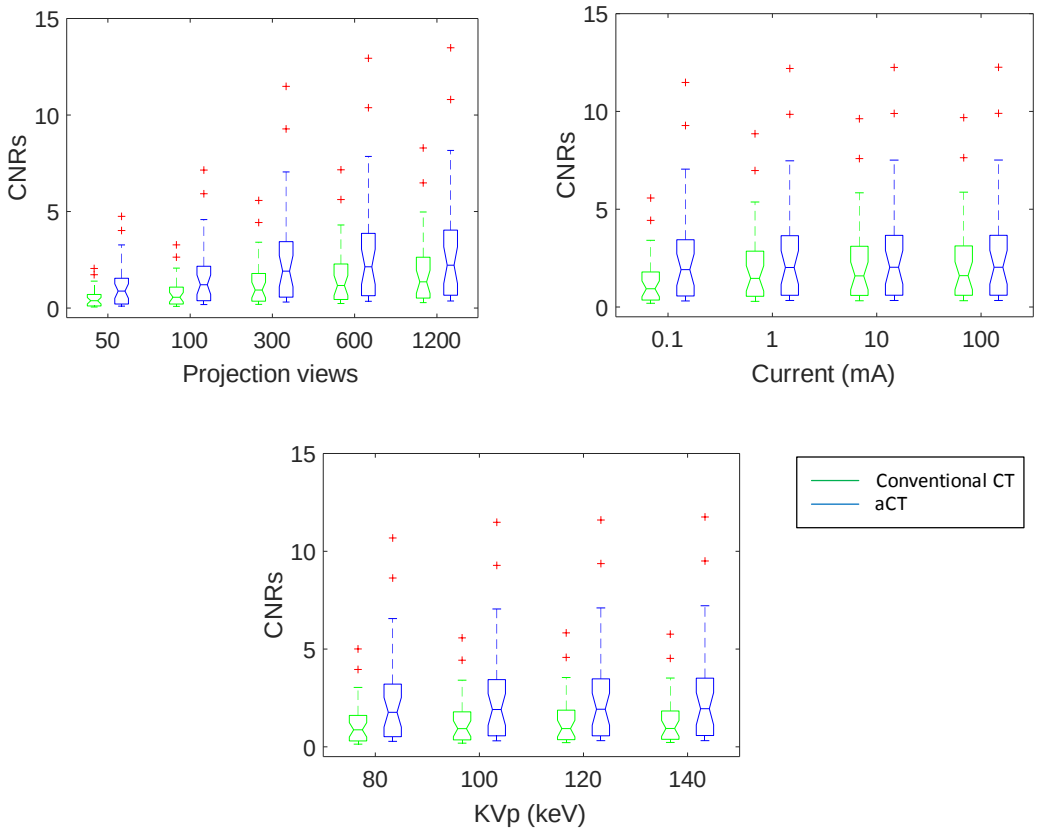

Figure 5 Comparaison entre le CT classique (la ligne verte) et l'aCT (la ligne bleue) en termes de CNRs pour: (a) différents angles de projection; (b) différents courants de source; (c) différentes tensions de source.

Pour étudier les images aCT améliorées, les bandes d'énergie ont été fixées respectivement à 30-39, 40-49, 50-59, 60-69 et 70-79 keV. L'énergie du bord K est située dans le bande d'énergie de 50-59 keV pour le matériau Gd, et de 30-39 keV pour le matériau I. Ainsi, pour Gd, l'atténuation effective dans le bande d'énergie 50-59 keV est la plus élevée parmi les cinq bandes, et pour I dans 30-39 keV. Nous nous sommes

donc concentrés sur ces deux bandes d'énergie pour étudier la visibilité de Gd et I (avec un courant de source fixe de 0.1 mA et des angles de projection de 300).

Pour améliorer le CNR de Gd et I, nous avons utilisé l'image de 70-79 keV en raison de son SNR le plus élevé parmi les cinq bandes. La figure 3.7 montre, pour l'étude de Gd, la comparaison entre l'image originale au niveau de la bande d'énergie 50-59 keV et sa version améliorée en ajoutant l'image de la bande d'énergie 70-79 keV. De même, pour l'étude de I, la Figure 6 montre la comparaison entre l'image originale à la source d'énergie 30-39 keV et sa version améliorée en ajoutant l'image de la source d'énergie 70-79 keV. Comme on l'a observé, en ajoutant les données d'une autre bande d'énergie ayant le SNR le plus élevé à l'image actuelle d'intérêt (avec le SNR le plus élevé), nous avons réussi à obtenir une image améliorée présentant à la fois un CNR et un SNR plus élevés par rapport à l'image originale. En fait, l'ajout de deux images provenant de deux bandes d'énerggie différents améliore le CNR et le SNR. Si l'on considère un plus grand nombre de cas, l'amélioration du SNR sera plus évidente, mais le CNR pourrait ne pas être amélioré de manière significative en raison d'un CNR plus faible dans d'autres bandes d'énergie. Pour les matériaux avec un bord K, l'amélioration est particulièrement visible. En prenant un autre exemple sur le matériau Fe qui n'a pas de bord K dans la bande d'énergie indiquée ci-dessus, nous montrons sur la Figure 6 l'image originale à la bande d'énergie 30-39 keV et sa version améliorée en ajoutant l'image du même bande d'énergie 70-79 keV. Nous pouvons observer des résultats similaires.

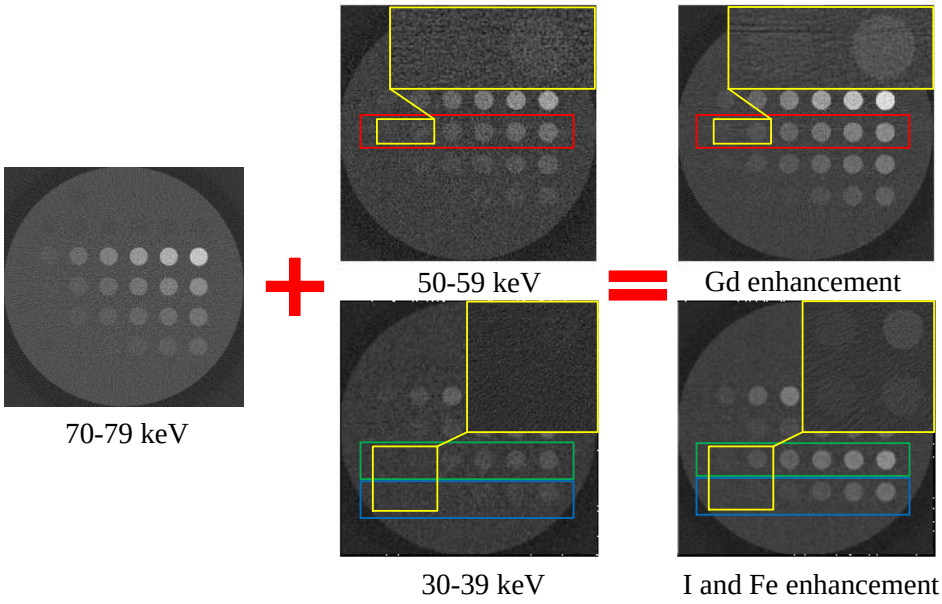

Figure 6 Comparaison des CNRs et des SNRs des images originales (colonne du milieu) aux bandes d'énergie 30-39 keV et 50-59 keV et de leur version améliorée (colonne de droite) en faisant la moyenne avec l'image de la bande d'énergie 70-79 keV (colonne de gauche). La visibilité de Gd (région de la boîte rouge), I (région de la boîte verte) et Fe (région de la boîte bleue) est nettement améliorée, et la région contenant des matériaux à faible concentration (région de la boîte jaune) est agrandie (coin supérieur droit). Toutes les images sont affichées sous une forme normalisée.

Afin d'évaluer la capacité du sCT à améliorer les images aCT, nous avons également réalisé la même expérience sur des données réelles acquises à l'aide d'un système de sCT physique. Le fantôme physique utilisé contient du Gd, du I, de l'eau et du PMMA à différentes concentrations Figure 7, colonne de gauche). Il a été scanné par une tension de 150 keV divisée en 5 bandes : 27-47 keV, 48-58 keV, 59-68 keV, 69-79 keV, et 80-150 keV. Les images multi-énergie originales et les images améliorées sont présentées dans la Figure 8. Le contraste de matériaux Gd et I est clairement amélioré après avoir combiné deux images multi-énergie correspondant à deux bandes d'énergie. De plus, le SNR (calculé sur les ROI) des images améliorées est également nettement amélioré (Figure 9).

Les images fCT du sCT sont des images spatiales de matériaux illustrées dans la Figure 10 pour différents courants de source. La vérité-terrain fCT contient de la PMMA, de l'eau et du Gd de 55 mg/cc, de l'I de 55 mg/cc et du Fe de 200 mg/cc. Les images fCT correspondent aux différents courants de respectivement 0.1 mA, 1 mA, 10 mA et 100 mA avec le tube source fixé à 100 keV et le nombre en projections à 300. Visuellement, l'augmentation du courant réduit le bruit et les images fCT sont plus proches de la vérité-terrein pour tous les matériaux en question.

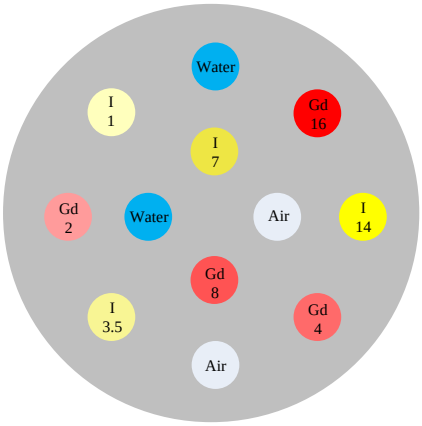

Figure 7 Illustration du fantôme pour le CT physique.

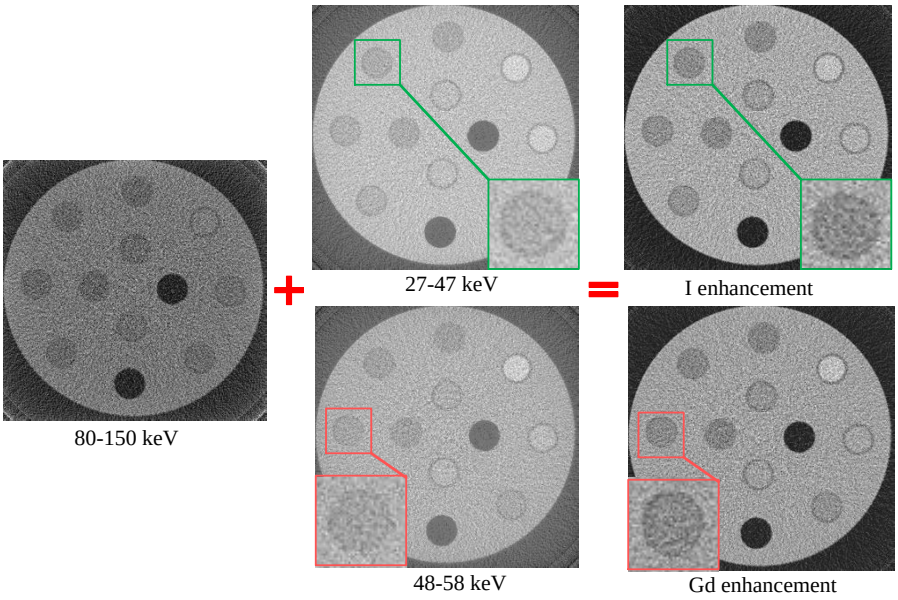

Figure 8 Amélioration de l'aCT sur des données réelles acquises à l'aide du sCT physique.

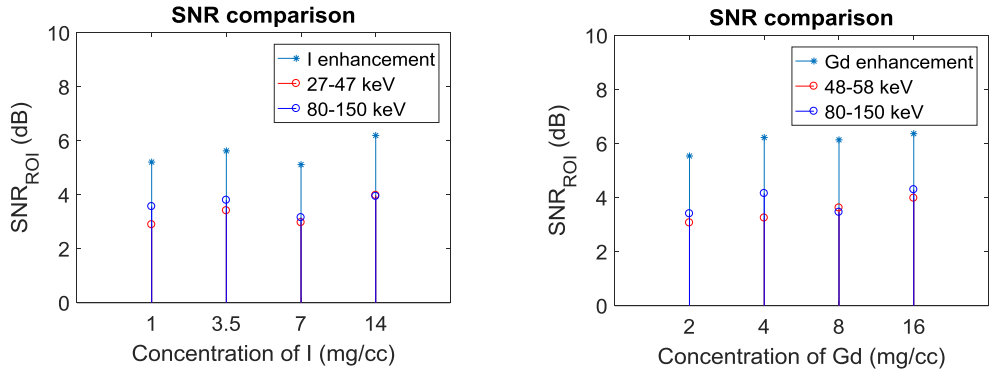

Figure 9 Comparaison du SNR pour les images originales et les images améliorées.

En même temps, la fCT issue du sCT a également été validée sur le fantôme physique présenté dans la Figure 7. Les résultats sont présentés dans la Figure 11. Le fond en plastique sans effet de bord K étant similaire à l'eau, il a été, comme prévu, décomposé en eau (ou plus exactement en un matériau similaire à l'eau mais de concentration plus élevée que l'eau). Les Gd et I de fortes concentrations (trous jaunes) sont clairement mis en évidence ; les Gd (ou I) de faibles concentrations inférieures ou égales à 4 mg/cc (ou inférieures ou égales à 3,5 mg/cc) sont beaucoup plus difficiles à distinguer. Bien qu'elles ne soient pas parfaites en raison de la présence de bruit et d'artéfacts, les images décomposées montrent clairement la distribution spatiale des matériaux dans le fantôme.

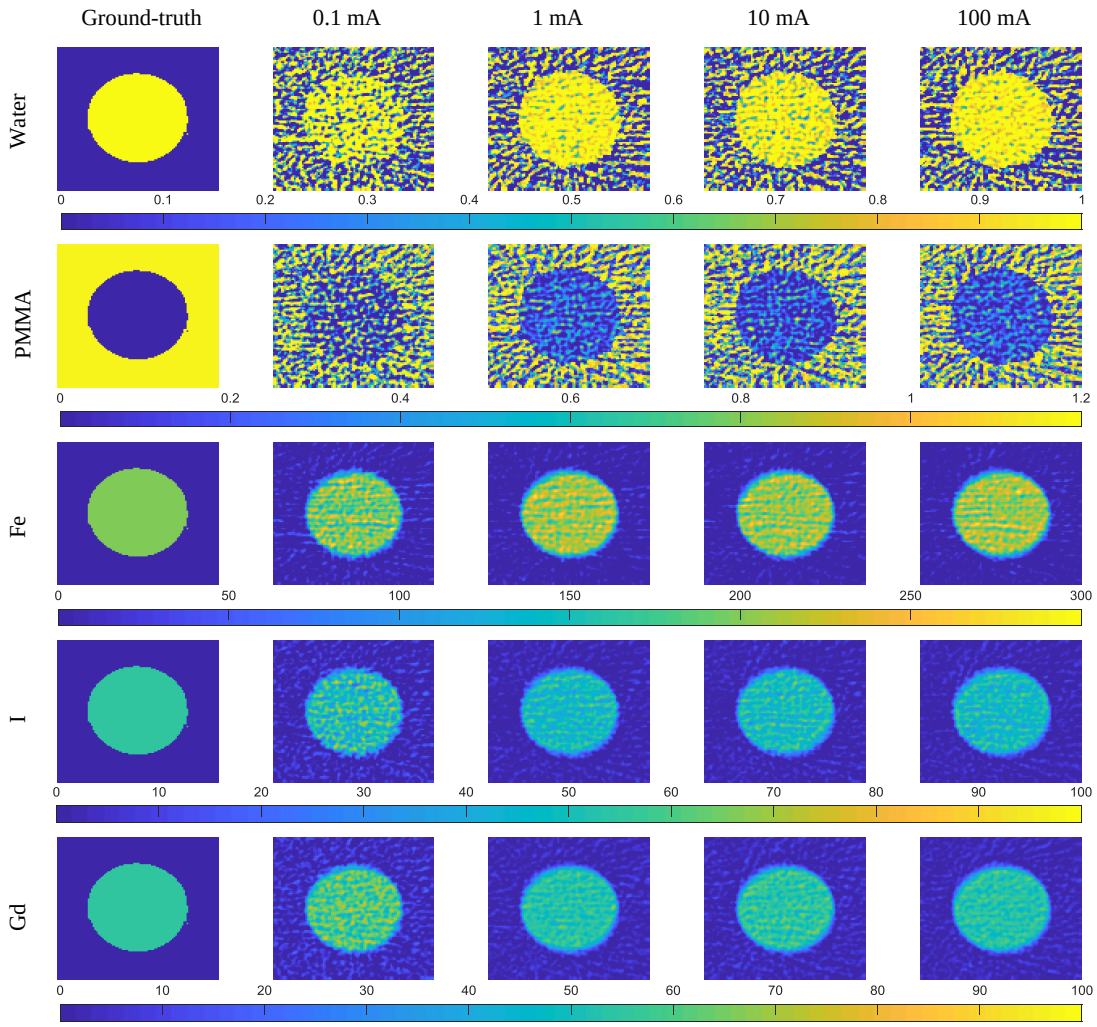

Figure 10 Décomposition de matériaux du mélange 6# (PMMA, eau, Gd de 55 mg/cc, I de 55 mg/cc et Fe de 200 mg/cc) dans la Figure 3 sous quatre courants de source différents dans le sCT. La première colonne est le fond de vérité des matériaux. La tension de la source a été fixée à 100 keV et la projection à 300.

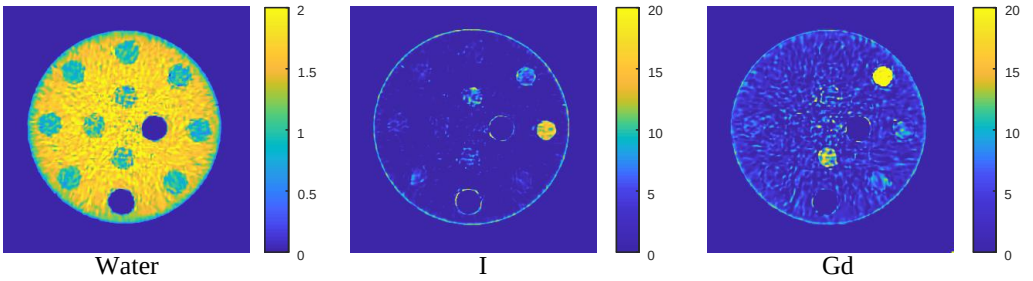

Figure 11 La fCT du sCT du fantôme physique. La valeur des pixels représente la concentration du matériau en mg/cc.

Comme on l'a observé, lorsqu'elle est utilisée comme aCT, le sCT obtient, avec les mêmes paramètres d'imagerie, de meilleures performances que le CT classique. La

question est alors de savoir quel courant de source peut être adopté dans le CT conventionnel pour obtenir la même qualité d'image que dans l'aCT. Il s'agit d'une question cruciale dans les applications cliniques puisque le courant de source est directement lié à la dose des rayons X.

Pour répondre à cette question, nous avons conçu un fantôme illustré à la Figure 12, qui présente 9 ROIs (5 trous et 4 anneaux) remplis de matériau Gd (parties vertes) de densité 5 mg/cc et I (disques jaunes) de densité 5 mg/cc sur le cylindre en PMMA. De plus, 5 ROIs sont étiquetés dans le fantôme, dont 4 trous de I avec un rayon de 30 mm (numéro 1), 15 mm (numéro 2), 7,5 mm (numéro 3) et 3 mm (numéro 4), et 1 trou de Gd (numéro 5) avec un rayon de 60 mm. Le rayon du PMMA est de 300 mm, et la taille de la reconstruction est de 800×800. Le nombre de projections et la tension de la source ont été fixés à 300 et 100 kVp, respectivement. Pour un même courant de source de 0.1 mA, le ROI 4 (rayon de 3 mm) est détecté dans l'aCT mais n'est pas distingué dans le CT classique (version zoomée dans le coin supérieur droit de la Figure 12). De même, pour le ROI 3 (rayon de 7,5 mm), il est clairement visible dans l'aCT mais ne l'est pas dans le CT classique. Lorsque le courant de source du CT classique est multiplié par 10 par rapport à l'aCT, de 0.1 mA à 1 mA, les reconstructions du CT classique et de l'aCT présentent une qualité visuellement similaire, et les images reconstituées ont également le même ordre de grandeur.

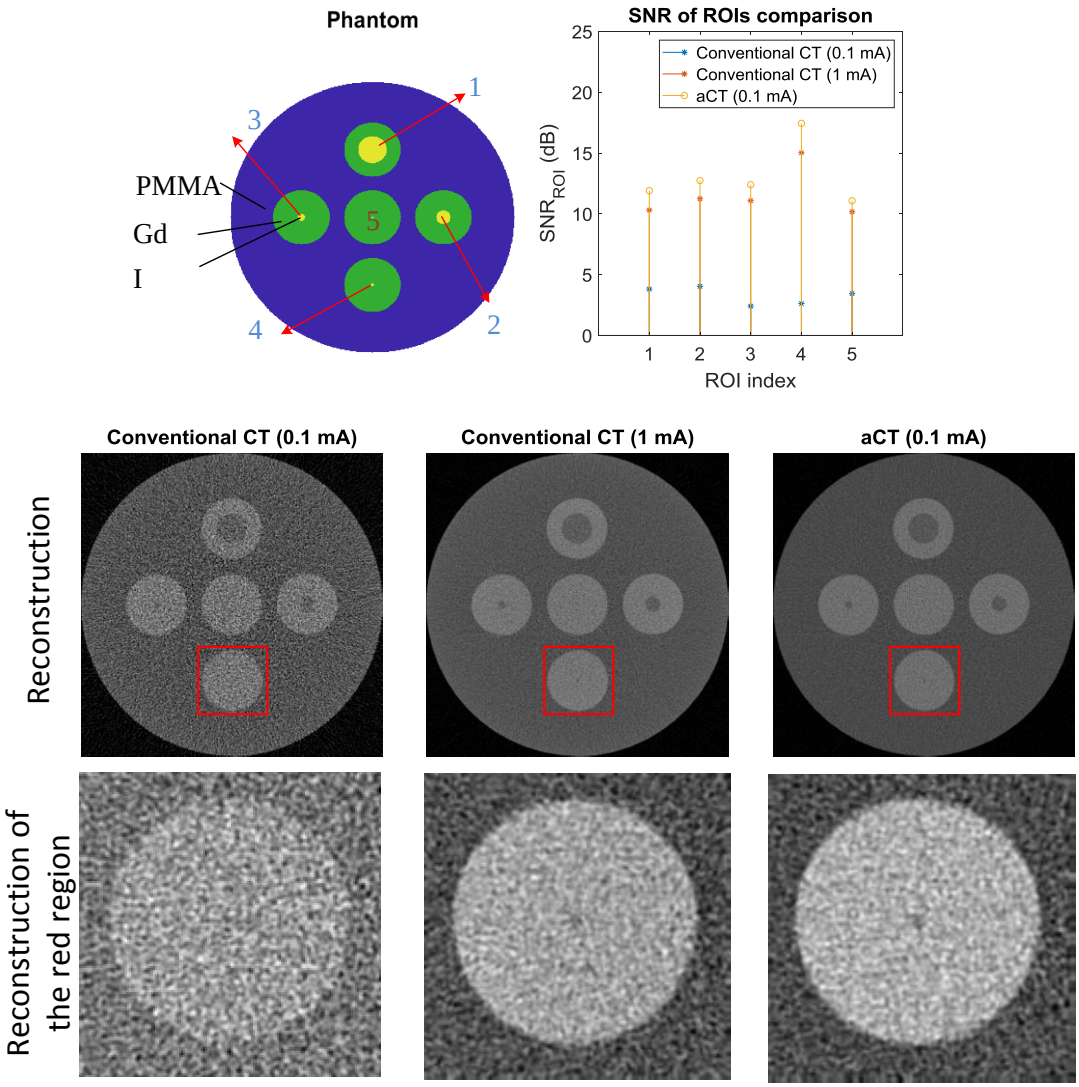

Figure 12 Comparaison entre l'image aCT du sCT et l'image CT classique. La région zoomée contient le petit trou de 3 mm de rayon (au centre de la région rempli d'iode de densité 5 mg/cc).

Conclusion

Nous avons étudié les potentialités du sCT par rapport au CT conventionnel par le biais de simulations et de validations physiques. Nous avons démontré, tant qualitativement que quantitativement, qu'en raison de ses caractéristiques de données multi-énergie, le sCT peut être utilisé pour réaliser simultanément l'imagerie anatomique et fonctionnelle avec une seule acquisition. Lorsqu'elle est utilisée en tant qu'aCT, le sCT permet d'obtenir des images anatomiques équivalentes à celles générées par le CT conventionnel, mais avec une qualité d'image bien meilleure. Cela est vrai pour différentes configurations de paramètres d'imagerie tels que le nombre de projections, le courant et la tension. Un autre avantage du sCT, et non des moindres, est sa qualité supérieure à celle du CT conventionnel à dose égale. En outre, le sCT offre la

possibilité d'améliorer intrinsèquement les images anatomiques dans l'aCT en utilisant différentes images correspondant à différentes bandes d'énergie. Les images obtenues présentent un SNR et un CNR sensiblement améliorés. Parallèlement, lorsqu'elle est utilisée comme fCT, le sCT nous permet d'obtenir des informations sur la composition quantitative de matériaux dans un pixel au moyen d'algorithmes appropriés de décomposition de matériaux. Cette capacité d'imagerie multimodalité simultanée du sCT avec une seule acquisition pourrait changer la façon d'utiliser le CT conventionnel et ouvrir de nombreuses nouvelles applications.

Chapitre 4: Reconstruction d'images à l'aide d'informations multi-énergie en sCT

En tant que nouveau type de CT, le sCT pourrait obtenir plus de deux ensembles de données en un seul balayage grâce aux PCD, qui ont la capacité de compter séparément le nombre de photons ayant des énergies différentes. Cependant, plus de bandes d'énergie signifient également moins de photons dans une bande, ce qui diminuera évidemment la qualité de reconstruction de l'image. Bien que les valeurs de l'image reconstruite (à savoir le coefficient d'atténuation) soient différentes pour chaque bande d'énergie, il existe toujours une relation intrinsèque entre les valeurs (à la même position) correspondant aux différentes bandes en raison de la cause de l'atténuation des rayons X. Dans ce chapitre, nous avons pour objectif de développer une méthode de reconstruction d'images qui explore l'intercorrélation entre différentes bandes d'énergie et qui, en même temps, utilise la similarité au sein de chaque bande d'énergie pour améliorer la qualité de reconstruction. Ainsi, pour ce faire, nous commençons par regrouper les pixels similaires issus de la reconstruction primaire (généralement avec des artéfacts et non parfaits) de toutes les bandes d'énergie, puis nous effectuons un ajustement linéaire pour chaque paire de bandes d'énergie sur les résultats du regroupement. Les résultats de l'ajustement sont utilisés pour améliorer les reconstructions finales.

Méthodes

Pour une même position dans les images reconstruites de chaque bande, la relation des coefficients d'atténuation dépend de la courbe d'atténuation du matériau de cette position. Par conséquent, l'information entre les bandes d'énergie pourrait également être utilisée pour améliorer la qualité de l'image de reconstruction. Zhang et al. ont trouvé la relation de cartographie des coefficients d'atténuation parmi les bandes d'énergie et ont introduit une méthode d'ajustement par morceaux au terme de régularisation de la méthode de reconstruction itérative. Cette méthode d'ajustement combine l'information parmi toutes les autres bandes pour débruiter et améliorer la qualité de l'image reconstruite. Cependant, cette méthode ne prend que l'eau comme seuil et utilise deux ajustements linéaires pour représenter la relation entre les bandes. En fait, pour différentes compositions de matériaux, les coefficients d'atténuation entre chacun des deux paires de bandes obéissent à une relation d'ajustement spécifique. De cette façon, les données pour la même position des autres bandes pourraient être utilisées pour améliorer la qualité de la reconstruction. Par conséquent, dans cette étude, l'ajustement inter-spectral dépendant du matériau est proposé comme post-traitement pour améliorer la qualité des images reconstruites.

Le cadre de notre méthode est présenté dans la Figure 13. Tout d'abord, la reconstruction primaire de chaque bande d'énergie est acquise par la méthode de base (FBP pour la simulation et SART pour le CT physique). Comme la relation linéaire existe sur la composition similaire des matériaux, l'étape suivante consistera à trouver

les positions avec la composition similaire de matériaux. Dans notre algorithme, l'algorithme le plus courant, k-means, est adapté pour regrouper la composition de matériaux similaires. Ensuite, l'ajustement linéaire est fait pour tous les points de chaque classe séparément. En utilisant les coefficients d'ajustement, pour le sCT avec cinq bandes d'énergie, chaque position dans une bande d'énergie est projetée dans les quatre autres bandes d'énergie. C'est-à-dire que maintenant les coefficients d'atténuation auront cinq valeurs différentes pour chaque bande d'énergie : la reconstruction originale et les projections des quatre autres bandes. Par conséquent, un filtre est appliqué sur les cinq valeurs pour réduire le bruit. De cette façon, l'information des autres bandes d'énergie est utilisée pour améliorer la qualité des images de reconstruction.

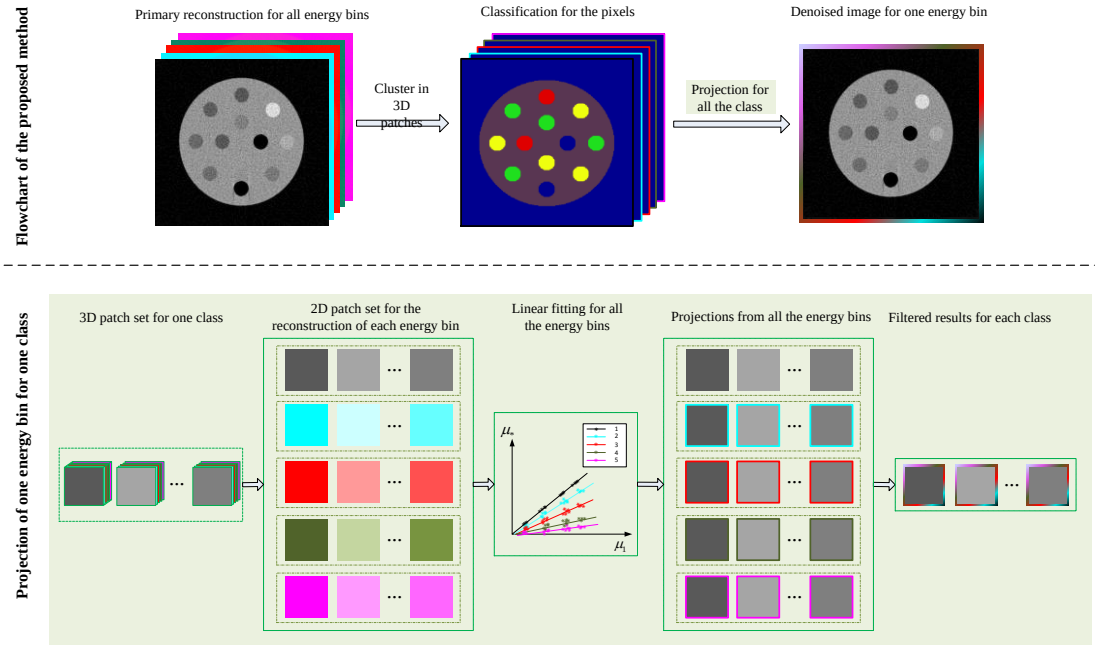

Figure 13 Cadre de la méthode proposée: débruitage de reconstruction pour une bande d'énergie.

Résultats

La simulation est réalisée à l'aide du logiciel Virtual X-ray Imaging (VXI) de l'INSA Lyon. Le système sCT est constitué d'un PCD de 700 pixels disposés en ligne, avec une tension de tube de 100kVp, un courant de tube de 100 µA et une résolution spectrale (en énergie) de 1 keV. Le détecteur a une capacité de résolution en énergie de 5 bandes d'énergie. Les plages d'énergie sont 30-39, 40-49, 50-59, 60-69 et 70-79 keV.

Le fantôme a été conçu pour être un grand cylindre en PMMA d'un rayon de 130 mm, qui a été creusé de 12 trous pour remplir les matériaux eau, Gd et I, comme le montre la figure 4.3. Pour le Gd, les concentrations ont été fixées séparément à 2, 4, 6, 8 mg/cc, et pour l'I à 1, 3,5, 7 et 14 mg/cc. Les 12 trous sont considérés comme les régions d'intérêt (ROIs), et les évaluations sont faites pour les ROIs.

La Figure 14(a) illustre la reconstruction originale par FBP pour cinq bandes d'énergie et les résultats projetés des quatre bandes vers la bande d'énergie 70-79 keV

dans la simulation. La Figure 14(b) montre les résultats de la reconstruction avec l'échelle d'affichage normalisée, y compris la vérité-terrain et les reconstructions à partir de FBP, TV et notre méthode pour le bande d'énergie de 70-79 keV. On peut observer que le résultat de notre méthode reste au même niveau que la vérité-terrain, et qu'il peut restituer les informations assez proches de la vérité-terrain.

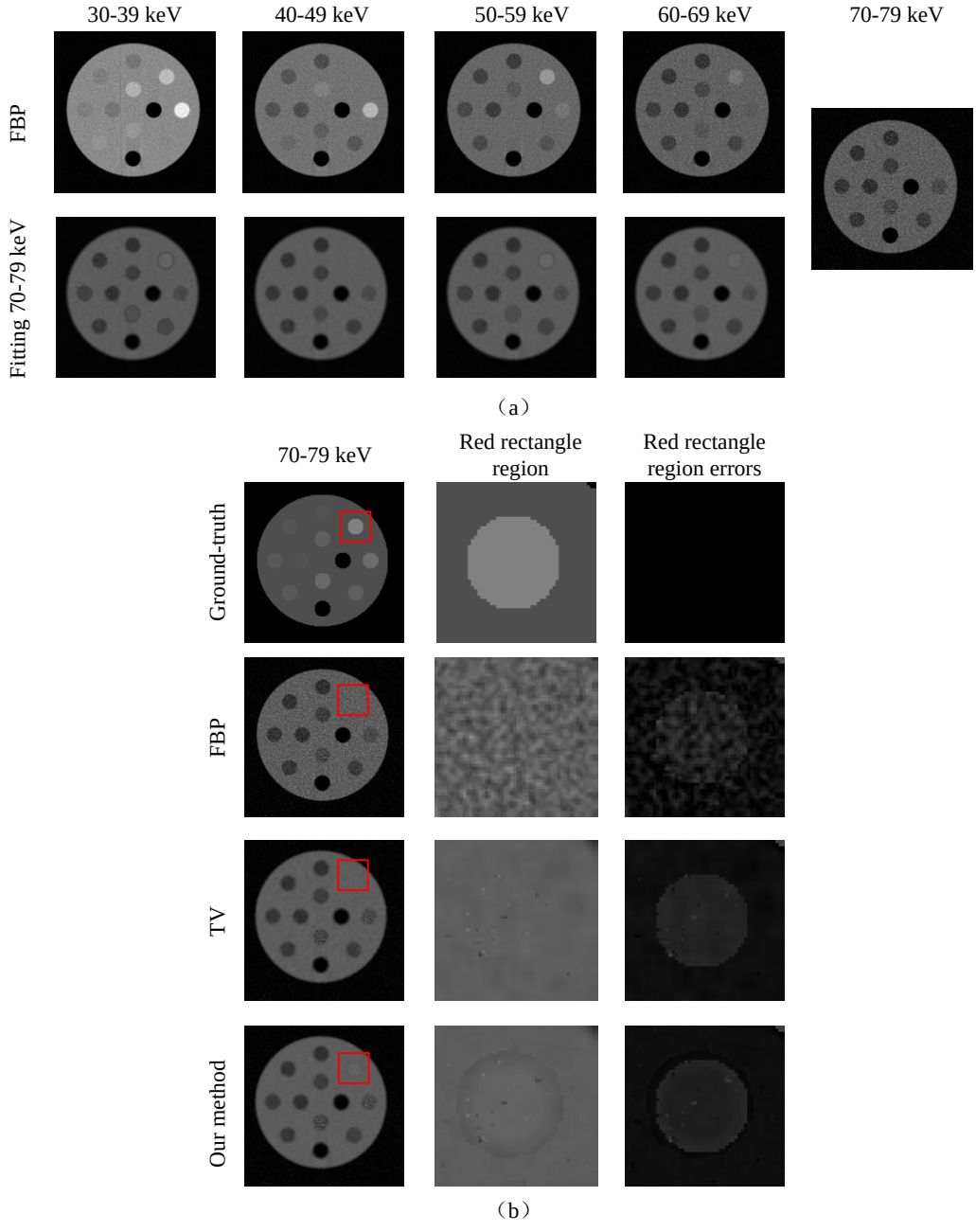

Figure 14 Comparaison de la reconstruction pour une bandes d'énergie de 70-79 keV.

Comme le fCT est l'une des applications les plus importantes du sCT, les résultats de la décomposition sont comparés sur la base des images spatiales reconstruites. La méthode de la norme L1 est utilisée pour décomposer les images spatiales reconstruites en eau, PMMA, I et Gd, comme le montre la Figure 15. On peut observer visuellement que les résultats de décomposition obtenus par nos méthodes d'ajustement contiennent moins de bruit et sont plus proches de la vérité-terrain.

Les données réelles sCT ont été générées par Phillips IQON. Le système est équipé de 924 PCD disposés en ligne. La distance de la source au centre de rotation est de 570 mm, et celle des détecteurs est de 1040 mm. La taille de l'image reconstituée est de , et chaque pixel correspond à . Le fantôme a été scanné par sCT avec le courant source à 220 mA, la tension source à 120 keV et l'angles de projection à 2400. La gamme d'énergie est divisée en 5 bandes d'énergie : 30-50, 51-61, 62-71, 72-80 et 81-150 keV. L'algorithme est validé à la fois sur fantôme physique et sur lapin in vivo.

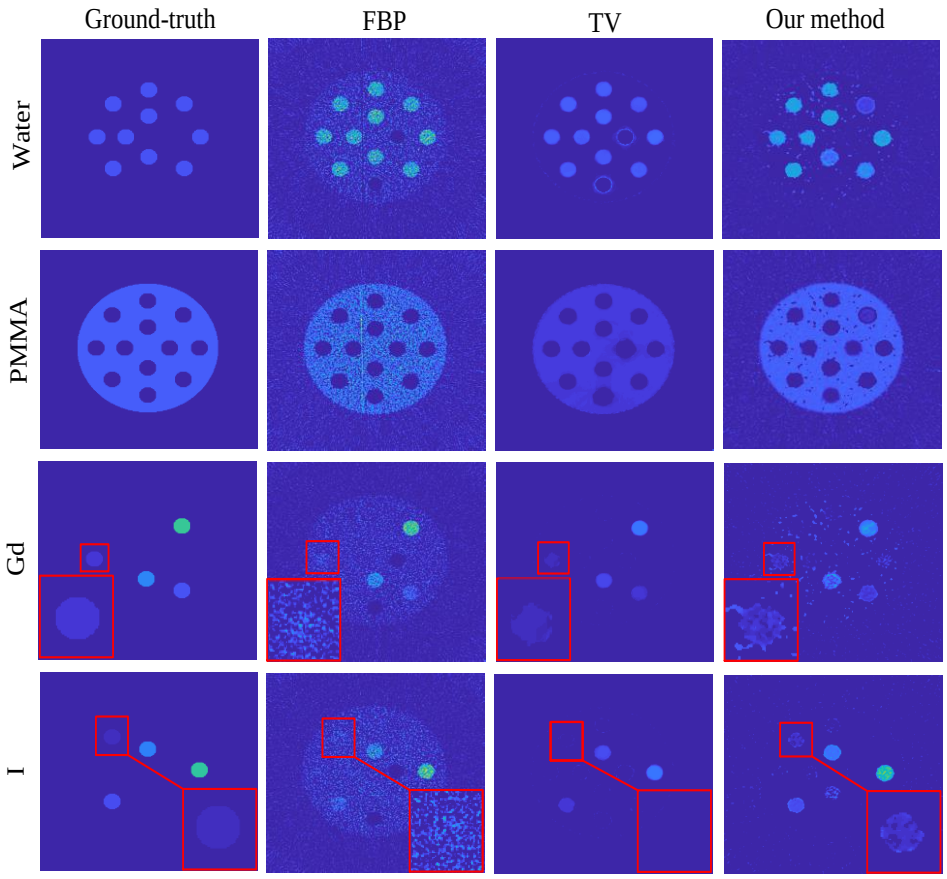

Figure 15 Comparaison de la décomposition de la reconstruction à partir de FBP, TV et de la méthode proposée.

Deux fantômes physiques (illustrés dans la Figure 16) respectivement remplis de Gd (ou I) et d'eau ont été utilisés pour évaluer les performances de notre méthode. La concentration pour Gd est fixée de 0.1 mg/cc à 15 mg/cc, et celle pour I est de 0.1 mg/cc à 15 mg/cc, comme indiqué par le chiffre dans chaque disque. La performance est évaluée en termes à la fois de la reconstruction et de la décomposition de matériaux.

(a) (b)

Figure 16 Fantôme physique: (a) I et eau; (b) Gd et eau.

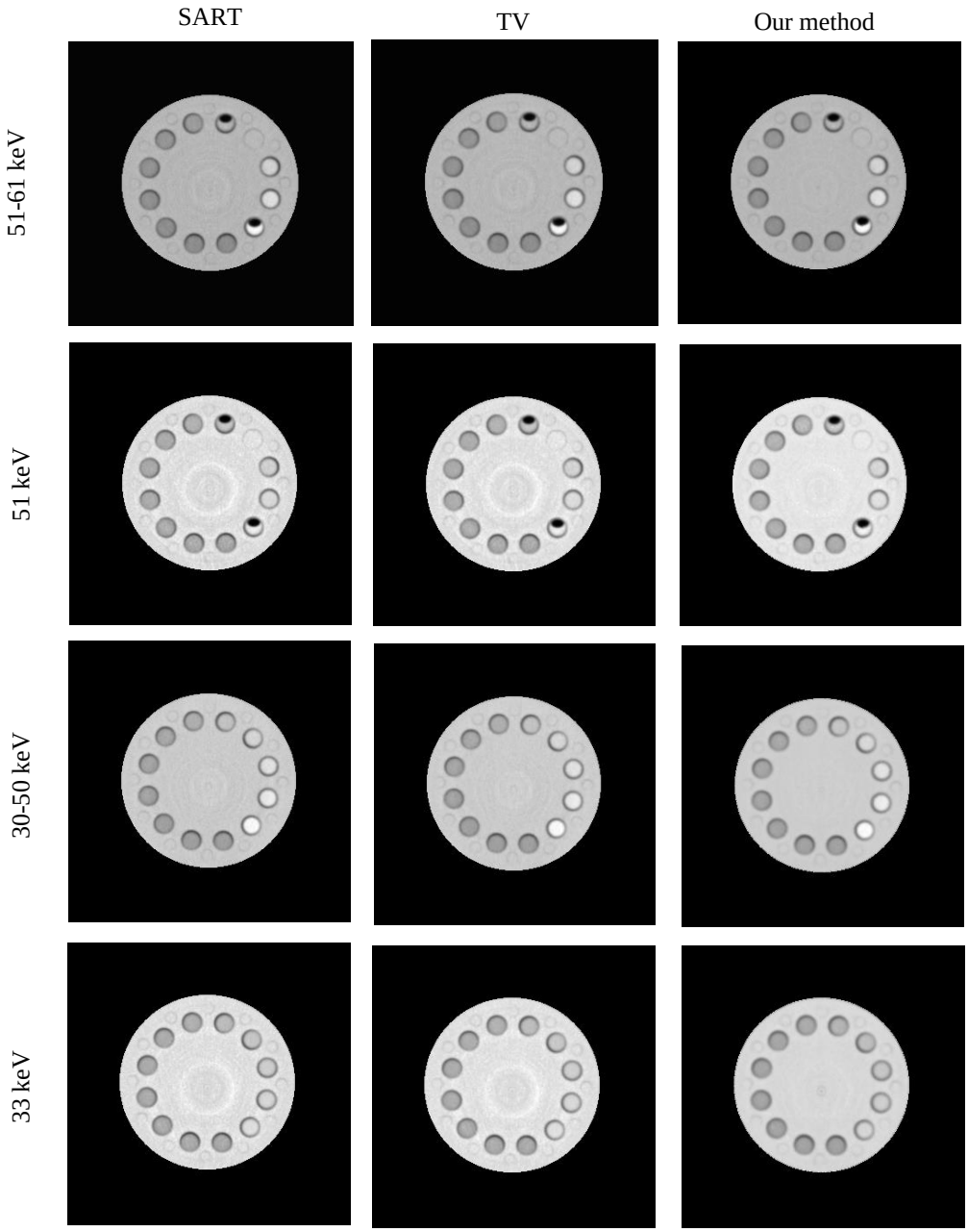

Figure 17 Reconstruction pour la bande d'énergie avec reconstruction du bord K et monoE du bord K pour Gd, I, respectivement.

La Figure 17 montre la reconstruction dans chaque bande d'énergie par SART, TV et notre méthode. En ce qui concerne la limite de la méthode d'acquisition des données, le sinogramme réel n'a pas pu être reconstruit par la méthode FBP. Les deux premières lignes montrent les résultats de Gd et les deux dernières lignes montrent la reconstruction de I, pour la case avec l'énergie du bord K et la reconstruction monoE du bord K. On peut observer qu'après avoir utilisé les informations provenant d'autres bandes d'énergie, le bruit de la reconstruction pour chaque bande d'énergie est visuellement réduit.

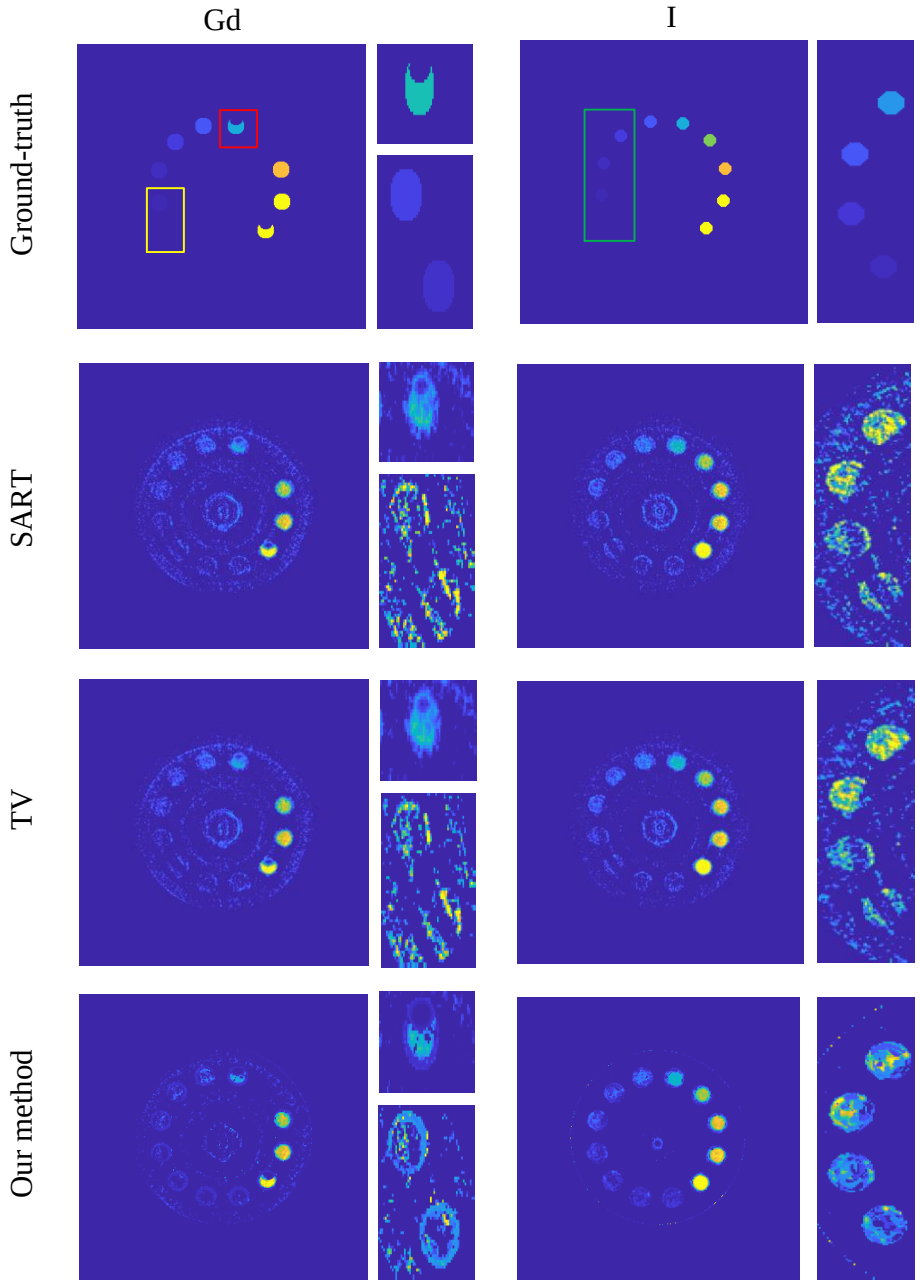

Figure 18 Résultats de la décomposition pour le fantôme physique avec Gd et I, respectivement. La colonne de droite pour chaque image est la région à faible concentration (rectangle jaune et vert) et de forme spéciale (le rectangle rouge) dans la forme agrandie. Les images de la même région pour toutes les méthodes sont affichées à la même échelle.

La Figure 18 présente la vérité-terrain du fantôme physique et les résultats de la décomposition de matériaux par l'ART, la TV et notre méthode. En même temps, les ROIs à faible concentration (rectangle jaune et vert) et de forme spéciale (rectangle rouge) sont zoomés. La fenêtre d'affichage est normalisée pour la même région. On peut observer que notre méthode est plus efficace pour les ROIs à faible concentration et de forme spéciale. Elle peut distinguer plus de pixels à faible concentration et fournir plus d'informations. Aussi, pour d'autres régions qui ne sont pas des ROIs, notre méthode réduit également l'artéfact dans une certaine mesure.

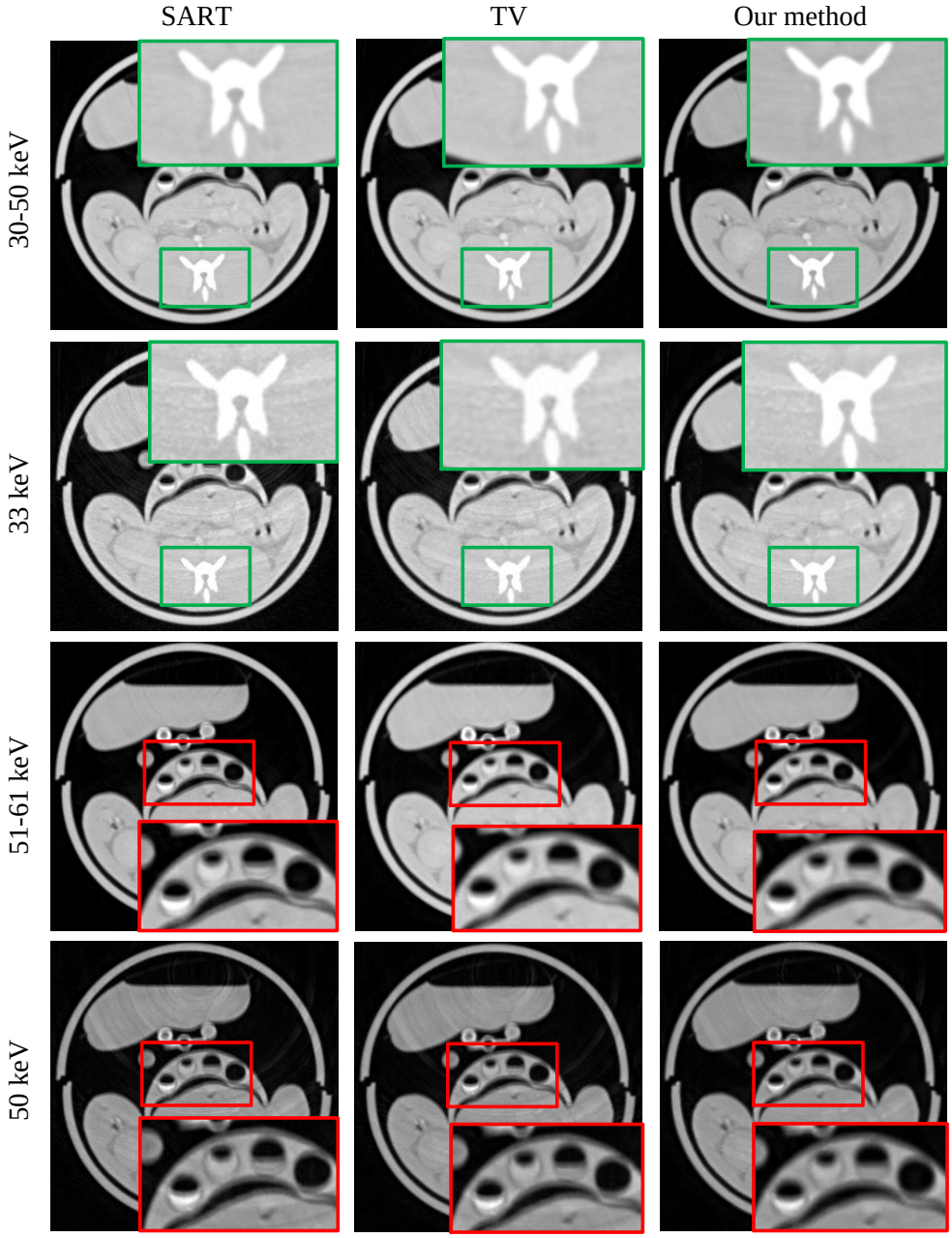

Figure 19 Reconstruction pour le lapin pour la bande d'énergie contenant le bord K et monoE pour le bord K, respectivement.

Le lapin a été injecté de Gd et fixé dans le conteneur pour être scanné. Les paramètres du système sCT sont réglés de la même façon que pour le fantôme physique. La Figure 19 montre la reconstruction à partir du sinogramme de 27-47 keV qui contient l'énergie du bord K de I et celui de 48-58 keV qui contient l'énergie du bord K de Gd. Pour la reconstruction d'une bande d'énergie, il n'a pas été possible de distinguer facilement la différence en raison de la grande plage d'énergie. Cependant, dans la reconstruction monoE, on a pu clairement observer que la reconstruction de notre méthode réduit les artefacts par rapport aux deux autres méthodes.

Les images sont décomposées en eau, Gd et I. Ainsi, le matériau ressemblant à l'eau (comme le plastique) sera décomposée en eau, et le matériau ressemblant à I sera en I (comme l'os dont la matière principale est le Ca). De plus, quatre tubes remplis de Gd à une concentration de 10, 5, 2 et 0 mg/cc (le rectangle de la Figure 20) sont fixés dans le récipient et scannés avec le lapin pour servir de référence. On peut observer que notre méthode souffre de moins d'artéfacts que les deux autres méthodes, surtout dans le matériau I (la deuxième rangée).

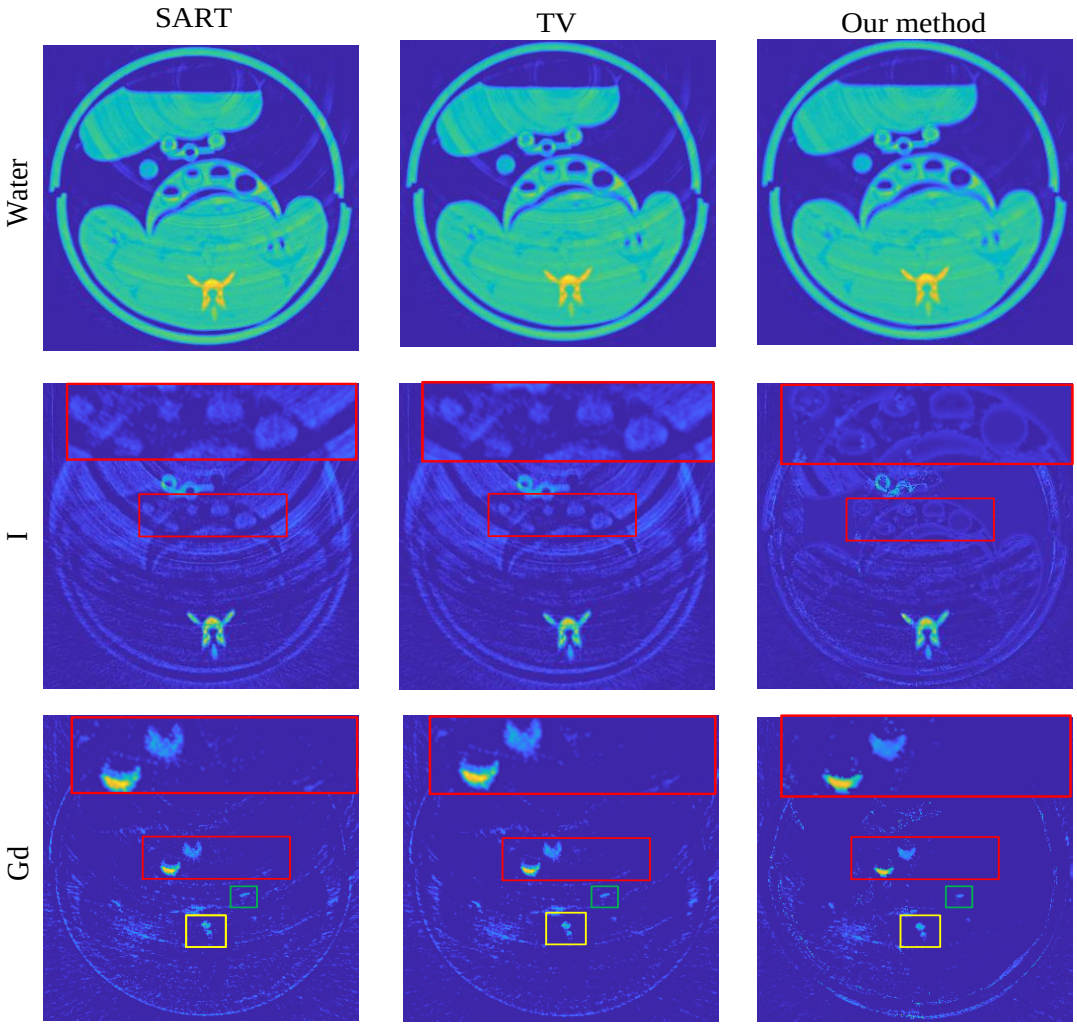

Figure 20 Résultats de la décomposition de matériaux du lapin injecté par Gd.

Conclusion

Nous avons proposé une méthode de reconstruction pour les images en sCT en exploitant des informations multi-énergie. Pour chaque bande d'énergie, nous reconstruisons l'image courante en utilisant aussi les images aux autres bandes d'énergie. Pour ce faire, nous classifions d'abord des pixels similaires en utilisant l'algorithme k-means. Ensuite, nous effectuons des ajustements linéaires entre deux images correspondant à deux bandes d'énergie, et ceci au sein de chaque classe. Ces ajustements linéaires se font deux à deux pour toutes les images correspondant à toutes les bandes d'énergie, ce qui conduit, pour une image courante (originale) à une bande donnée d'énergie, à plusieurs autres images (estimées) correspondant aux autres bandes d'énergie. A la fin, pour chaque pixel fixé, un filtrage (médian) dans la direction d'énergie génère l'image reconstruite finale, qui présente une meilleure qualité. Les résultats sur des données aussi bien simulées que réelles (fantôme physique et lapin) démontrent l'efficacité de la méthode proposée, qui montre de meilleures performances en termes à la fois de reconstruction et de décomposition de matériaux.

Chapitre 5: Reconstruction et débruitage simultanés dans sCT

Malgré leur vitesse de convergence, les méthodes itératives, qui permettent d'intégrer les connaissances connaissances a priori dans le processus de reconstruction, améliorent la qualité de la reconstruction, réduisent la dose et sont plus résistantes au bruit.

Une limite typique du sCT est que le nombre de photons disponibles dans chaque bande d'énergie est moins que le nombre total de photons détectés, ce qui entraîne une diminution considérable du SNR dans chaque bande. Dans ce chapitre, nous proposons d'introduire un mécanisme de débruitage explicite dans la reconstruction en ajoutant le filtre de débruitage dans la reconstruction interative, ce qui conduit à la méthode de reconstruction et débruitage simultanés pour les images sCT. Dans ce chapitre, nous suggérons d'utiliser les informations de chaque bande d'énergie et de toutes les autres bandes d'énergie comme termes de régularisation pour reconstruction et débruitage simultanés.

Méthodes

En tant que type d'image particulier, les images CT peuvent également être débruitées par toutes les méthodes des images naturelles. Pour la reconstruction et débruitage simultanés d'images sCT, la fonction objective est exprimée

$$\min_U \frac{1}{2}\|Y - AU\|_2^2 + \frac{\lambda}{2}\|U - F_U\|_2^2, \quad (5)$$

où F_U représente le terme de débruitage, λ est le paramètre qui équilibre le terme de fidélité des données et le terme de débruitage. Dans notre travail, quatre algorithmes de débruitage populaires sont introduits et compares, y compris le filtre guidé (GF-guided filter), la transformation en ondelettes (WT-wavelet transform), les moyennes non locales (NLM-nonlocal means), la correspondance par blocs et le filtrage 3D (BM3D-block-matching and 3D filtering).

Comme décrit au chapitre 4, la méthode de post-traitement proposée, qui utilise les informations multi-énergie pour débruiter chaque bande d'énergie, montre de meilleures performances que l'image originale. Par conséquent, elle pourrait être utilisée comme terme de régularisation dans la fonction objective de reconstruction et débruitage simultanés. L'opérateur de débruitage inter-bande est exprimé comme suit

$$\min_U \frac{1}{2}\|U - L_U\|_2^2, \quad (6)$$

où L_U donne l'opérateur de post-traitement présenté au chapitre 4. Par conséquent, en ajoutant à la fonction objective l'opérateur de débruitage inter- et intra-bande, on obtient le modèle de reconstruction et débruitage simultanés suivant

$$\min_U \frac{1}{2}\|Y - AU\|_2^2 + \frac{\lambda}{2}\|U - F_U\|_2^2 + \frac{\rho}{2}\|U - L_U\|_2^2, \quad (7)$$

où λ et ρ sont les paramètres qui équilibrent le poids du terme.

Pour accélérer la vitesse de convergence, nous utilisons l'algorithme de Bregman divisé pour optimiser la fonction objective.

Résultats

Le fantôme illustré à la Figure 3 a été utilisé pour la simulation. L'image reconstruite est de taille 160×160, et les paramètres λ, γ sont fixés à 20 et 100, respectivement. En prenant comme référence les coefficients d'atténuation théoriques, la Figure 21 montre les images reconstruites et les erreurs de reconstruction, avec différentes configurations: reconstruction directe sans débruitage, reconstruction et débruitage simultanés par GD, WT, NLM et BM3D. Il est évident les artefacts sont largement éliminés en utilisant reconstruction et débruitage simultanés que à la méthode de reconstruction directe. La Figure 22 illustre les profils des images reconstruites pour la bande d'énergie 50-59 keV, qui montrent aussi clairement que l'introduction d'un débruitage explicite dans la reconstruction permet d'obtenir des images reconstruites plus proches de la référence ainsi que des variances plus faibles.

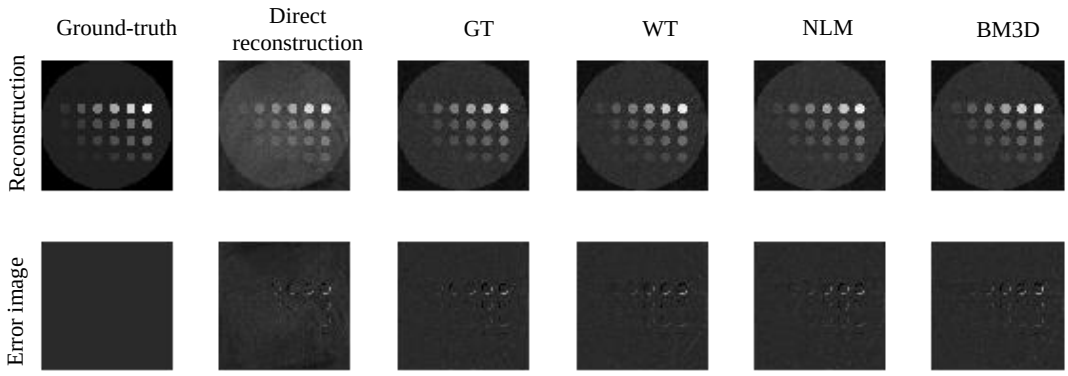

Figure 21 Images reconstruites (rangée du haut) et erreurs de reconstruction (rangée du bas). De gauche à droite : référence, reconstruction sans débruitage, et reconstructions avec GF, WT, NLM et BM3D, respectivement.

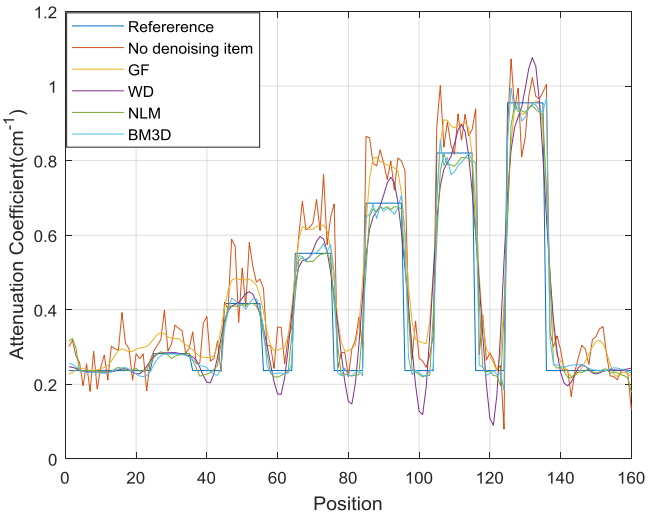

Figure 22 Les profils 1D selon les lignes dans Figure 21.

De manière plus quantitative, le Tableau 1 donne les valeurs RMSE et SNR des images reconstruites sans et avec débruitage. Les résultats montrent que les méthodes de reconstruction et débruitage simultanés permettent d'obtenir des RMSEs plus faibles et des SNRs plus élevés, quelles que soient les techniques de débruitage utilisées.

Tableau 1 RMSEs et SNRs des images reconstruites.

	Reconstruction directe	**Reconstruction et débruitage intra-bin simultanée**			
		GF	**WT**	**NLM**	**BM3D**
RMSE	0.0991	0.0707	0.0790	0.0692	0.0713
SNR(dB)	9.8028	13.5969	12.6393	13.7077	13.5551

Nous avons également comparé différentes méthodes de reconstruction en termes de performances de décomposition de matériaux, comme le montre la Figure 23. L'utilisation d'une des techniques de débruitage décrites ci-dessus tire avantage de la méthode de reconstruction directe à partir du sinogramme, en particulier pour le PMMA et l'eau, qui ont des coefficients d'atténuation similaires.

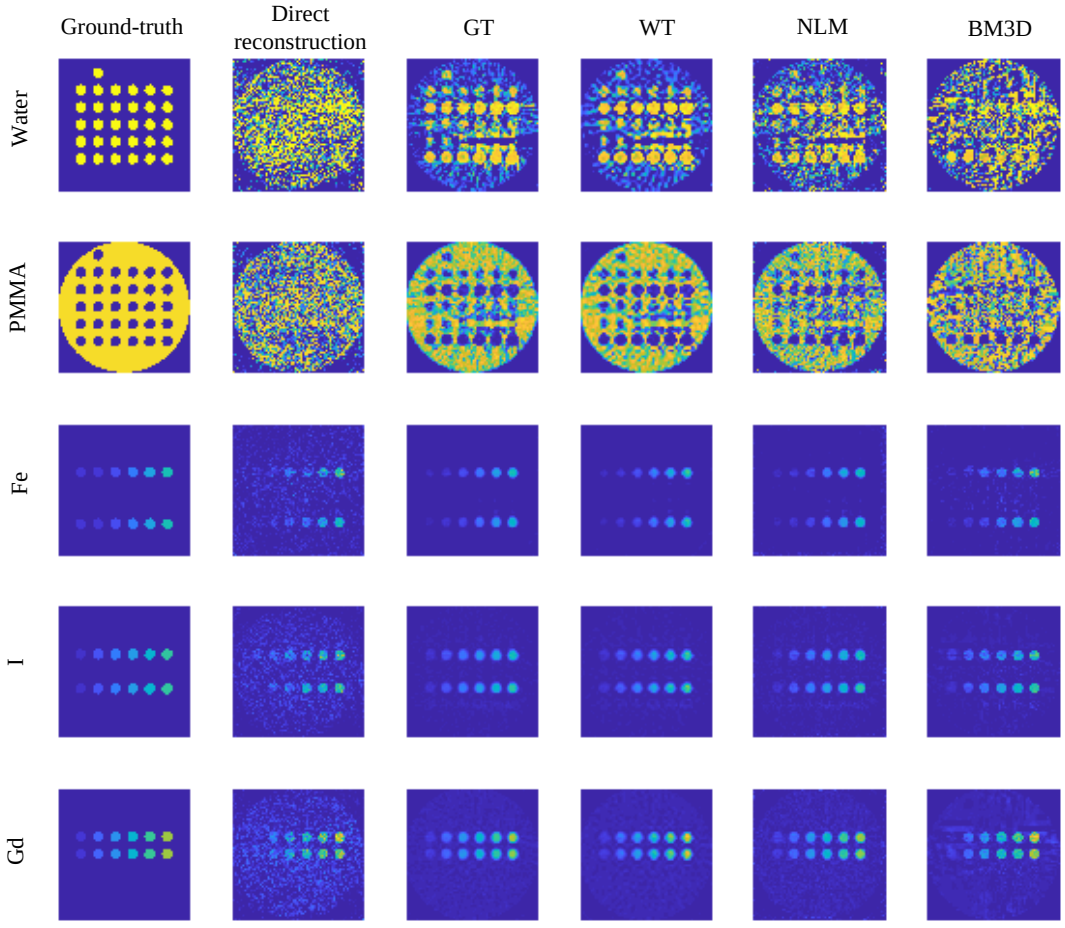

Figure 23 Comparaison de différentes méthodes de reconstruction en termes de performances de décomposition de matériaux. De haut en bas: PMMA, Eau, Fe, I et Gd. De gauche à droite: la vérité-terrain, reconstruction directe sans débruitage, reconstruction et débruitage simultanés

avec GF, WT, NLM et BM3D, respectivement.

D'après les résultats du débruitage intra-bande, les résultats avec les filtres NLM montrent de meilleures performances que les trois autres filtres. Ainsi, dans cette partie, la méthode de reconstruction et débruitage simultanés combinée intra et inter-bande vient d'utiliser le NLM pour la comparaison.

La Figure 24 montre la reconstruction et la comparaison des erreurs pour la bande d'énergie 50-59 keV à TV, reconstructions et débruitage avec NLM, et reconstruction avec un fonctionnement combiné intra-bande NLM et inter-bande. Nous observons que la méthode de notre thèse a une fonction efficace sur le débruitage, et à certains endroits, elle conserve les bords que la TV.

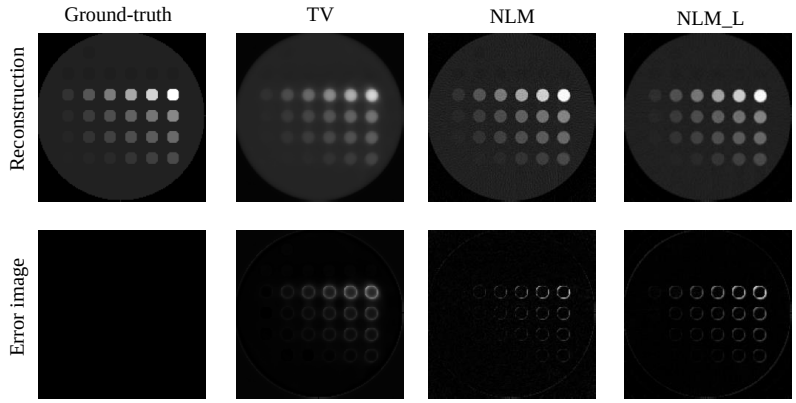

Figure 24 Images reconstruites (rangée du haut) et erreurs de reconstruction (rangée du bas). De gauche à droite : référence, TV, reconstructions avec NLM, et reconstruction avec opération combinée intra-bande NLM et inter-bande, respectivement.

Plus quantitativement, le Tableau 2 donne les valeurs RMSE et SNR de la reconstruction pour comparaison. Les résultats montrent que la reconstruction avec une opération combinée de NLM intra- et inter-bande obtient la RMSE la plus faible et le SNR le plus élevé par rapport aux autres méthodes.

Tableau 2 RMSE et SNR des images reconstituées pour TV, reconstructions avec NLM, et reconstructions avec opération combinée intra-bande NLM et inter-bande (NLM_L).

	TV	NLM	NLM_L
RMSE	0.0900	0.0692	0.0478
SNR(dB)	11.4790	13.7077	21.1451

Les résultats de la décomposition de matériaux pour ces méthodes sont également comparés, comme l'illustre la Figure 25. Bien que les résultats de décomposition de notre méthode ne soient pas aussi lisses que ceux de TV, ils sont plus proches de la vérité-terrain. La décomposition sur la reconstruction et le débruitage avec des filtres combinés inter- et intra-bande réduisent le bruit globalement, mais pour les matériaux sans bord K, comme I, les résultats ne sont pas aussi bons que la décomposition de la reconstruction avec la seule NLM.

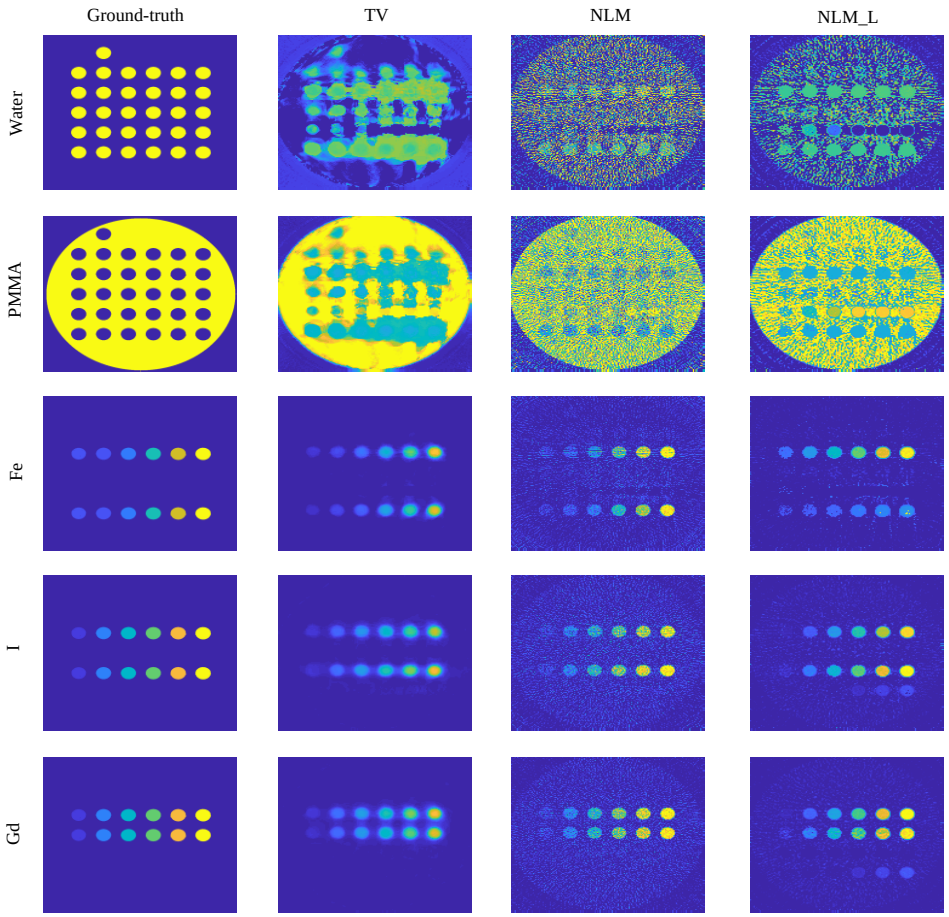

Figure 25 Comparaison de différentes méthodes de reconstruction en termes de performances de décomposition des matériaux. De haut en bas : PMMA, Eau, Fe, I et Gd. De gauche à droite : la vérité-terrain, TV, reconstructions avec NLM, et reconstruction avec opération combinée intra-bande NLM et inter-bande, respectivement.

Conclusion

Tout d'abord, nous avons proposé une méthode de reconstruction et débruitage simultanés pour les images sCT. Quatre méthodes de débruitage populaires, dont GF, NLM, WT et BM3D, ont été introduites dans la reconstruction. Leurs performances ont été évaluées à l'aide de la vérité-terrain, de la RMSEs et du SNRs. L'algorithme de Bregman fractionné a été utilisé pour accélérer la vitesse de convergence. Les résultats montrent qu'avec la combinaison de la reconstruction et du débruitage, les images reconstruites ont des RMSEs plus petites, des SNRs plus élevés et de meilleures performances dans la décomposition de matériaux.

Sur la base du modèle ci-dessus, nous avons introduit l'opération de post-traitement du chapitre 4 dans la fonction objective et construit un modèle de reconstruction et débruitage simultanés en utilisant les informations intra- et inter-bandes. Les résultats montrent une meilleure performance dans la reconstruction et une certaine amélioration dans la décomposition de matériaux, en particulier pour les matériaux avec un bord K.

List of Figures

List of Tables

Abbreviations

aCT	Anatomical imaging in CT
ART	Algebraic reconstruction techniques
BM3D	Block-matching and 3D filtering
CNR	Contrast-to-noise ratio
CT	Computed tomography
DECT	Duel-energy CT
EID	Energy-integrating detector
FBP	Filtered back projection
GF	Guided filter
monoE	Monoenergetic CT image
NLM	Nonlocal means
PCD	Photon-counting detector
PMMA	Poly(Methyl Methacrylate)
RMSE	Root mean square error
ROI	Region of interest
sCT	Spectral photon-counting CT
SNR	Signal-to-noise ratio
TV	Total variation
WT	Wavelet transform

Main Symbols

A	System matrix
I_0	Photon number generated by the X-ray source
I	Photon number received by the detector
E	Energy
U	Reconstruction images of sCT
Y	Sinograms of sCT
μ	Attenuation coefficient
μ_m	Attenuation coefficient
ρ	Density of the material
$\delta(\bullet)$	Dirac function
∇X	Gradient of X
$\|\cdot\|_2$	L2 norm
$\|\cdot\|_*$	Nuclear norm

General introduction

0.1 Problem statement and objective

X-ray computed tomography (CT) has evolved into an indispensable imaging method in clinical routine since its introduction by Cormack and Hounsfield in 1970s. It is the first method to non-invasively look into the inner structure of the object without physical operation, which makes it widely applied in medical, industrial, material and so on.

It is known that the conventional CT with single X-ray tube and energy integrating detectors (EIDs) measures the total photons through an object over the entire spectrum. Besides the anatomical information of the object, scientists are still interested in the composition material of the object, which is called the functional information. Motivated by this curiosity, dual-energy CT (DECT) is discovered, which improves the reconstruction quality and meanwhile makes it possible to look into the scanned object by two different spectral information. Due to that DECT only gets two set of data at one time, it has limited ability in the X-ray imaging application. Recent years, with the development of hardware, X-ray CT system mounted with photon-counting detectors (PCDs) appeared, which has the ability to distinguish the photons with different energies and measure them separately. This kind of CT system is named as X-ray spectral photon-couting CT (sCT). sCT enables to measure more than two sets of information of the scanned object at the same time, which can be further utilized to image reconstruction, image enhancement and material decomposition.

- Reconstruction in sCT. Thanks to the energy distinguish ability of PCD, sCT gets more than two measurement in one acquisition. However, the division of energy spectrum will also decrease the photons of each bin, which will make it sensitive to the noise. Therefore, denoising is an important topic in sCT reconstruction, which can be applied within one energy bin and across all the energy bins according to the attenuation property of the object.
- Enhancement in sCT. Considering the property of the attenuation coefficient of the material, for one energy bin, the contrast-to-noise ratio(CNR) is high but the signal-to-noise ratio(SNR) is low. While for another energy bin, on the contrary, the CNR may be low but SNR be high. By combining the information of different energy bins, an enhanced image with both higher CNR and SNR can be acquired, which is beneficial for the observation of the interested part.
- Material decomposition in sCT. As the attenuation information of multiple energy bins is provided by sCT, the material varieties and their corresponding concentrations are calculated by mathematical methods, which provides a glimps of the inner composition of the scanned object.

As the primary stage of sCT development, real data is rare for the research. Thus, in our work, a great many experiments on simulation are made to prove the effectiveness of the proposed method. Also, limited real data, including the physical phantom and the rabbit, are meanwhile utilized to validate the abilities of our mehod. Reconstruction and material decomposition results based on the reconstruction are employed to demonstrate the performances of our proposed method.

0.2 Main contributions

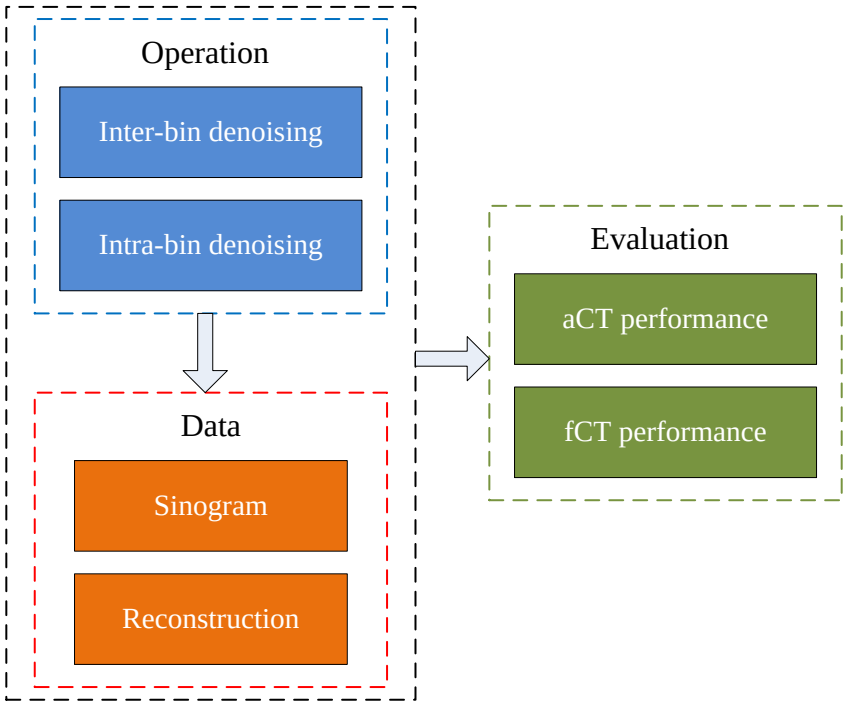

Figure 0.1 Contributions of the present work.

The main contributions of this thesis include: the exploration of the multimodel imaging of sCT in anatomical imaging (aCT) and fuctional imaging (fCT), a post-processing method combining the multi-energy information, and an iterative method integrating the denoising both within one energy bin and among all the energy bins. The information within one bin or among all the energy bins are applied on the sinogram or reconstruction to improve the image quality, whose results are evaluated with both aCT and fCT performance. In the following, we detail the contributions from the three aspects.

- Multimodel imageing of sCT (Chapter 3).

  Exploration of the sCT ability to achieve simultaneously both aCT and fCT in one single acquisition through reconstruction and material decomposition. aCT function of sCT is studied under the same configuration as that of conventional CT, and fCT function of sCT is investigated by applying material decomposition algorithms to the acquired multi-energy data.

Selection of the energy bin number to balance the performance of reconstruction image and material decomposition image for sCT. For the same range of energy width, more bins mean narrower bin width, which will result in sensitivity to the noise. However, more bins will at the same time provide plenty of information for material decomposition, which will benefit the material decomposition. Thus, simulation was made by setting different number of energy bins. The results from both reconstruction and material decomposition were compared, which reconmmends 5 or 6 energy bins for sCT.

- Reconstruction utilizing multi-energy information in sCT (Chapter 4).

  The X-ray CT system usually directly displays the reconstructed images, but with large noise. We propose an image-to-image method, which is based on the primarily reconstructed image and utilizes the relationship of the attenuation coefficients for different energy bins to improve the image quality. As discovered, the attenuation of the similar material composition pixels shares the similar linear relationship among every two energy bins even with various concentrations. This idea is to cluster the pixels with similar variation rule of attenuation coefficient among all the energy bins, make a fitting with the cluster results, and utilize the fitting results to denoise the reconstruction for each energy bin. The proposed method is applied to the images already reconstructed by other methods.

- Simultaneous reconstruction and denoising in sCT (Chapter 5).

  We propose a sinogram-to-image model for sCT imaging, including the intra-bin denoising, combined intra- and inter-bin denoising.

  Intra-bin denoising. The narrow bin width of the sCT will increase the noise for each energy bin. One idea is to add the denoising item to each energy bin in the process of reconstruction, namely the intra-bin denoising. In our work, four most popular denoising filters, including the Guided Filter (GF), Wavelet Transform (WT), Non Local Means (NLM), Block-matching and 3D Filtering (BM3D), are added as a regularization of the objective function to improve the reconstruction quality.

  Combined intra- and inter-bin denoising. The relationship of the attenuation coefficients for each energy bin is employed as a regularization term in the reconstruction objective function, namely the inter-bin denoising. In our work, as the method described in the above multi-energy based reconstruction functions in the improvement of the image quality, this item is introduced as the inter-bin denoising regularization term. The filters, which are responsible for intra-bin denoising by the information within the energy bin and inter-bin denoising out of the current energy bin, are both added as regularization terms in the reconstructed objective function for simultaneous reconstruction and denoising.

0.3 Organization of the thesis

The manuscript is organized as follows:

In Chapter 1, entitled “X-ray computed tomography (CT) and spectral CT (sCT)”, the principles of the interactions of X-rays with matter are introduced, including photoelectric absorption, Compton scattering and pair production; the development and the principles of X-ray CT are described, including the conventional energy integrated CT, DECT and sCT.

In Chapter 2, entitled “Reconstruction of sCT images”, a review of the existing reconstruction methods for CT is presented, including the analytical method, iterative methods and learning methods. For each kind of methods, one or several representative methods are introduced in detail. Some of these methods are also utilized in the following chapters.

In Chapter 3, entitled “Multimodel imaging of sCT”, the multimodel imaging ability of sCT is introduced, including aCT and fCT in one single acquisition through reconstruction and material decomposition. aCT function of sCT is studied under the same configuration as that of conventional CT, and fCT function of sCT is investigated by applying material decomposition algorithms to the acquired multi-energy data. In addition, the number of energy bins of the CT system is discussed to balance the quality of reconstruction and material decomposition.

In Chapter 4, entitled “Image reconstruction using multi-energy information in sCT”, a post-processing method cooperating the relationship among each energy bin is introduced. The method is validated on simulation, physical phantom and rabbit data to demonstrate its performance.

In Chapter 5, entitled “Simultaneous reconstruction and denoising in sCT”, an iterative method integrating the denoising both within one energy bin and among all the energy bins is presented and validated on simulation and physical CT.

In the final, entitled “Conclusion and perspective”, a brief summary of the main results, the conclusions and future perspectives are presented.

Chapter 1 X-ray computed tomography (CT) and spectral CT (sCT)

Abstract

In this chapter, we first introduce the general attenuation principle of X-ray CT and the basic compositions of the X-ray CT system. The development of the hardware technology stimulates the X-ray CT system to extend from conventional CT to duel-energy CT and then to spectral CT. The key advance is the invention of photon-counting detectors, which has the ability of energy discrimination compared with the energy-integrating detectors. Spectral CT makes it possible to look into the nature which causes the attenuation of X-rays, and it shows potential applications in image reconstruction, material decomposition and image enhancement.

1.1 X-ray computed tomography (CT)

1.1.1 Basis of X-ray CT

CT has become one of the most popular methods in medical diagnosis. Although X-ray has already been applied to radiography, it can only get the image of superposition structure. Owing to the work of Cormack and Hounsfield in the last century, CT can collect the information of the scanned object from multiple angles, which makes it the first method to acquire the inside structure of the human body without superposition explicit physical trauma. Therefore, CT displays much more details in advantage of the radiography.

Since the first occurrence of CT instrument for the brain examination in 1972, it has been applied to all the body, including the chest, abdomen, spine and limbs. In the past years, with the development of hardware technology, CT instrument has expanded both in the scanning and detecting method. The early X-ray CT instrument utilized the rotating/translating method to scan the object and collected the information with just 1~2 detectors, which could only acquire limited data, require long time cost and obtain images of poor quality. Later, the progress of hardware makes it possible to utilize more than 1000 detectors and the advance of scanning method allows to finish the scan within the time level of by the rotate/stationary mode, which as a result makes it reconstruct the image of the scanned object with high quality and resolution within short time. Due to the rapid development and convenient utilization of X-ray CT, it has now been applied to many aspects, including medical, industrial, material, and so on.

1.1.2 Principles of CT

1.2.2.1 CT system

The X-ray CT system mainly consists of three parts: the source generates the photons of specific distribution under the given parameters; the detectors receive the photons penetrating the object, and the computing system for the information process, as shown in Figure 1.1.

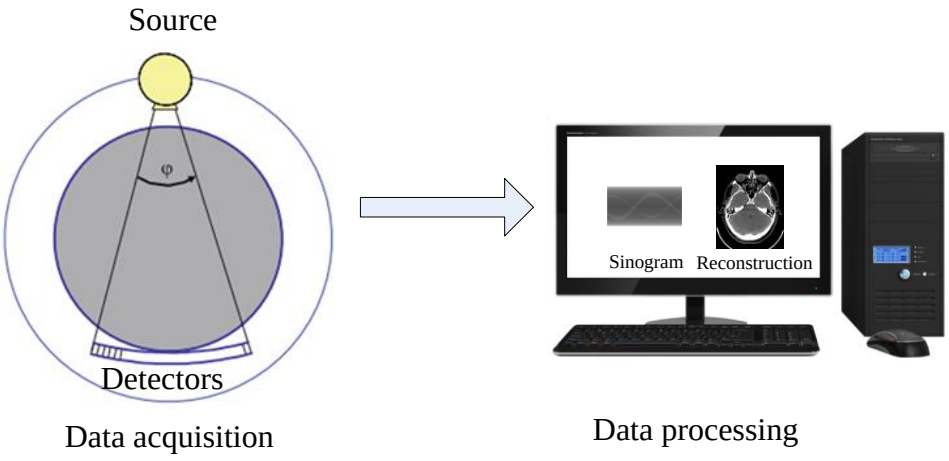

Figure 1.1 CT system.

- Source

X-ray radiation actually is a kind of electromagnetic, whose wavelength is defined from 10^{-8} to 10^{-13} m in the electromagnetic spectrum. The generation of the X-rays in CT is shown in Figure 1.2. First, the electrons are heated to almost 2400K through the cathode filament. Under the source voltage U_a added on the two ends of the source, the thermal electrons are accelerated with high speed. However, when entering the anode material, the speed of these electrons will decrease, which generate the X-ray radiation.

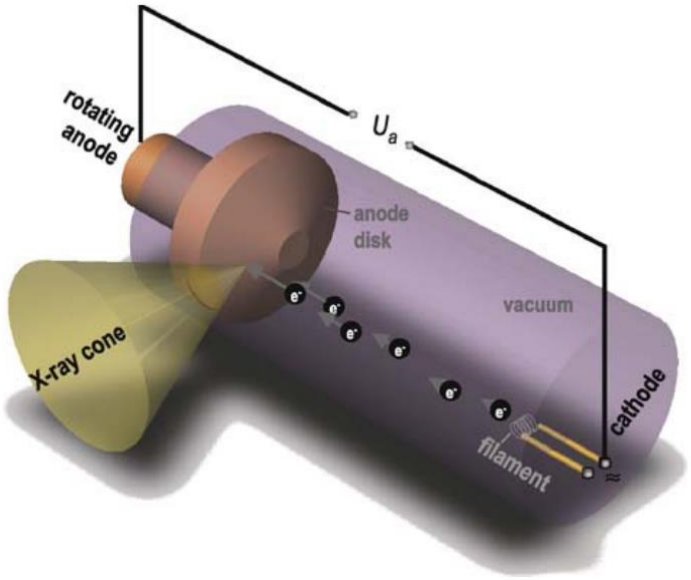

Figure 1.2 X-ray generation (Figure retrieved from (M 2008)).

The distribution of the X-ray photon energy depends on the source voltage. Generally, the maximum of the energy is . As the most of the photons in low energies have weak penetration, they are more likely to be absorbed by the scanned object; while the photons with high energies are more likely to penetrate the object and reach the detectors. Thus, in practical CT system, in the front of the object there will be a filter, which removes the photons with low energies.

Figure 1.3 shows the distribution of the X-ray under the source voltage of 80, 100, 120 and 140 keV, respectively. Each distribution has several peaks in the photon numbers within the energy range. These peaks are caused by the interaction of the incident electrons with the orbital electrons, which is called the characteristic of X-rays. Also, With the increase of the source voltage, the photons generated from the source increases, and the photons of the peak energy becomes more obvious.

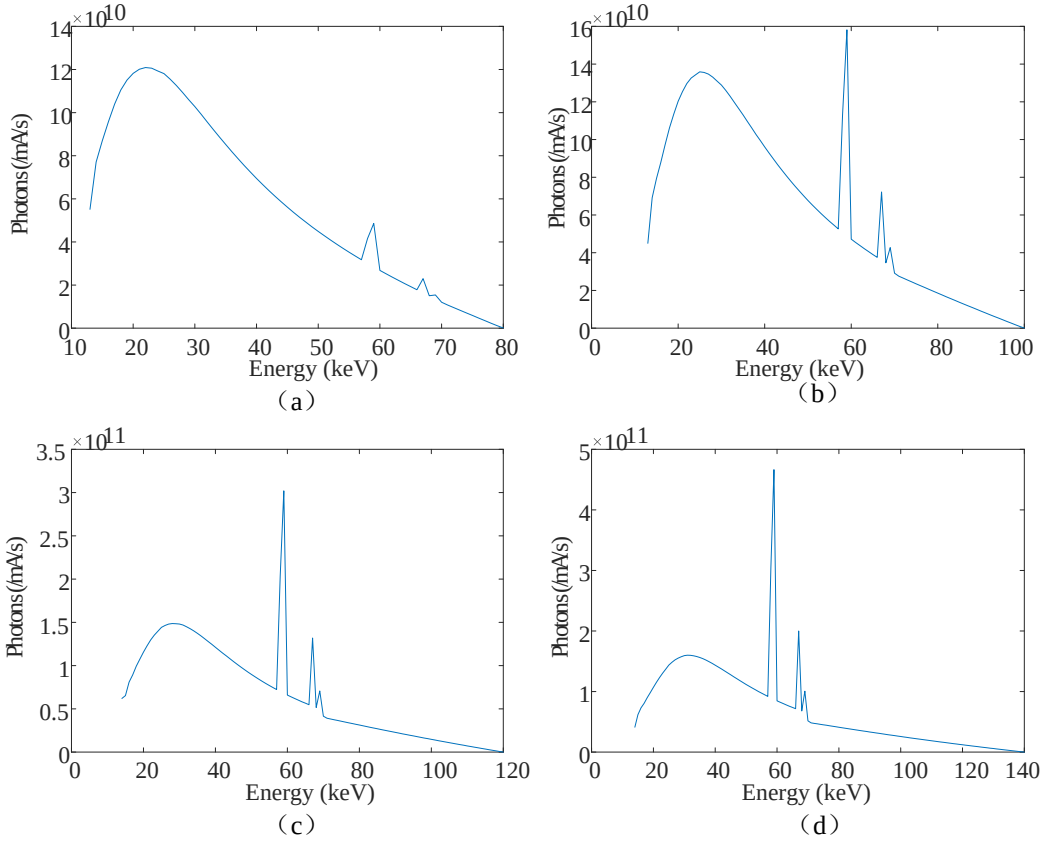

Figure 1.3 Photon distribution in simulation under 80, 100, 120 and 140 keV, respectively. With the increase of the source voltage, the photons generated from the source increases, and the photons of the peak energy becomes more obvious.

- Detectors

When X-rays penetrate an object, due to the photon-matter interaction, the energy and number of photons through the object will decrease. These photons are measured by the detectors opposite to the source and form the signal containing the information of the object. There are mainly two types of detectors: EID and PCD. EID measures all the photon information without discrimination, namely providing the integrated information of the transmitted beam; while PCD owns the ability of energy discrimination, which makes it possible to count the photons with different number separately. It is also the development of the detector that stimulates the evaluation of sCT, which is introduced in detail in section 1.2.

- Computing system

The computing system is to process the information from the source and detectors, and provides the useful information for further analysis, which is usually displayed by image. The form process of the conventional CT image is as follows: firstly the slice is divided into several cuboids of equal volume, which is the so called voxel; then the scanned information is calculated to acquire the attenuation coefficient for each pixel for the X-rays, and they are arranged as matrix; finally, the matrix is displayed by the block ranging from dark to white according to the values, namely pixel, which is the CT image.

The working process of X-ray CT is as follows: according to the different absorption and transmissivity of human tissues, the detectors of high sensitivity are applied to measure the photons of each X-ray, and all the information is input to the computer for processing. Then, the image of the scanned slice or volume is reconstructed to discover the tiny lesion of the human body. However, due to the slight difference of the human tissue for the X-rays, it is often difficult to distinguish the tiny lesion. Therefore, reconstructing CT image of high quality is a significant problem for improving the diagnosis accuracy.

1.1.2.2 Photon-Matter interaction

With very high, material-dependent capability of matter penetration, the X-ray can penetrate the scanned object. However, due to the absorption and scattering, the number of photons, i.e., the radiation intensity, decreases exponentially while running through an object along the incident direction.

As illustrated in Figure 1.4, all the physical mechanisms that leads to the reduction of photons measured by a detector behind the object are usually to be described by a single attenuation coefficient μ. The radiation intensity after passing through an object is determined by

$$I_{\eta+\Delta\eta} = I_\eta - \mu_\eta I_\eta \Delta\eta \,, \tag{1.1}$$

By reordering this equation and taking the limit, we can get

$$\frac{dI}{I_\eta} \lim_{\Delta\eta\to 0} \frac{I_{\eta+\Delta\eta} - I_\eta}{\Delta\eta} = -\mu_\eta I_\eta \,, \tag{1.2}$$

Integrating of both sides, Equation (1.2) is transformed to

$$I_\eta = e^{-\mu\eta + C} \,, \tag{1.3}$$

where C is the constant determined by the initial condition. With the initial condition I_0, it is written as

$$I_\eta = I_0 e^{-\mu\eta} \tag{1.4}$$

This is the well-known Beer's law of attenuation. Thus, in one CT scan, denoting the photon number reaching the detectors as I, the penetrating length of the X-ray as L, if the object is made by the material with various attenuations, Beer's law is expressed as

$$I = I_0 e^{-\int_L \mu dl} \,, \tag{1.5}$$

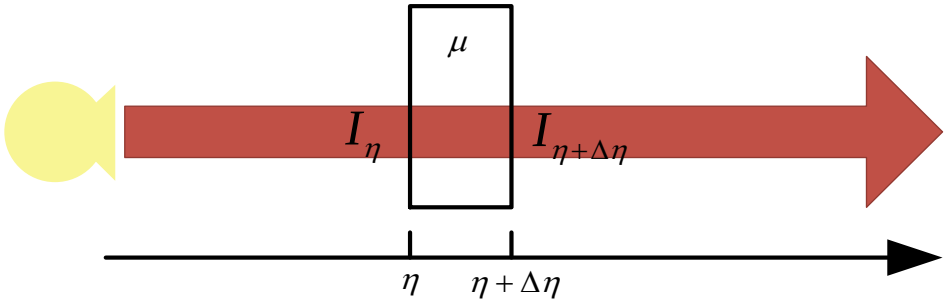

Figure 1.4 Mathematical model of the X-ray attenuation.

Beer's law indicates the reduction of X-ray photon numbers when penetrating the object. The exponential reduction in photon number is resulted from the interaction of the photons and the object, of which the most important functions are Compton scattering, photoelectric absorption, and pair production.

- Photoelectric absorption

Photoelectric absorption describes the interaction of the X-ray with the inner shell of the atom. If the binding energies of atomic electrons are smaller than the energy of the incident X-ray photon, the X-ray photon can be absorbed by the atom. Then, the electron of a lower shell is kicked off the atom and escapes through the material in the form of a free photoelectron, as shown in Figure 1.5. A K-shell interaction is more possible to happen than the outer shell if both interactions are satisfied, where more than 80% of the photoelectric absorption happens.

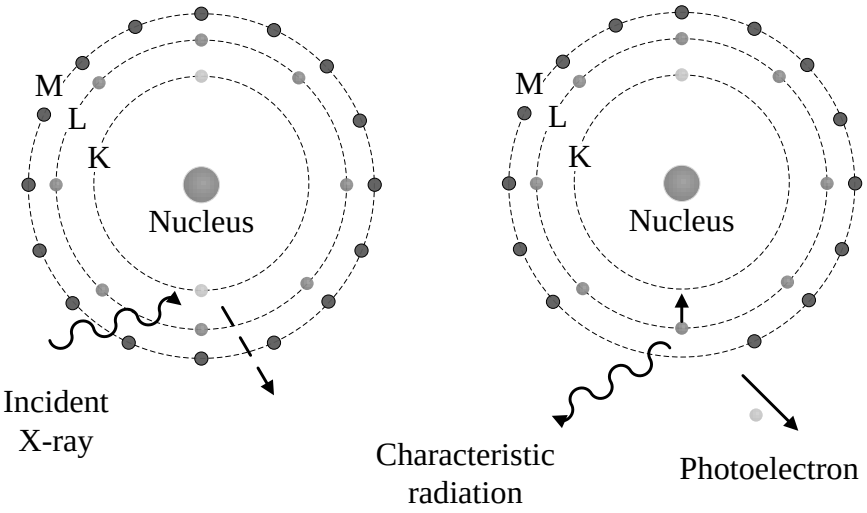

Figure 1.5 The first two stages of the photoelectric absorption. The incident X-ray interacts with the electrons in the inner shell of the atom. The energy is absorbed and ejects the photoelectron. The electron in the outer shell will transferred to fill in the vacancy in inner shell. Almost all of the energy of the incident X-ray is transferred to the ejected photoelectron (Figure inspired by (M 2008)).

The interaction of photoelectric will also result in unstable structure of the atom due to the vacancy in the particular shell. Thus, the electron originally in the outer shell of the atom will transfer to fill this position and at the same time generate the characteristic radiation of the X-ray line.

- Compton scattering

Different from photoelectric absorption, Compton scattering is the interaction of the X-rays with the outer shell of the atom. When the incident X-ray photon is with the energy much more than the binding energy, Compton scattering occurs: the energy of the incident X-ray photon will reduce, the direction will change and the electrons in the outer shell of the atom will be ejected, as illustrated in Figure 1.6.

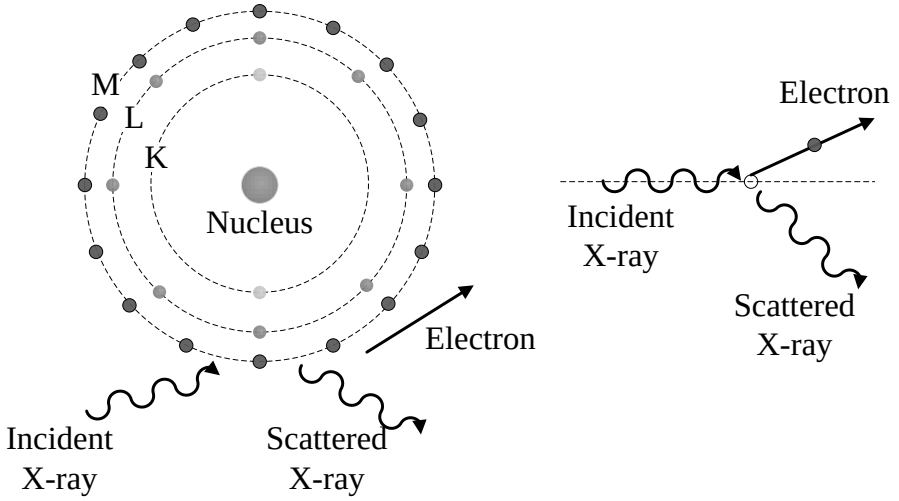

Figure 1.6 Compton scattering interaction (left). In this process, the energy of the incident X-ray photon will reduce, the direction will change and the electrons is generated (Figure inspired by (M 2008)).

- Pair production

When the energy of the incident X-ray photon is more than 1.022 MeV (the mass energies of one electron and one positron), it is possible to generate the pair production effect. This interaction happens between the X-ray photon and the nucleus of the atom, which will generate an eletron-positron pair. The electron and positron will meet each other after a very short travelling length according to the schematical pattern, which makes the pair annihilation and generate the X-ray lines.

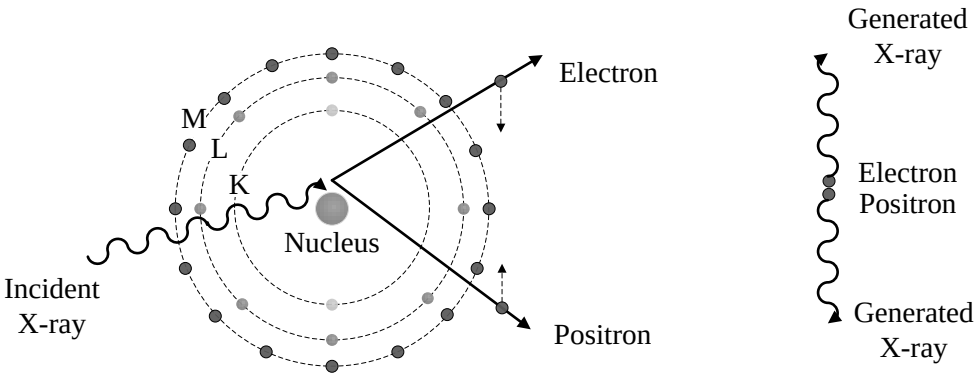

Figure 1.7 Two stages of the pair production photon-matter interaction. The first stage is to generate a pair of electron and a positron (left), and the second stage is to generate new X-ray lines when the pair annihilation happens (Figure inspired by (M 2008)).

Also, their exists other photon-matter interactions, including the Thomson scattering, photo disintegration and so on, which all contributes to the attenuation of X-ray penetrating the object. In these interactions, the photoelectric absorption is the main reason for X-ray attenuation, and other effects mainly bring in the noise in the process.

1.2 Spectral CT (sCT)

1.2.1 Development of sCT

As a particular X-ray imaging technique, X-ray CT enables imaging three-dimensional (3-D) structures of the object and plays an indispensable role in medical imaging, industrial control and security check. Historically, CT was used to gain knowledge about the anatomy of organs; we can call these conventional CTs the anatomical CT (aCT). Later, dual-energy CT (DECT) became available (Alvarez and MacOvski 1976a) with technological developments in fast kVp-switching, dual-source CT and dual-layer detectors (Macovski et al. 1976; Marshall, Alvarez, and Macovski 2014; Noh, Fessler, and Kinahan 2009; Sukovic and Clinthorne 2002). Compared to conventional aCT, DECT provides the possibility of obtaining information about the composition of materials. This makes it widely used in medical analysis, such as abdominal imaging (Dac, Shaping, and Elements 1997; Graser et al. 2009), Achilles tendinopathy and partial tear diagnosis (Mallinson et al. 2013), and so on (Karçaaltincaba and Aktaş 2011)(Johnson et al. 2007). However, DECT separates energy spectrum only into two parts and thus provides only two measurement points on the X-ray attenuation curve, which limits considerably its ability to distinguish more materials. Moreover, DECT often requires the registration of acquired data if motion is present during acquisitions (Taguchi et al. 2010).

More recently, owing to advances in photon-counting technology, which allows counting photons in short time, a new kind of CT, called the spectral photon-counting CT, is emerging (Iwanczyk et al. 2007). We call it simply spectral CT (sCT). Compared to DECT, sCT uses three or more energies (or more exactly energy bins; an energy bin corresponds to an interval of energies). Equipped with photon-counting detectors, sCT divides the whole energy spectrum into small energy bins using multiple energy thresholds and counts the number of photons in each energy bin separately, thus making

it possible to generate multiple images corresponding to different energy bins in one single acquisition. In such way, sCT produces rich information for distinguishing energy-related characteristics of the object and offers sufficient information for separating more than two materials composing the object (Fletcher et al. 2015; Katsuyuki and S. 2013; Liu et al. 2016). Compared to DECT, sCT presents the advantages of quicker acquisition, higher efficiency, more energy bins, and more flexibility for data processing (Taguchi et al. 2010).

1.2.1.1 Conventional CT

Conventional CT utilizes one X-ray source to generate the photons whose number obeys specific distribution under the given system parameter, and integrating detectors are arranged in an array in the opposite position to receive the photons penetrating the scanned object. Conventional CT utilize the EIDs which count all the photons of different energies they receive. Therefore, for one scan, one pair of data (the photons generated by the source and received by the detectors) is acquired for the CT image reconstruction. Conventional CT reconstructs the image according to the differences of the attenuation coefficient of the object. Therefore, in medical diagnosis, it has good performance to distinguish the tissues with obvious attenuation coefficient difference. However, for the tissue with the same or similar attenuation coefficient curve, it is difficult to tell them apart. Thus, it is essential to develop a novel imaging method which can effectively distinguish the tissue and analyze the material component of the object.

1.2.1.2 DECT

In 1976, Akvarez first proposed the DECT, which utilized two kinds of X-rays to scan the object and reconstructed the image of the electron density and effective atomic number for the scanned object (Macovski et al. 1976). However, it is not widely applied due to the limit of the CT instrument. In 1979, Lelcz proposed the implementation model of two DECT, namely the "two crystal" technique which utilizes a split crystal detector simultaneously to obtain the high and low energy data in one scan, and "two kV" technique which scans twice with low and high kV respectively. Meanwhile, Lelcz drew the conclusion through theory calculation that the "two kV" technique could get better performance compared with the "two crystal" technique. In 2005, Phillips succeeded in utilizing the two-layer system on the Brilliance 64 CT scanner, which is the leap for the DECT system. This kind of DECT is easy to implement, but due to the limit of the filter ability, it is difficult to distinguish the low energy and high energy spectra, which causes non-negligible errors in the reconstruction (Kappler et al. 2009). In 2006, Siemens invented the first dual source CT (Somaton Defintion-Flash), which integrated the X-ray tube with two different energy and detectors into one system. The system completes the data collection under different tube voltage and current, which makes it possible to acquire the image data simultaneously, improve the accuracy of image registration and realize the material separation. In 2007, GE introduced the Discovery CT750 HD DECT system, which employed the detectors made up of

gemstone and improved the stability of the data acquisition process. The system could quickly complete the switch between the low energy and high energy and acquire the data at the same time and same angle.

By utilizing the attenuation characteristic of the object under different energies, DECT gets the reconstruction image and distinguishs the material effectively. Compared with conventional CT, DECT shows better performance in removing the beam-hardening artifacts and improving the reconstruction image quality. What's more, DECT utilizes the information for analyzing the material composition and their concentration quantitatively, which offers the possibility to detect the internal composition of the scanned object.

However, DECT just employed two attenuation features of the scanned object, which limit it to just analyze two kinds of material composition. In reality, for the scanned object, more kinds of material and their concentrations are required for medical diagnosis. To satisfy this requirement, sCT occurred.

1.2.1.3 sCT

Recent year, the development of the detector stimulates the evolution of sCT (also named as multi-energy CT), which enables to detect the photons of different energy separately due to the novel kind of detectors. Different from conventional CT and DECT, sCT employs the PCDs to collect the information.

- Principle of PCDs

Figure 1.8 shows the principles of EID and PCD, respectively. In EID, the incident X-rays hit the upper scintillator and are converted into visible light. Then, the generated visible lights are absorbed by a photodiode made of a semiconductor material, which measures the amount of the incident light and creates an electrical signal proportional to the total energy. Different from EID, PCD does not contain the scintillator layer but is made by a semiconductor diode with a large voltage applied on. When the incident X-rays reach the semiconductor, it generates a cloud of positive and negative charges. These charges are pulled away under the force of the voltage rapidly and generate an electrical pulse, which is readout by a electronic circuit.

In summary, compared with EID, PCDs will directly convert the X-ray photons to electric signals and this results in higher photon detecting ratio compared with EIDs, which first convert the X-ray photons to visible light and then to electric signals (Willemink et al. 2018).

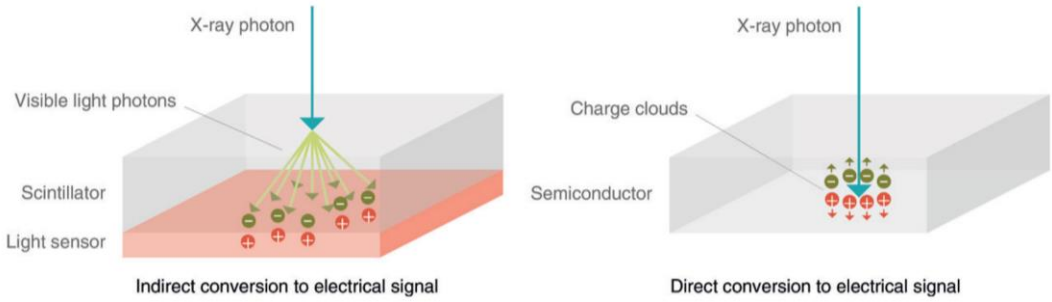

(a) (b)

Figure 1.8 Comparison of EID and PCD (Figure form (Willemink et al. 2018)).

The photons striking the detector generate electrical pulses, whose heights are proportional to the energy of the photon. The number of these pulses is counted by the electronics system with set thresholds, whose range is set between the electronic and the height of the pulses. Therefore, in PCDs, the photons are classified into different classes (namely the energy bin) according to their energies by comparing the generated electronic pulse with the thresholds. Meanwhile, in this mechanism, the electronic noise availably is removed from the photon pulse because of the higher threshold (Willemink et al. 2018). However, in EIDs, the total information under the signal curve is counted during the measurement interval, which makes it lack the energy distinguish ability and contain the electronic noise.

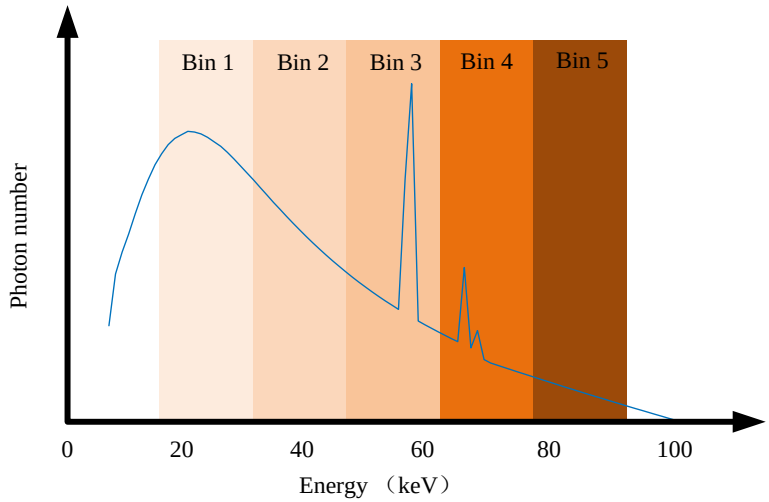

Figure 1.9 PCDs. The photons with different energies are sorted into several energy bins.

Therefore, mounted with PCDs, sCT acquires the data of more than one energy bin in just one scan. In this definition, when the number of energy bin is two, sCT actually degraded to a special kind of DECT. But due to the different implementation of DECT and the more data requirement of sCT, in this thesis, sCT refers to the CT system captured by PIDs with at least three energy bins.

- Noise in PCD.

The noise in PCD obeys Poisson distribution due to the statistic counting for the photons. What's more, cross talk and pile up are the two important effects which contribute to the detecting noise.

Cross talk. Cross talk describes the phenomenon of the photons wrongly regesitered by the detector elements into the energy bin. In the ideal PCD, the photon only generates one signal corresponding to its energy. However, in reality, the photons interact by the Compton scattering change their energies and directions, which will make them be registered with incorrect energy ranges (Bornefalk and Danielsson 2010). Another important cause of cross talk is the photons with energy near the thresholds, which are more likely to be counted by its incident energy bin and its neighbours. This way, the photons are counted more than once. The phenomenon is also called charge-sharing (Xu, Danielsson, and Bornefalk 2011). Various kinds of cross talk will bring noise in the detection, which will result in the degradation of the sCT images.

Pile-up. The number of photons striking the detectors is hundred millions per second per square millimeter (Persson et al. 2014), which requires the detectors to count the pulses fast enough. If two photons reaching to the detectors within too short time interval, it is possible to happen that the detector does not act that fast and regards them as one photon with the summed energy. In reality, the counting rate of the PCD is quite low , which makes it suffer from the noise caused by pile-up.

1.2.2 Model of sCT

As discussed above, sCT shares the similar system structure as conventional CT but mounted with PCDs. Therefore, the imaging principle also obeys the basic principle of CT model. The only difference brought by the PCD is the number of measurement in one scan. As the attenuation coefficient of the object is dependent on the energy, Beer's law is expressed as

$$I(\mathrm{E}) = I_0(\mathrm{E}) e^{-\int_L \mu(\mathrm{E}) dl}, \tag{1.6}$$

where E donates the energy of the photons. Reform the Equation (1.6) to put the measurement in one side, then it is written as

$$\int_L \mu(E) dl = -\ln \frac{I(E)}{I_0(E)}, \tag{1.7}$$

This is named as the sinogram of the scanned object under the energy E, which is usually as an observation in the CT system. Therefore, in sCT system, more than two sinograms are acquired, which for conventional CT and DECT are one and two, respectively, as displayed in Figure 1.10.

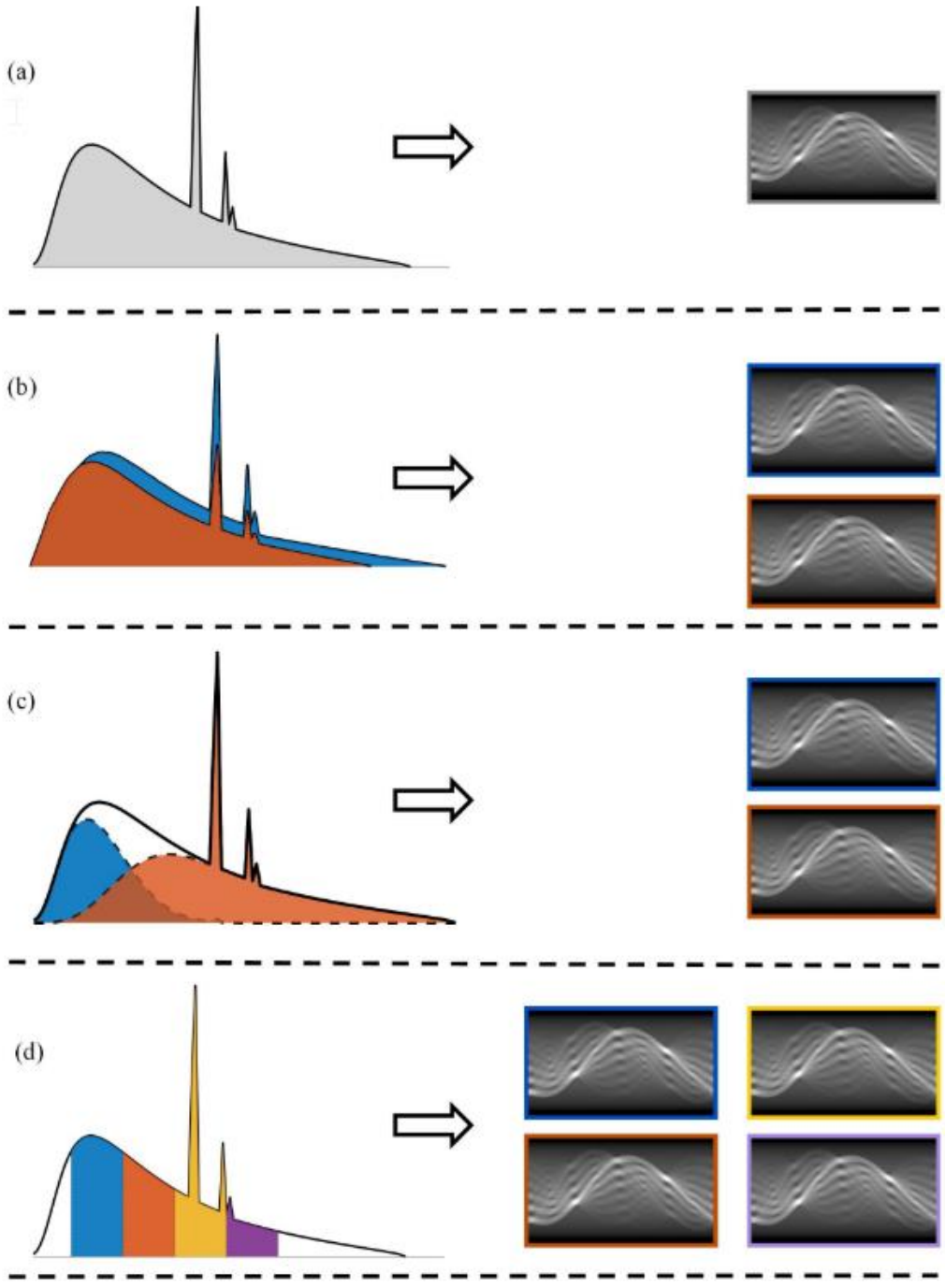

Figure 1.10 Measurement of: (a) conventional CT with one sinogram; (b) (c) DECT with two sinograms and (d) sCT with more than two sinograms (Figure from (Ting 2019)).

1.2.3 Application of sCT

1.2.3.1 Recontruction

Reconstruction is a typical topic in X-ray CT system, which illustrates the attenuation coefficient values of the object as an image. In medical analysis, the reconstructed image is usually displayed by the CT value, which is defined as

$$CT\ value = \frac{\mu - \mu_{Water}(73)}{\mu_{Water}(73)} \times 1000, \quad (1.8)$$

where $\mu_{Water}(73)$ is the attenuation coefficient of the pure water under energy of the 73 keV, and the unit for CT value is Hounsfield (HU). The CT value of pure is 0, and that of the air is -1000. Actually, CT value is a linear transform of the attenuation coefficient. Thus, the reconstruction image displayed with normalized scale in attenuation coefficient and in CT value is the same visually.

Compared to the conventional CT, sCT reconstruction acquires more than two images of the scanned object, responding to the attenuation coefficients for each energy bin. The characteristic of these images is that they share the similar structure but are of various values, which can be utilized for further analysis, such as material decomposition.

The reconstruction of sCT will be described in detail in the following Chapter 2, 4, and 5.

1.2.3.2 Material decomposition

The attenuation of the X-ray is produced by the photon-matter interaction. Thus, different materials show various attenuation curve for the X-ray. In 1976, Alvarez and Macovski (Alvarez and MacOvski 1976b) proposed to extract energy-dependent information by dividing the attenuation coefficients into photoelectric absorption and Compton effect, each corresponding to the composition information and mass density information of the object.

Figure 1.11 shows the mass attenuation curve for five materials from 0 to 150 keV, including PMMA, Water, gadolinium (Gd), iodine (I) and iron (Fe) . As can be observed, the attenuation coefficient generally decrease with the increase of the energy (such as Water and PMMA), but it has various sudden increase for different materials (such as Gd and I), which is the characteristic of the material attenuation coefficient, namely the K-edge effect. For Gd, the K-edge energy is about 50 keV, and for I is about 33 keV. Thus, the materials with K-edge effect are often injected to humans for diagnosis assistance. Roessl and Proksa (Roessl and Proksa 2007) added the K-edge term into the decomposition formula and successfully distinguish the Gd from the normal tissues.

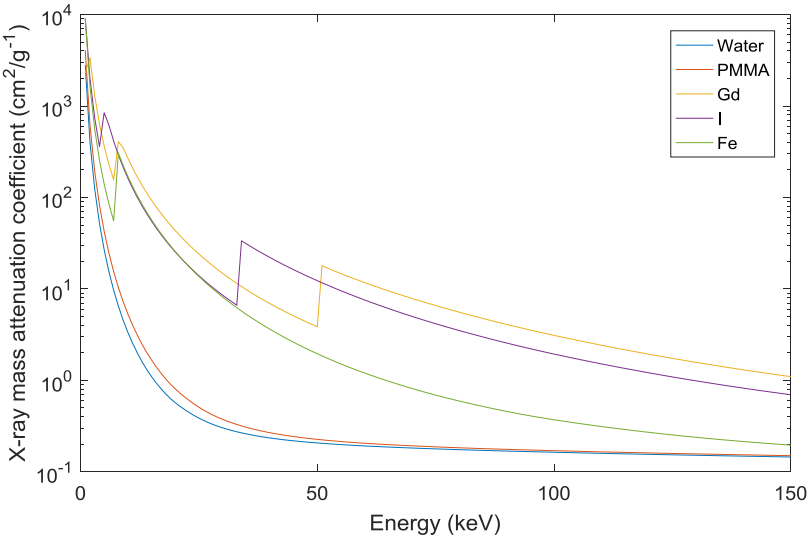

Figure 1.11 Mass attenuation coefficients for five different materials from 0 to 150 keV, including PMMA, Water, Gd, I and Fe.

The material decomposition opens the door for viewing the nature cause of the attenuation for X-ray. Material decomposition in X-ray CT not only gives the variety of the material but also calculates the corresponding concentration, which has multiple applications in medical diagnosis and industry detection. Figure 1.12 shows an example of material decomposition results, which enables to illustrated the material distribution within the human heart.

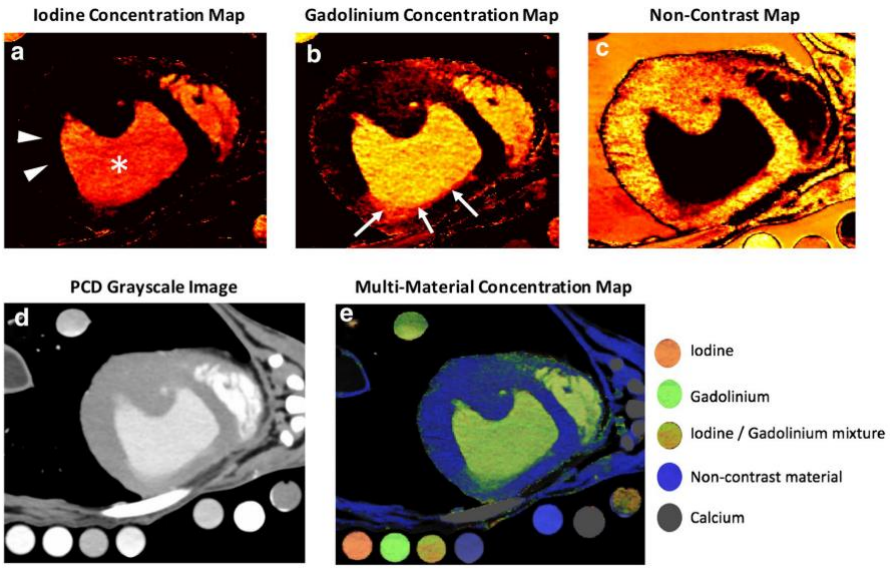

Figure 1.12 Material decomposition in sCT (Cited: (Symons et al. 2017)).

1.2.3.3 Image enhancement

The information within appointed range of energy is the key for practical application. For example, in medical diagnosis, the contrast agent injected to the human can help to observe the organ metabolism. However, a narrow energy bin often is often sensitive to the noise and has low signal-to-noise ratio(SNR). By combing the information of this

energy bin with the rest of the energy bins abtained in sCT, one image with both high contrast-to-noise ratio (CNR) and SNR could be acquired (Bouleti et al. 2017).

Another image enhancement is through the generation of virtual monoenergetic (monoE) image. Due to the sudden increase in the attenuation coefficient of the contrast agent with K-edge effect, the attenuation coefficient near the K-edge energy is often with larger value, which is thus utilized for enhancement while reducing the nearby streak and beam hardening artifacts (Patel et al. 2019). Figure 1.13 gives an application of the enhancement through MonoE on the lumen of the aorta.

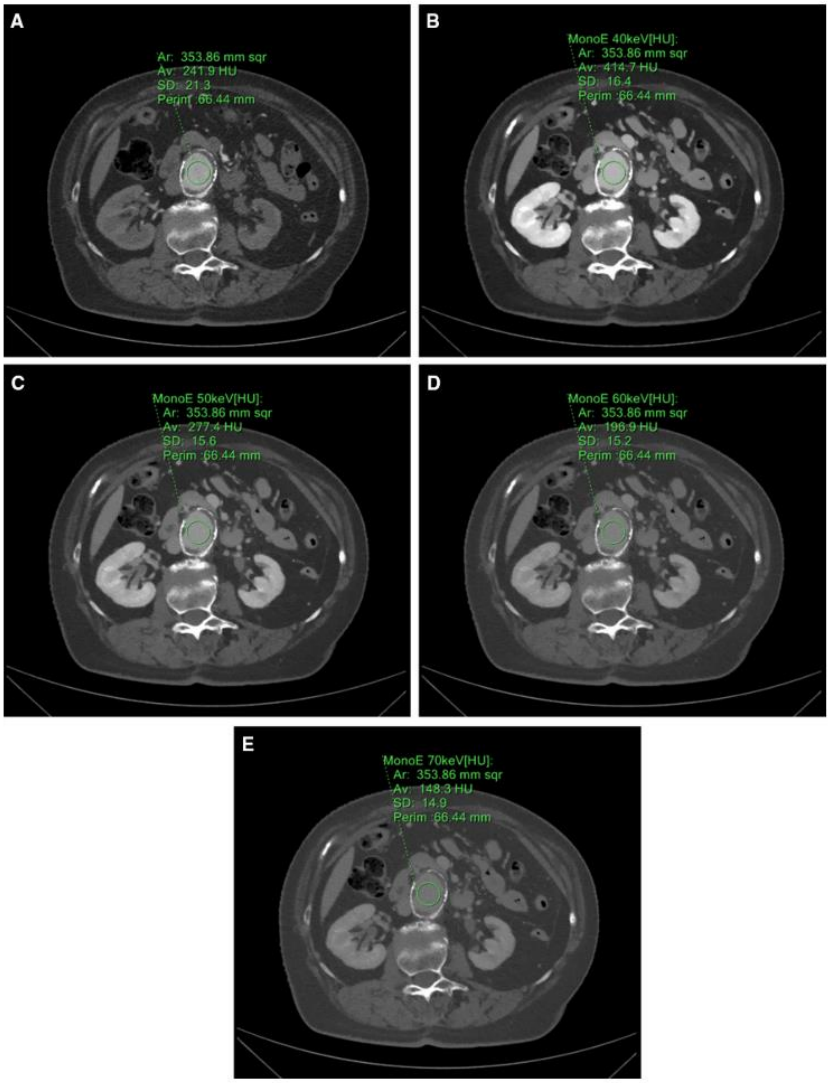

Figure 1.13 Enhancement through MonoE: (A) Identical circular ROI drawn on true arterial; (B) Virtual monoE at 40 keV, and 50 keV (C), 60 keV (D), 70 keV (E) (Patel et al. 2019).

1.3 Summary

To summarize, in this chapter, as the fundamental of all the CT system, we first introduced the basic principles of X-ray CT. Then the development of CT system is presented and the difference between conventional CT and sCT are described in detail, which is mainly thanks to the PCDs. Due to the distinguish ability of PCDs, sCT shows

potential application in image reconstruction, material decomposition and image enhancement.

Chapter 2 Reconstruction of sCT images

Abstract

In this chapter, we introduce the general reconstruction method of sCT images. As a special form of CT system, sCT can be regarded as several acquisitions of the conventional CT. Thus, all the traditional methods can be utilized for reconstruction in sCT. The reconstruction algorithm is divided into three kinds: analytical methods, iterative methods and learning methods. Each kind of method has their own characteristics: analytical methods are quick but sensitive to the noise; iterative methods show better performances under the noisy conditions but require more time and space to calculate; learning methods show good potential in reconstruction but require large data set, which is the rare resource in sCT. Therefore, despite the better performances of iterative methods and learning methods, analytical methods is still the most widely utilized in industry. In the future, the overcome of the shortcomings in iterative methods and learning methods will provide more possibilities for sCT reconstruction.

2.1Introduction

A lot of researches have been made on the CT reconstruction since its introduction. As a kind of CT system, sCT images can also be reconstructed by utilizing the conventional reconstruction methods. Meanwhile, due to the characteristic of sCT, there also developed many specific methods for sCT reconstruction. In the past years, CT reconstruction has developed from the traditional analytical method to iterative methods and nowadays to learning methods. The analytical method reconstructs the image from the formulation of the projection by inverse transform; the iterative methods reconstructs the image by creating a model combining the reconstructed errors and priori knowledge. Nowadays, due to the nonlinear modeling ability of learning method, learning methods have already been extended to the reconstruction of CT images on the basis of big data.

2.2 Analytical methods

In X-ray CT, the source generates energy spectrum under the given source voltage, current and scanning time, which corresponds to a specific photon number distribution. When the photons get through the phantom, due to the photon-mater interaction, considering the position of the scanned object, the photons reaching the detectors will decrease both in number and energy and obey the Beer's law (M 2008)

$$I(E)=I_0(E)\exp\left(-\int_L f(x,y,E)dl\right), \qquad (2.1)$$

where $I_0(E)$ designate the photon numbers generated by the source, $I(E)$ the photon numbers received by the detectors, $\mu(x,y,E)$ the attenuation coefficient of energy E at position (x,y), and $\int_L f(x,y,E)dl$ the penetrating line integral of the attenuation coefficient along the line L for X-ray from source to detector. In X-ray CT, $I_0(E)$ and $I(E)$ are the measurements. Thus, the line integration of the $f(x,y,E)$ is expressed as

$$\int_L f(x,y,E)dl=-\ln\frac{I(E)}{I_0(E)}, \qquad (2.2)$$

which is also called projection data. As shown in Figure 2.1, this projection is denoted by the parameters θ and the integration length s in the rotating sampling system (ξ,η), namely

$$P_\vartheta(\xi,E)=\int_{(\theta,s)} f(x,y,E)d\eta=-\ln\frac{I(E)}{I_0(E)}, \qquad (2.3)$$

Equation (2.3) represents the projection data in the rotating sampling system under the given projection angle θ and the position of the collecting time. However, due to the constantly changing of the system in the data collection, it is compliable to describe the attenuation values in the system. Thus, the fixed coordinate system is utilized to express the image of the spatial distribution of attenuation coefficients. The two coordinate systems are transformed by

$$\begin{bmatrix}\xi\\ \eta\end{bmatrix}=\begin{bmatrix}\cos\theta & \sin\theta\\ -\sin\theta & \cos\theta\end{bmatrix}\begin{bmatrix}x\\ y\end{bmatrix}, \tag{2.4}$$

namely

$$\xi = x\cos\theta + y\sin\theta\ , \tag{2.5}$$

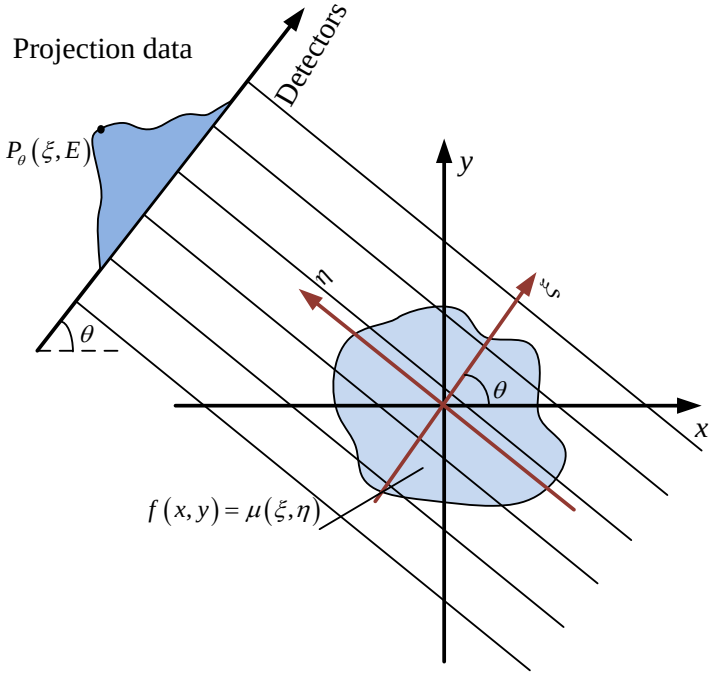

Figure 2.1 Coordinate for 2D Parallel projections (Figure collected from (Gullberg et al. 2009).

From the view point of signal processing, the stepwise shift of the X-ray source represents a sampling process of the continuous projection signal. Thus, the projection data is rewritten as

$$P_\theta(\xi,E)=\int_{-\infty}^{+\infty}\int_{-\infty}^{+\infty} f(x,y,E)\,\delta(x\cos\theta+y\sin\theta-\xi)\,dxdy=\int_0^s \mu(\xi,\eta,E)d\eta\ , \tag{2.6}$$

where $\delta(\bullet)$ is the Dirac function. In this way, all points of the objects lying on the line $\xi = x\cos\theta + y\sin\theta$ are passed through by X-ray photons. Actually, the projection data $P_\theta(\xi,E)$ is equal to the Radon transform of function $f(x,y,E)$, which is the projection of $f(x,y,E)$ along the line in the angle θ and ξ distance from the origin of the coordinate.

- ***Fourier slice theorem***

The Fourier slice theorem, also known as center slice theorem, is the foundation in the analytical CT reconstruction methods. It says that the 1D Fourier transform of $P_\theta(\xi, E)$ equals to the 2D Fourier transform of $f(x,y)$ at angle θ, as shown in Figure 2.2. In this method, for each energy bin, the reconstruction is independent and the influence of energy is ignored within the energy bin. Thus, in the following of this part, the energy dependent variable will be omitted since it does not contribute to the reconstruction method.

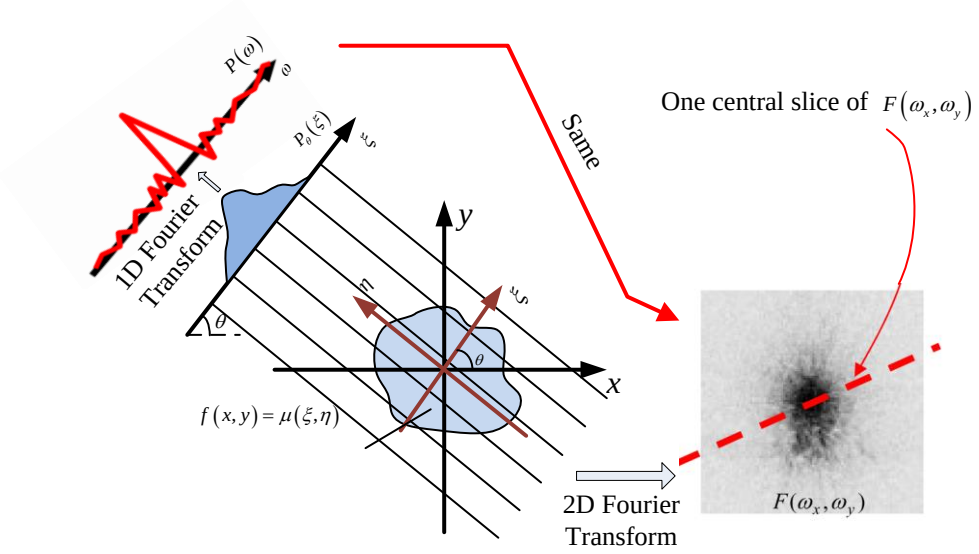

Figure 2.2 Fourier slice theorem.

Thus, if the object is scanned at least 180°, the 2D Fourier transform of the object corresponding to the central slices of the detector directions will cover all the Fourier space, namely $\omega_x - \omega_y$ space. In other words, if scanning the system around the object for 180° rotation, the complete Fourier transform function $F(\omega_x, \omega_y)$ can be acquired, as shown in Figure 2.3. Thus, the reconstructed image $f(x,y)$ is determined by inverse 2D Fourier transform.

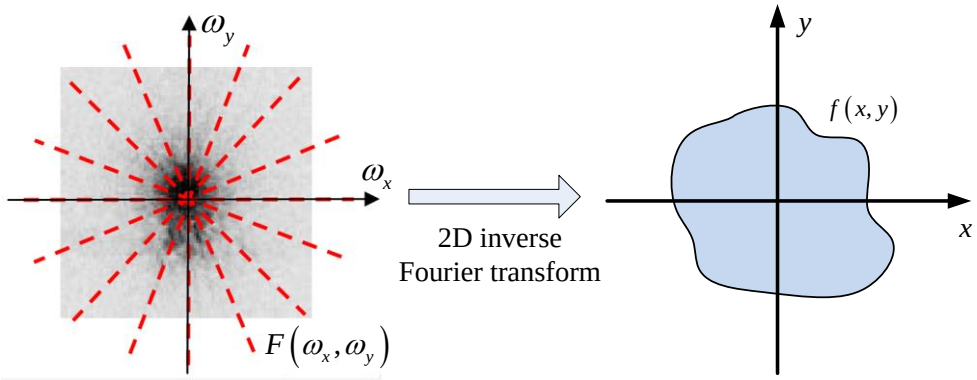

Figure 2.3 Detector brings a central slice in Fourier space. When these lines covered all the Fourier space, the original image can be reconstructed by inverse Fourier transform.

- ***Filtered Back projection***

Fourier slice theorem is the basis of FBP algorithm. In the (ξ,η) coordinate system, a Fourier transform is made on the projection data, namely

$$S_\theta(\omega)=\int_{-\infty}^{+\infty}P_\theta(\xi)e^{-j2\pi\omega\xi}d\xi=\int_{-\infty}^{+\infty}\left[\int_{-\infty}^{+\infty}\mu(\xi,\eta)d\eta\right]e^{-j2\pi\omega\xi}d\xi \quad (2.7)$$

According to Equation (2.3), it is rewritten as

$$S_\theta(\omega)=\int_{-\infty}^{+\infty}\int_{-\infty}^{+\infty}f(x,y)e^{-j2\pi\omega(x\cos\theta+y\sin\theta)}dxdy \quad (2.8)$$

Let $u=x\cos\theta, v=y\sin\theta$, the equation is written as the 2D Fourier transform at spatial frequency

$$S_\theta(\omega)=F(\omega\cos\theta,\omega\sin\theta)=F(u,v) \quad (2.9)$$

Make 2D inverse transform of $F(u,v)$, then the original image $f(x,y)$ can be reconstructed, as shown in Equation (2.10)

$$f(x,y)=\int_{-\infty}^{+\infty}\int_{-\infty}^{+\infty}F(u,v)e^{j2\pi(ux+vy)}dudv \quad (2.10)$$

Transform coordinates (u,v) in frequency domain to polar coordinate system (ω,θ) , Equation (2.10) is rewritten as

$$\begin{aligned}
f(x,y)&=\int_0^{2\pi}\int_{-\infty}^{+\infty}F(\omega,\theta)e^{j2\pi\omega(x\cos\theta+y\sin\theta)}\omega d\omega d\theta\\
&=\int_0^{\pi}\int_{-\infty}^{+\infty}F(\omega,\theta)e^{j2\pi\omega(x\cos\theta+y\sin\theta)}\omega d\omega d\theta+\int_0^{\pi}\int_{-\infty}^{+\infty}F(\omega,\theta+\pi)e^{j2\pi\omega(x\cos(\theta+\pi)+y\sin(\theta+\pi))}\omega d\omega d\theta\\
&=\int_0^{\pi}\left[\int_{-\infty}^{+\infty}F(\omega,\theta)|\omega|e^{j2\pi\omega(x\cos\theta+y\sin\theta)}d\omega\right]d\theta\\
&=\int_0^{\pi}\left[\int_{-\infty}^{+\infty}S_\theta(\omega)|\omega|e^{j2\pi\xi\omega}d\omega\right]d\theta\\
&=\int_0^{\pi}h_\theta(\xi)d\theta
\end{aligned} \quad (2.11)$$

where

$$h_\theta(\xi)=\int_{-\infty}^{+\infty}S_\theta(\omega)|\omega|e^{j2\pi\xi\omega}d\omega \quad (2.12)$$

From Equation (2.12), it is observed that the original image $f(x,y)$ is actually the inverse Fourier transform of $S_\theta(\omega)|\omega|$. $h_\theta(\xi)$ is also called the filtered projection, which is actually the high-pass filtered projection signal $P_\theta(\xi)$. This can also be explained from the Fourier slice theorem that the frequency spectrum has a higher density distribution near origin point than other regions. Therefore it is necessary to introduce a correction filter to reduce the over weighted effects at low frequency. Meanwhile, since the projection data is sampled, the filter only need to match the sampling points of w. Due to the fact that in reality the energy of high frequency is so low to be negligible, the filter is selected to be bandlimited. According to the Shannon Theory, the sampling interval is set as $\tau=1/2W$ if the W is the maximum frequency. Considering all the above conditions, the bandlimited filter is

$$H(w) = |w| b_{\omega}(\omega), \tag{2.13}$$

where

$$b_{\omega}(\omega) = \begin{cases} 1 & |\omega| \le W \\ 0 & otherwise \end{cases}, \tag{2.14}$$

Thus, the filtered back projection (FBP) principle is defined. It is concluded by the three steps.

Algorithm 2.1 FBP

1. Calculation of the Fourier transform of $P_\theta(\xi)$

$$P_\theta(\xi) \circ ------ \bullet S_\theta(\omega)$$

2. Back transform of the bandlimited filtered $S_\theta(\omega)$

$$S_\theta(\omega) H(\omega) \bullet ------ \circ h_\theta(\xi)$$

3. Backprojection on the line $\xi = x\cos\theta + y\sin\theta$

$$f(x,y) = \int_0^\pi h_\theta(\xi) d\theta$$

The relationship of the image (object space), the projection (Radon space), and frequency space (Fourier space) is summarized as the following figure.

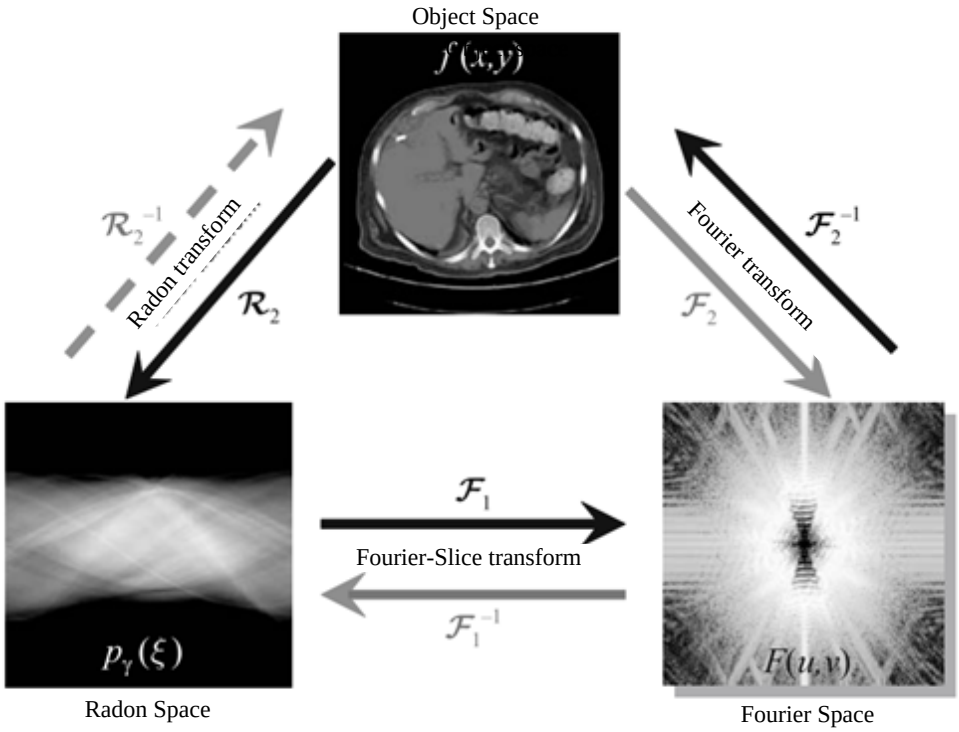

Figure 2.4 The transform between among Object Space, Radon Space and Fourier Space (M 2008).

2.3 Iterative methods

FBP is the most widely used algorithm in industry because of its fast speed. FBP weights all the X-rays equally, which however does not consider the beam-hardening artifacts resulted from the polychromatic spectrum of the source tube. The beam-

hardening artifacts are especially obvious when the scanning objects contain metal material. Thus, algebraic and statistic method provide other possibilities to reconstruct the CT images, which are usually solved by iterative algorithm.

2.3.1 Algebraic reconstruction techniques (ART)

Since the invention of X-ray CT, the first reconstructions were made by the ART. Although FBP is the most widely applied algorithm today, ART still has significant influence for its performance in noisy conditions.

ART regards the reconstruction problem as a linear system of equations and considers the discrete measurement of the practical realization of the CT system. The projections $P_\theta(\xi)$ are actually discrete due to the distribution of the detector array. The CT image to be reconstructed is usually reshaped as a discrete vector of unknown variables f_j, $j=1,...,N$. The set of projections is described by a linear system of equations. When the X-rays pass by the object, the intensity of the X-ray beam will be weakened due to the Compton effect, photoelectric effect and k-edge effect, which is quantified by attenuation coefficients, namely $\mu_j = f_j$. For each ray through the object, the sum of the attenuation coefficients is obtained by the measurement and Beer's law. As each X-ray does not penetrate all the pixels of the object, we must evaluate the degree of the X-ray functioning with each pixel. In the ART method, the assumption is that the X-ray has a certain width. To determine the weights of the X-ray passing through pixel, the ratio of the beam illuminating the area and the entire pixel area is utilized, as shown in Figure 2.5 and defined by Equation (2.15)

$$a_{ij} = \frac{S_{ij}}{b^2}, \qquad (2.15)$$

where a_{ij} donates the contribution of ray i to pixel j, S_{ij} represents the illuminated area of pixel j by ray i, and b^2 is the total area of pixel j.

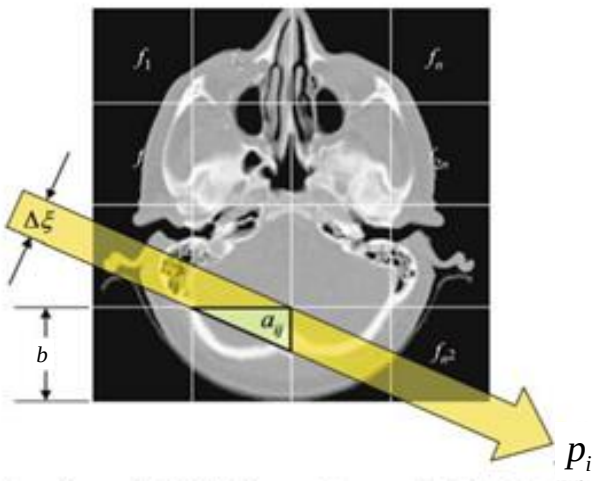

Figure 2.5 The weight of the system matrix in ART algorithm for a X-ray beam (M 2008).

Therefore, a set of equations is expressed as

$$\sum_{j=1}^{N} a_{ij}\mu_j = p_i \quad , \tag{2.16}$$

where N is the number of pixels that are to be reconstructed (if the image size is $n \times n$, then $N = n^2$), $i = \{1,2,...,M\}$ is the index of the projection. M is acquired by the total number of projections D and the number of detectors N_p, namely $M = N_p D$. Writing all the projections and all the attenuation coefficients as column vectors, we get

$$\mathrm{p} = \left(p_1, p_2, ..., p_M\right)^T , \tag{2.17}$$

$$\mu = \left(\mu_1, \mu_2, ..., \mu_N\right)^T , \tag{2.18}$$

The weightings are also writing by an $M \times N$ matrix, namely

$$A = \begin{pmatrix} a_{11} & a_{12} & \cdots & a_{1N} \\ a_{21} & \cdot & & a_{2N} \\ \vdots & & \cdot & \vdots \\ a_{M1} & & & a_{MN} \end{pmatrix} , \tag{2.19}$$

where A is also called the system matrix, which is determined by the system geometry and scanning way. Therefore, the system of equations is

$$\mathrm{p} = A\mu , \tag{2.20}$$

In reality, as each pixel is small and the size of system matrix is huge, A is usually replace by a sparse matrix whose elements above the threshold are set as 1 and those below as 0.

The above equation models a single energy bin. For sCT with K energy bins, the equation is expressed as

$$Y = AU , \tag{2.21}$$

where $Y = \left[\mathrm{p}_1, \mathrm{p}_2, ..., \mathrm{p}_K\right]$ is the measurement for all the energy bins, and $U = \left[\mu_1, \mu_2, ..., \mu_K\right]$ for the reconstruction for all the energy bins. Of course, each energy bin is treated as an independent measurement and built the reconstruction separately.

In practice, the solution of the equations cannot be easily obtained because the problem is ill-conditioned. Very small singular values might occur and very small errors in the measurement will result in the large fluctuations in the reconstructed images. Thus, in ART method, this inverse problem is solved by iterative algorithm. For one energy bin reconstruction, this method begins with an initial image assumption μ^0 , and compare the calculated values in the process until reaching the convergences conditions (the maximum iteration number or the threshold of the errors).

As the starting point, μ^0 can be arbitrary, from the results of other rudimentary estimation such as FBP, or set as a zero vector, which does not have much influence on the final reconstruction. The principle of the ART method can be explained by an 2D example. The vector μ^0 is projected perpendicularly onto the first straight line that represents the first X-ray beam with the projection result p_1 to get an improvement

image μ^1. Then μ^1 is also projected perpendicularly onto the second straight line p_2 in the same way and acquire the image μ^2. μ^2 has some improvement compared with μ^1 because it locates closer to the intersection point of the straight line than its two predecessors. Thus, the iteration equation is expressed as

$$\mu^k = \mu^{k-1} - \frac{\left(a_i \mu^k - p_i\right)}{a_i \left(a_i\right)^T} \left(a_i\right)^T, \qquad (2.22)$$

where $a_i = (a_{i1}, a_{i2}, ..., a_{iN})$ is the row i of the system matrix A.

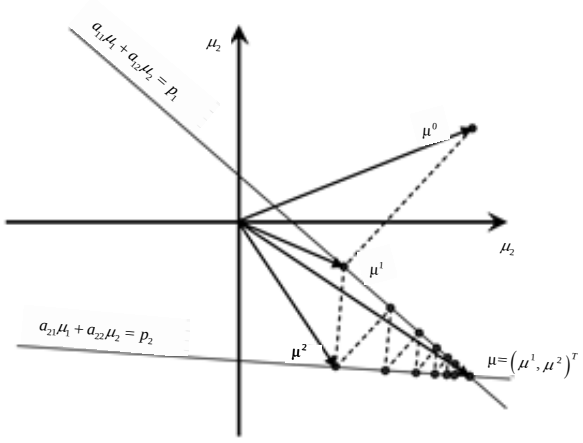

Figure 2.6 The principle of ART method in 2D plane.

Therefore, ART is summarized by the following 4 steps:

Algorithm 2.2 ART

Input: A, $Y = [p_1, p_2, ..., p_K]$, $p = (p_1, p_2, ..., p_M)^T$

Output: $U = [\mu_1, \mu_2, ..., \mu_K]$

Initialize: set k=1, μ^0

For each energy bin, do

(1) Calculate the forward projection based on the k th estimation

$$p_k = A\mu^k$$

(2) Correct reconstruction image by back-projection and obtain $\mu^{(k)}$

$$\mu^k = \mu^{k-1} - \frac{\left(a_i \mu^k - p_i\right)}{a_i \left(a_i\right)^T} \left(a_i\right)^T$$

(3) If the stop criterion is satisfied, the algorithm ended; otherwise set $k = k+1$ and return to step (2).

2.3.2 Regularization models

ART takes advantage over the FBP method in reducing the noise, especially in sparse and incomplete data. The essence of the ART algorithm is to build the reconstruction as a system of equations and explores the iterative method to solve this

model. Inspired by this idea, it developed many methods which incorporate the prior information to improve the performances.

The improved model usually creates an objective function which consists by two parts: the data fidelity term to measure the reconstruction errors and the regularizations term to indicate the prior knowledge. The aim of the method is to minimize the sum of the data fidelity term and the regularization term, namely the objective function, which is represented as

$$U^* = \arg\min_U \left\{ \mathcal{F}(U) + \lambda \mathcal{R}(U) \right\}, \tag{2.23}$$

where $\mathcal{F}: \mathbb{R}^N \to \mathbb{R}^M$ is the data fidelity term which is usually defined as Equation (2.24)

$$\mathcal{F}(U) = \frac{1}{2} \| Y - AU \|_2^2, \tag{2.24}$$

and $\mathcal{R}: \mathbb{R}^N \to \mathbb{R}^M$ defines the regularization penalty with $\lambda > 0$ being the regularization parameter balancing the trade-off between the two terms. The regularization term does not necessarily has only one part, which means it can include all the prior information by multiple parts. The following paragraphs will introduce three most commonly existing regularization forms in detail, including the TV, TNV and PRISM, and the most widely used method split Bregman algorithm to solve the models with regularizations.

2.3.2.1 Regularization terms

A. Total Variation (TV)

The total variation (TV) penalty has been successful as the most widely utilized regularization due to its edge-preserving qualities. The isotropic TV defined for a single energy bin image is denoted by Equation (2.25)

$$\mathrm{TV}(\mu) = \sum_{j=1}^{N} \left\| D_j \mu \right\|_2, \tag{2.25}$$

where D_j is a $2 \times N$ matrix such that $D_j \mu$ is the gradient of μ at pixel j. Thus, for sCT, this term is defined as the sum of the TV norm of each energy bin, namely

$$\mathcal{R}_{\mathrm{TV}}(U) = \sum_{k=1}^{K} \mathrm{TV}(\mu_k), \tag{2.26}$$

The TV regularization could improve the reconstruction quality by smoothing the pixels of the images. However, it does not employ the data of the energy bin with high SNR to improve the reconstruction of the energy bin that is disturbed by larger noise.

B. Total nuclear variation (TNV)

The total nuclear variation (TNV) was proposed to enforce the strong relationship among energy bins. TNV employs the nuclear norm of the Jacobian matrix of all the energy bins, and penalizes the singular values of the Jacobian (Kazantsev et al. 2018). Based on the Schatten matrix norm of the first order, TNV penalty is expressed as

$$\mathcal{R}_{\mathrm{TNV}}(U)=\sum_{j=1}^{N}\left\|D_jU\right\|_*, \tag{2.27}$$

where $\|\cdot\|_*$ is the nuclear norm, i.e. the sum of the singular values. TNV is proved to perform well in medical sCT application with five energy bins.

C. A prior rank, intensity and sparsity model (PRISM)

This method (Manley 2013) is developed to reconstruct the multi-energy images with fewer CT data and less radiation dose. Motivated by the knowledge that the multi-energy images of each energy bin shares the same background over energy and the spectral features of these images are sparse, PRISM decomposes the multi-energy images into the sum of a low-rank matrix U_L and a sparse matrix U_S, namely

$$U=U_L+U_S, \tag{2.28}$$

For the low-rank part, PRISM employs the rank of the tight-frame transform of the multi-energy images to describe the coherence of the energy spectrum; for the sparse part, it merges the characteristics the base materials into the model. Thus, the regularization of PRISM is expressed as

$$\mathcal{R}_{\mathrm{PRISM}}(U_L,U_S)=\lambda_*\|U_L\|_*+\lambda_1\|WU_S\|_1+\lambda_t\|WU\|_1, \tag{2.29}$$

where W represents the tight-frame transform, $\lambda_*, \lambda_1, \lambda_t$ are the parameters to balance the trade-off of each item.

2.3.2.2 Optimization

There are many optimization algorithms for solving the problems, such as conjugate gradient algorithm (CG), fast composite splitting algorithm (FCSA), maximum likelihood expectation maximization (MLEM), ordered subsets expectation maximization (OSEM), alternating direction method of multipliers (ADMM), split Bregman algorithm (SBA), and so on. CG utilizes the gradient of the objective function and finds the solution through large number of iterations, which is of low efficient. Based on the wavelet sparsity, FCSA has higher calculation efficiency compared with CG but often suffers from the cascade effect. MLEM and OSEM (a modified version of MLEM to accelerate the convergence speed) are methods based on the statistical feature of the data and have already been wildly utilized in medical imaging (especially in emission tomography) due to their ability in denoising, but it is sensitive to data and may increase the errors with the iteration number (Ch et al. 2015; Chun et al. 2016; Li 2016). ADMM and SBA are the effective methods for solving the problems with L1 norm. As a special form of ADMM, SBA converges faster than ADMM when the parameters are properly selected (Nien and Fessler 2014). Therefore, considering the computational efficacy and numerical stability, SBA is adopted to solve this problem.

This method searches the solution by alternatively optimizing the variables. For the Equation (2.23), if $\mathcal{F}(U)$ and $\mathcal{R}(U)$ are convex functions and $\mathcal{R}(U)$ is differentiable, this problem is transferred to

$$\arg\min_{U,\mathrm{d}}\left\{\|\mathrm{d}\|_1+\lambda\mathcal{R}(U)\right\}\qquad \textit{subject to}\ \mathrm{d}=\mathcal{F}(U), \tag{2.30}$$

This constrained problem is transformed to the unconstrained problem as Equation (2.31)

$$\arg\min_{U,\mathrm{d}}\left\{\|\mathrm{d}\|_1+\lambda\mathcal{R}(U)+\frac{1}{2\delta}\|\mathrm{d}-\mathcal{F}(U)\|_2^2\right\}, \tag{2.31}$$

where δ is a super parameter, which will only affect the convergence speed. Hence, according the Bregman iteration, the equation is expressed as

$$\left[U^{k+1},\mathrm{d}^{k+1}\right]=\arg\min_{U,\mathrm{d}}\left\{\|\mathrm{d}\|_1+\lambda\mathcal{R}(U)+\frac{1}{2\delta}\|\mathrm{d}-\mathcal{F}(U)-\mathrm{b}^k\|_2^2\right\}, \tag{2.32}$$

$$\mathrm{b}^{k+1}=\mathrm{b}^k+\mathcal{F}(U)-\mathrm{d}^{k+1}, \tag{2.33}$$

Thus, the regularization optimization problem has changed to a series of unconstrained optimization problems and Bregman iterations. This method is simpler than the traditional formula to calculate the optimization solution. After separating the L1 and L2 components of the function, the next procedure will be to solve Equation (2.32), which is implemented by the following two steps:

$$U^{k+1}=\arg\min_{U,\mathrm{d}}\left\{\lambda\mathcal{R}(U)+\frac{1}{2\delta}\|\mathrm{d}-\mathcal{F}(U)-\mathrm{b}^k\|_2^2\right\}, \tag{2.34}$$

$$\mathrm{d}^{k+1}=\arg\min_{U,\mathrm{d}}\left\{\|\mathrm{d}\|_1+\frac{1}{2\delta}\|\mathrm{d}-\mathcal{F}(U)-\mathrm{b}^k\|_2^2\right\}, \tag{2.35}$$

Therefore, the steps of the split Bregman algorithm to optimize the regularization problem is summarized as following:

Algorithm 2.3 Split Bregman algorithm

Output: U

Initialize: set k=0, δ, U^0

While $\|\mu^k-\mu^{k-1}\|_2\geq tol$

For $k=1$ to K

$$U^{k+1}=\arg\min_{U,\mathrm{d}}\left\{\lambda\mathcal{R}(U)+\frac{1}{2\delta}\|\mathrm{d}-\mathcal{F}(U)-\mathrm{b}^k\|_2^2\right\}$$

$$\mathrm{d}^{k+1}=\arg\min_{U,\mathrm{d}}\left\{\|\mathrm{d}\|_1+\frac{1}{2\delta}\|\mathrm{d}-\mathcal{F}(U)-\mathrm{b}^k\|_2^2\right\}$$

end

$\mathrm{b}^{k+1}=\mathrm{b}^k+\mathcal{F}(U)-\mathrm{d}^{k+1}$

end

SBA are also available for solving the objective function with more than two regularization terms (including L1 and L2 terms) by decomposing it into several sub problem and optimizing it alternatively. For each sub problem, various optimizations can be adopted to find the solution.

2.4 Learning methods

Over the past years, machine learning, or artificial intelligence, has generated preponderant researches and attracted much attention in many aspects, including medical image processing. The most widely applied method is dictionary learning (DL) (Chen et al. 2014), which expresses the image by a sparse linear combination of the learned atoms. In the compressed sensing theory, DL and sparse representation has close relationship to each other. The patch-wise DL makes it more effective to represent the image with patch-shaped features. The following part will describe the principle of DL in CT reconstruction.

DL is based on the image domain, which means a primary reconstructed image should be acquired in the first step. Usually, the primary image suffers from severe noise and artifacts. Let $\tilde{\mu}$ denote the primary image, the DL based patch-wise model is expressed as

$$\arg\min_{U,\mathrm{D},\alpha} \lambda \left\| U-\tilde{U} \right\|_2^2 + \sum_{ij} \varsigma_{ij} \left\| \alpha_{ij} \right\|_0 + \sum_{ij} \left\| R_{ij}U - D\alpha_{ij} \right\|_2^2 , \qquad (2.36)$$

where R_{ij} represents the operator to extract the patch with size $\sqrt{m}\times\sqrt{m}$ centered at the position (i,j) in the after reshape the U as images, D donates the dictionary matrix of size $m\times K$, which consists of K m-vector atoms, and α_{ij} represents the coefficient of the dictionary for the patch centered at the position (i,j). This problem is usually solved by two steps:

$$\arg\min_{\mathrm{D},\alpha} \left\| \alpha_{ij} \right\|_0 \quad s.t. \left\| R_{ij}U - D\alpha_{ij} \right\|_2^2 \le \varepsilon, \left\| \alpha_{ij} \right\|_0 \le L \ \forall i,j , \qquad (2.37)$$

$$\arg\min_{U} \lambda \left\| U-\tilde{U} \right\|_2^2 + \sum_{ij} \left\| R_{ij}U - D\alpha_{ij} \right\|_2^2 , \qquad (2.38)$$

where ε and L are the tolerance parameters. Equation (2.37) is to train the coefficient α_{ij} and dictionary D by the patches and is usually solved by the K-means Singular Value Decomposition (K-SVD) (Chen et al. 2014). With fixed coefficient and dictionary, Equation (2.38) can be solved by iterative methods.

DL methods employ the characteristics of the image itself and improve the reconstruction quality, which makes it successfully applied in medical imaging. Later, many researches are developed based on the DL approaches, including tensor-based DL reconstruction (Tan et al. 2015; Zhang et al. 2017). Nowadays, DL based methods has become a significant part in CT reconstruction as a machine learning tool.

Deep learning methods have attracted much attention over the past years as its effective performance, also including medical imaging (Greenspan, Van Ginneken, and Summers 2016). However, the good performance is based on the large data set, which makes it a limit application to the sCT reconstruction.

2.5 Summary

Based on the Radon Transform, Fourier slice theorem, the analytical methods can fast acquire the reconstructed image but ares sensitive to the noise; iterative method

utilize the prior knowledge as the constraints of the objective function to improve the quality of the reconstruction but require long time cost; recently deep learning methods show good potential in reconstruction, but require large amount of data which is the rare resource for sCT. The development of reconstruction in CT is presented as Figure 2.7. FBP is still the most widely used method in practical applications; iterative algorithms are researched popularly in the low-dose CT, DECT and sCT at present; some deep learning methods has been developed for conventional CT; in the future, with the increase of the dataset, deep learning methods combine both the analytic method and iterative method show potential ability to acquire better performances in CT imaging.

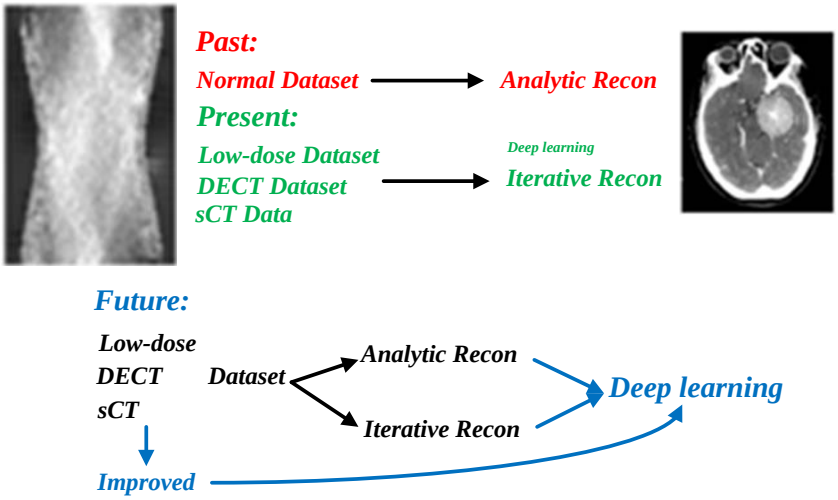

Figure 2.7 The development of CT reconstruction (Figure inspired by (Wang 2016)).

Chapter 3 Multimodel imaging of sCT

Abstract

This chapter proposes to investigate the potentialities of sCT to perform simultaneously multimodal imaging through a simulation study. The idea consists in using sCT to achieve both conventional anatomical CT (aCT) imaging and new functional CT (fCT) imaging. To this end, a virtual sCT system and a phantom containing different materials of various densities were designed. Then, multi-energy data at different energy bins of the phantom were acquired using the virtual sCT system. After that, aCT function of sCT was studied using the same configuration as that of conventional CT, and, at the same time, fCT function of sCT was investigated by applying material decomposition algorithms to the same acquired multi-energy data. Finally, the simulations were validated on physical sCT data. The results showed that sCT can be used to achieve simultaneously aCT and fCT imaging in one single acquisition. It produces substantially better image quality while requiring much lower dose than conventional CT. Moreover, sCT offers the possibility to enhance intrinsically anatomical images by making use of multi-energy data. Meanwhile, when used as fCT, sCT enables us to get insights into the quantitative composition of materials in a pixel, by detecting and quantifying for example mixtures of water, Gd, I and Fe of different concentrations. Par ailleurs, lorsqu'elle est utilisée comme fCT, la sCT nous permet d'obtenir des informations sur la composition quantitative de matériaux dans un pixel, en détectant et en quantifiant par exemple des mélanges d'eau, Gd, I et Fe de différentes concentrations.

3.1 Introduction

Due to its higher energy resolution, sCT can be used to not only image the anatomical characteristics of an object but also obtain the quantitative composition of materials that constitute the object. In this sense, sCT offers the possibility to realize simultaneously anatomical CT (aCT) and functional CT (fCT), which is very attractive for many applications. Figure 3.1 illustrates well an example of such simultaneous multimodal imaging ability of sCT. The phantom contains four materials of polymethyl methacrylate (PMMA), water, gadolinium (Gd) and iodine (I), which have different densities. We can readily reconstruct conventional aCT image by making use of the total energy from the five energy bins (30-39keV, 40-49keV, 50-59keV, 60-69keV, 70-79keV). At the same time, we can also obtain fCT images by using an appropriate material decomposition algorithm, each of which corresponds to one of the four materials constituting the object.

For sCT, a number of reconstruction and material decomposition methods were reported in the literature. Concerning sCT reconstruction, three categories of methods can be loosely identified: traditional analytical filtered backprojection (FBP) method (Buzug 2015), iterative methods (Beister, Kolditz, and Kalender 2012; Chun, Dewaraja, and Fessler 2014; Luo 2010; Luo et al. 2012; Manley 2013; Rigie, Sanchez, and La Rivière 2015; Sidky and Pan 2008; Zhang et al. 2016) such as total variation (TV) (Sidky and Pan 2008) and PRISM methods (Manley 2013), and convolutional neural network (CNN) methods (Badea, Holbrook, and Clark 2018; Chen et al. 2017, 2018; Gupta et al. 2018; Han, Yoo, and Ye 2016; Jin et al. 2017). All these methods have their advantages and disadvantages. FBP is stable but requires a large number of projections. Iterative methods are more resistant to noises but require more time to reach the solution. CNN methods can gain a relatively high accuracy but require large amount of training data. Currently, FBP is still the most basic and commonly used method in practical applications. With regard to material decomposition in sCT, generally, for a given number of energy bins, the same number of materials can be decomposed (Sukovle and Clinthorne 2003). The authors of (Morrison and Mccammon 1983) proposed to consider X-ray attenuation as the combination of photoelectric absorption, Compton scattering and K-edge components, and used this model for material decomposition. In (Faby et al. 2014), material decomposition was achieved by optimization without constraints such as singular value decomposition (SVD). Other material decomposition methods used optimization with constraints, including local joint sparsity and structural low-rank (DSR) (Xie et al. 2019) and gradient sparsity via bilateral total variation (BTV) (Clark and Badea 2014).

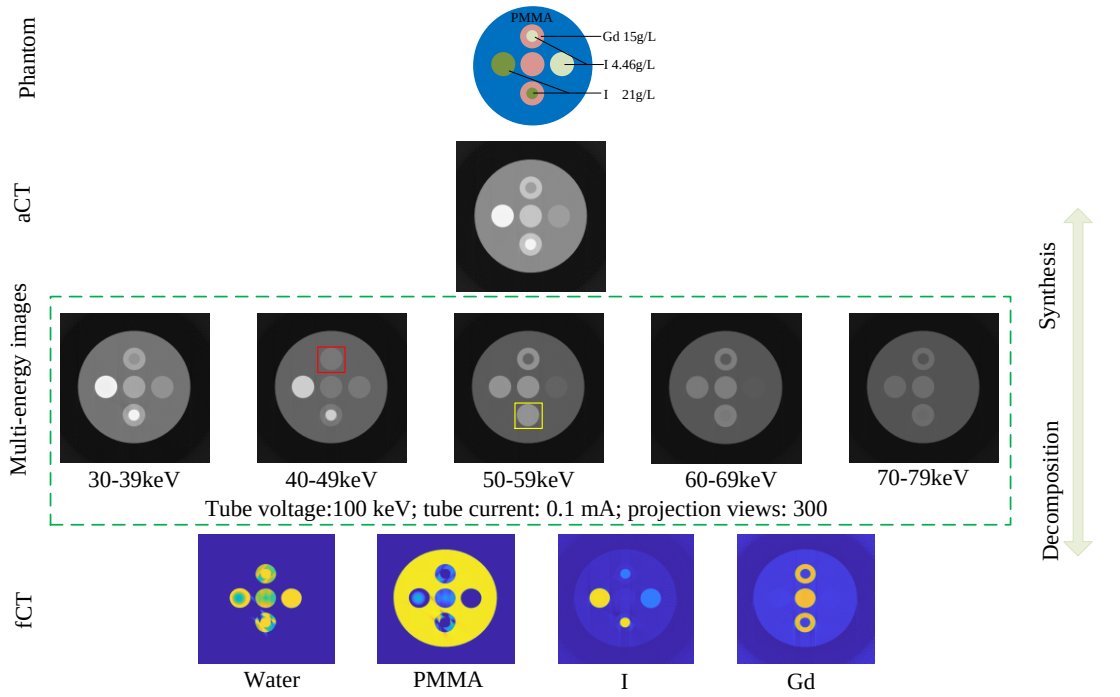

Figure 3.1 Illustration of the ability of sCT to realize simultaneously multimodal anatomical CT (aCT) and functional CT (fCT).

In this chapter, we investigate the potentialities of sCT to perform simultaneously multimodal imaging. The idea consists in using sCT to achieve both conventional anatomical CT (aCT) imaging and new functional CT (fCT) imaging. To this end, a virtual sCT system and a phantom containing different materials of various densities were designed. Then, multi-energy data at different energy bins of the phantom were acquired using the virtual sCT system. Finally, aCT function of sCT was studied using the same configuration as that of conventional CT, and, at the same time, fCT function of sCT was investigated by applying material decomposition algorithms to the same acquired multi-energy data.

3.2 Methods

3.2.1 Imaging configurations

To study the potentialities of sCT, the simulation software Virtual X-ray Imaging (VXI) (Duvauchelle et al. 2000), which allows simulating both conventional CT and sCT systems, was used. In the following, the designed CT system, phantom and data processing are described in detail.

3.2.1.1 CT imaging setting

The CT imaging configuration is illustrated in Figure 3.2. The imaging parameters are given in Table I, which were set for both conventional CT and sCT. The distance from source to rotation center is 200 mm, and that from rotation center to detectors is 400 mm. The pixels of size 0.4 mm × 0.4 mm and thickness 0.3 mm (to ensure the complete absorption of photons) are arranged in a line. Thus, the maximum fan angle of

the X-ray beam is equal to 26° and the field of view (FOV) is 93.3 mm. The detector is based on cadmium telluride (CdTe).

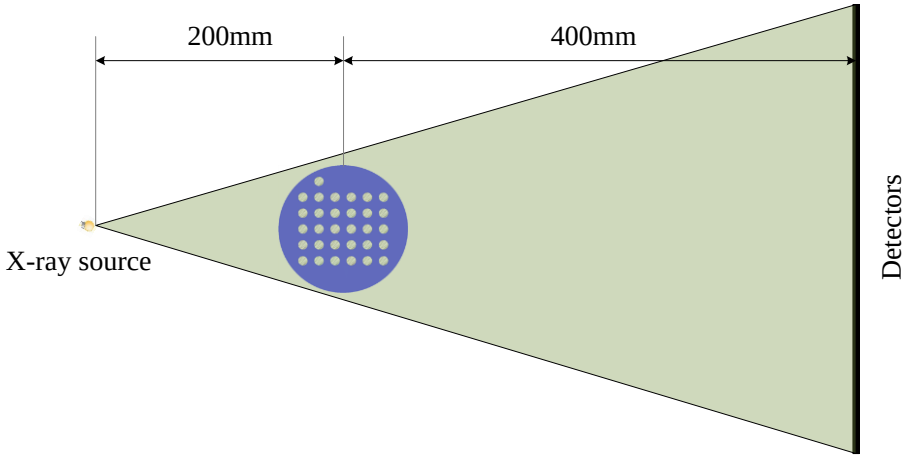

Figure 3.2 CT imaging configuration.

The spectrum was simulated based on Birch & Marshall model (Birch and Marshall 1979) for tungsten target material without filtration. The phantom under the system was scanned in the angle range $0° - 360°$. The source is set as a point generating isotropic X-rays, and thus the geometry unsharpness can be ignored. The kVp was set as respectively 80, 100, 120, and 140 keV to analyze the influence of peak voltage on reconstruction, and the current as 0.1, 1, 10, and 100 mA. The projection views were set as 100, 300, 600, and 1200, respectively. Because of the direct proportion of current and scanning time to photon numbers in X-ray source, prolonging scanning time is equivalent to increasing the current, which implies that they have the same influence on CT in the simulation. For this reason, the influence of scanning time will not be addressed in the present study. Five energy bins ranging from 30-39, 40-49, 50-59, 60-69, and 70-79 keV were set for comparisons with conventional CT.

Table 3.1 CT imaging parameters.

Parameters	Values
Source to rotation center (mm)	200
Detectors to rotation center (mm)	400
Magnification factor	2
Detector pixel	700
Detector pixel size (mm)	0.4 × 0.4
Detector size at the rotation center (mm)	0.13 × 0.13
Fan angle	26°
Pixel thickness (mm)	0.3
KVp (keV)	80,100,120,140
Spectral resolution (keV)	1
Current (mA)	0.1,1,10,100
Projection views	50,100,300,600,1200
Energy bin number (for sCT)	2,3,4,5,6,10,12

3.2.1.2 Phantom

Both conventional CT and sCT were experimented on the phantom shown in Figure 3.3, which is a cylinder made of PMMA with a diameter of 80 mm and thickness of 0.1 mm so that it can be reconstructed as a single slice. It contains 31 holes of diameter 6 mm, which are filled with water and different materials of different concentrations. The holes along each row contain the same material but have different concentrations. Three common contrast agents were considered: Gd, I and iron (Fe). The concentrations of Gd and I were set as 5, 15, 25, 35, 45, 55 mg/cc, and those of Fe as 30, 50, 100, 150, 200 mg/cc. Mixtures are filled with water and all the three contrast agents of the same concentrations in the same column. For example, mixture $1^{\#}$ is made up of water, Gd of 5 mg/cc, I of 5 mg/cc and Fe of 15 mg/cc; mixture $6^{\#}$ contains water, Gd of 55 mg/cc, I of 55 mg/cc and Fe of 200 mg/cc.

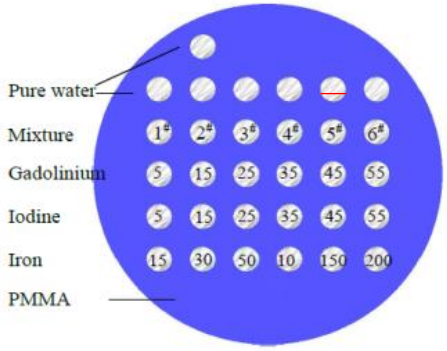

Figure 3.3 The phantom containing different materials of different concentrations.

3.2.1.3 CT model

In X-ray CT, the source generates energy spectrum under the given source voltage, current and scanning time, which corresponds to a specific photon number distribution. When the photons get through the phantom, due to photoelectric effect, Compton scattering and K-edge effect, the photons reaching the detectors will decrease both in number and energy and obey the Beer's law (M 2008)

$$I(E) = I_0(E)\exp\left(-\int_L \mu(\vec{x},E)dl\right), \quad (3.1)$$

where $I_0(E)$ designate the photon numbers generated by the source, $I(E)$ the photon numbers received by the detectors, and $\int_L \mu(\vec{x},E)dl$ the penetrating line integral of the attenuation coefficient for X-ray from source to detector. In X-ray CT, $I_0(E)$ and $I(E)$ are the measurements.

In practice, $I(E)$, also called projection in CT, is noisy because of the presence of quantum noise, electronic noise and statistical noise (Duan et al. 2013)(Gravel, Beaudoin, and De Guise 2004). Quantum noise is directly related to the number of incoming X-ray photons. Electronic noise stems from different sources such as quantization and signal amplification. Statistical noise comes from photon counting by detectors. For sCT equipped with photon-counting detectors, CT projections are expected to have

negligible electronic and quantum noises, and only statistical noise of photons is considered, which often obeys Poisson distribution (Shikhaliev, Xu, and Molloi 2005). Therefore, only Poisson noise with the expectation of ideal photon numbers (Hsieh 2009) is considered in the present study. The detected photons or CT projections with Poisson noise $I_{Poisson}(E)$ can be expressed as

$$I_{Poisson}(E) \sim Poisson(I(E)), p(I_{Poisson}(E)) = \frac{e^{-I(E)} I(E)^{I_{Poisson}(E)}}{I_{Poisson}(E)!}. \quad (3.2)$$

Figure 3.4 shows the ideal sinogram in the 3D form and the sinogram after adding Poission noise.

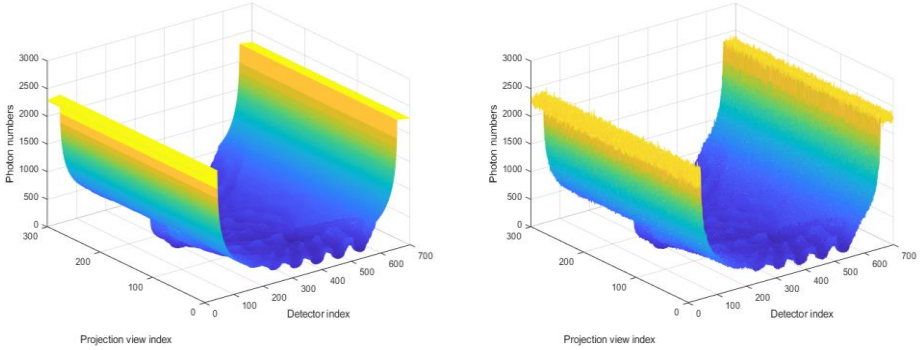

Figure 3.4 Sinogram in the 3D form for the phantom of 300 projection views, 0.1 mA current, and 100 keV tube voltage. (a) ideal sinogram; (b) sinogram added with Poisson noise.

3.2.2 aCT

Anatomical imaging is the main application of conventional CT. It reflects the structure information of the object. Like conventional CT, sCT also has this basic ability, but with an added advantage: multi-energy data from sCT can be used not only for traditional reconstruction, but also for energy-enhanced reconstruction by enhancing data at particular energy bins. In this sense, conventional CT can be regarded as a particular case of sCT where data at all the energy bins are appropriately accounted for. To demonstrate this, we investigate in the following the influence of imaging parameters on reconstruction and compare the reconstruction quality of conventional CT and sCT. To analyse the influence of one parameter, all the other parameters are kept unchanged. Also, to make an objective comparison, reconstructions are performed under the same conditions, including system parameters, phantom and reconstruction method.

3.2.2.1 aCT image of sCT

In conventional CT, there is only one single energy bin (i.e. the whole energy spectrum). Therefore, the anatomical image is obtained through one reconstruction. In contrast, in sCT, since there are three or more energy bins, more than two reconstructions are needed. To obtain the conventional-CT function of sCT, or in other words, to obtain the aCT image of sCT, we first reconstruct different spatial images

corresponding to different energy bins and then average them. Each of the spatial images is reconstructed using the most commonly used FBP algorithm.

To evaluate the reconstructions from conventional CT and aCT, common metrics including root mean square error (RMSE), signal-to-noise ratio (SNR) and contrast-to-noise ratio (CNR) are calculated.

Reconstruction accuracy: the following RMSE is used to calculate the accumulated error of the reconstructed image

$$RMSE(B)=\sqrt{\sum_{\vec{x}}\left(\mu_{\vec{x}}(B)-\mu_{\vec{x}}^{GT}(B)\right)^2\Big/N}, B=1,2,...,K, \quad (3.3)$$

where $RMSE(B)$ is the RMSE for energy bin B, $\mu_{\vec{x}}(B)$ and $\mu_{\vec{x}}^{GT}(B)$ are respectively the reconstructed and ground-truth at position $\vec{x}$ at energy bin B, N is the total number of pixels in the reconstructed image, and K is the number of energy bins (for conventional CT, $K=1$). What is noteworthy is that the ground-truth of each bin is identical due to the attenuation property of the object.

The ground-truth $\mu_x^{GT}(B)$ is obtained as follows. In the simulation, given the source current and voltage, the generated photon numbers at different energies can be obtained from the spectrum. Meanwhile, mass attenuation coefficient at each energy bin can be retrieved from NIST (Hubbell J H 1995). Thus, according to (Le and Molloi 2011), effective mass attenuation coefficient $M(B)$ of a material at energy bin B can be calculated as

$$M(B)=\frac{\sum_{E=E_s(B)}^{E_f(B)}\Phi(E)M(E)}{\sum_{E=E_s(B)}^{E_f(B)}\Phi(E)}, B=1,2,...,K, \quad (3.4)$$

where $\Phi(E)$ designates the number of photons of energy E, $M(E)$ is the mass attenuation coefficient for the material at energy E, and $E_s(B)$ and $E_f(B)$ denote the start energy and finishing energy of energy bin B, respectively. Thus, for a material of concentration ρ, the ground-truth $\mu^{GT}(B)$ is given by

$$\mu^{GT}(B)=M(B)\cdot\rho, B=1,2,...,K, \quad (3.5)$$

where $M(B)$ denotes the effective mass attenuation coefficient of energy bin B. For a mixture of P materials at position x, the ground-truth can be expressed as the total attenuation coefficient (M 2008)

$$\mu_{\vec{x}}^{GTT}(B)=\sum_{i=1}^{P}\mu_{\vec{x}}^{GT,i}(B), B=1,2,...,K, \quad (3.6)$$

with $\mu_{\vec{x}}^{GT,i}(B)$ denoting the attenuation coefficient of material i,which can be calculated using Equation (3.5).

- *SNR:* SNR is employed to evaluate the noise level of reconstructed images. The SNR at energy bin B is defined by

$$SNR(B)=10\log\left(\sum_{\vec{x}}\left\|\mu_{\vec{x}}^{GT}(B)\right\|^2\Big/\sum_{\vec{x}}\left\|\mu_{\vec{x}}(B)-\mu_{\vec{x}}^{GT}(B)\right\|^2\right), B=1,2,...,K. \quad (3.7)$$

- *CNR:* CNR is a metric used to evaluate the contrast between region of interest (ROI) and background. In the present study, the 31 dug holes filled up with materials are regarded as ROIs, and the remaining PMMA as background. Thus, CNR at energy bin B is given by

$$CNR(B) = \frac{|\bar{\mu}_{ROI}(B) - \bar{\mu}_{BG}(B)|}{\sqrt{\sigma^2_{ROI}(B) + \sigma^2_{BG}(B)}}, B = 1, 2, ..., K, \quad (3.8)$$

where $\bar{\mu}_{BG}(B)$ (or $\bar{\mu}_{ROI}(B)$) represents the mean attenuation coefficient of background (or ROI), and $\sigma_{BG}(B)$ (or $\sigma_{ROI}(B)$) the standard deviation of the latter.

3.2.2.2 Enhanced aCT image of sCT

As mentioned above, different images corresponding to different energy bins are acquired and reconstructed in one single scanning. These spatial images have different attenuation coefficients but are intrinsically correlated. Generally, images at low-energy bins have higher CNR but lower SNR due to the small number of detected photons, whereas images at high-energy bins show the opposite characteristics. Indeed, for materials without K-edge, their attenuation coefficient decreases with energy. The difference in attenuation coefficient between materials is much larger at low-energy bins than at high-energy bins, thus resulting in higher CNR. But for materials with K-edge, the attenuation coefficient at K-edge energy will suddenly increase, thus leading to higher CNR at the current energy bin. Based on this remark, the idea here is to exploit the characteristics related to energy bins for synthesizing an (anatomical) image having both higher SNR and higher CNR, which leads to what we call the enhanced aCT image (with respect to conventional CT) of sCT.

Assume that the reconstructions at energy bins i and j give respectively the highest CNR and SNR among all energy bins. To get an image with both high CNR and high SNR, the photon numbers are added to reconstruct an enhanced image given by

$$I^{Enhancement} = I^i_{Poisson} + I^j_{Poisson}, \quad (3.9)$$

and

$$I_0^{Enhancement} = I_0^i + I_0^j, \quad (3.10)$$

where I_0^i (or I_0^j) and $I^i_{Poisson}$ (or $I^j_{Poisson}$) designate, at energy bin i (or energy bin j), the generated photon numbers and the received photon numbers with Poisson noise, respectively. $I_0^{Enhancement}$ and $I^{Enhancement}$ represent the synthesized (enhanced) data. In such way, information at two different energy bins is combined to form a new pair of data, which can be used for enhancing reconstructed images. Such enhancement is achieved by two mechanisms. First, adding the data reduces noise, thus improving the SNR. Second, the decreased standard variations σ_{ROI} and σ_{BG} increase CNR according to Equation (3.8). In principle, information from any two energy bins could be exploited for enhancement, but with energy bins having high CNR, the enhancement is more visible.

To evaluate the above-enhanced reconstruction, the following SNR of ROI is also used

$$SNR_{ROI} = \mu_{ROI} / \sigma_{ROI} \,. \qquad (3.11)$$

3.2.3 fCT

As stated above, sCT can achieve aCT imaging of an object by measuring its anatomical or morphological characteristics. It can also at the same time achieve the aforementioned novel fCT function (with respect to conventional CT). Given multiple (at least three) datasets (projection data or spatial images corresponding to different energy bins) delivered by sCT, the spatial distribution of materials contained in the object can be obtained by applying a mathematical material decomposition algorithm. Thus, sCT accomplishes a sort of functional imaging of the object.

fCT images from sCT are in the form of a series of so-called material images, each of which is a spatial image representing the spatial distribution of one material. The material images can be obtained either in projection domain or in image domain (Foygel Barber et al. 2016; Li et al. 2015, 2017; Mechlem et al. 2018; Palareti et al. 2016; Taguchi et al. 2007) or still in a one-step manner from projection data without reconstructing explicitly spatial images. In the present study, we perform material decomposition in image domain.

As indicated by Equation (3.6), linear attenuation coefficient can be expressed as the linear combination of materials. Combining the attenuation coefficients of all the energy bins leads to

$$\begin{bmatrix} \mu_{\vec{x}}(1) \\ \vdots \\ \mu_{\vec{x}}(K) \end{bmatrix} = \begin{bmatrix} M^1(1) & \cdots & M^P(1) \\ \vdots & \ddots & \vdots \\ M^1(K) & \cdots & M^P(K) \end{bmatrix} \begin{bmatrix} \rho_{\vec{x}}^1 \\ \vdots \\ \rho_{\vec{x}}^P \end{bmatrix} \qquad (3.12)$$

where $M^i(B)$ and $\rho_{\vec{x}}^i$ denote respectively the mass attenuation coefficient at energy bin B and the concentration at position $\vec{x}$ of material i. Applying Equation (3.12) to all the pixels of the image yields the spatial distribution of materials. In other words, after sCT reconstructions, fCT images (i.e. spatial material images) can be derived from reconstructed sCT images. In the present study, based on FBP reconstructions, $\ell 1$-norm minimization method was used for material decomposition. The results were compared and evaluated both visually and quantitatively using RMSE.

3.3 Experiments and Results

3.3.2 aCT

This subsection aims to show what sCT can produce as anatomical images (aCT) and compare aCT images from sCT with conventional CT images for different configurations of projection views, current and voltage.

3.3.2.1 aCT images with respect to conventional CT images

A. Projection views

Projection views reflect the density of sampling angles, which provides information at different directions. More projection views mean more information, but at the same time increase CT dose. In the present experiment, under the same source current and voltage, reconstructions from respectively 50, 100, 300, 600 and 1200 projection views were compared. The source voltage was set as 100 keV, and the current as 0.1 mA.

Table 3.2 gives the reconstruction results in terms of RMSE and SNR. For the same projection views, aCT shows better performance than conventional CT in terms of both RMSE and SNR. Compared to conventional CT, the SNRs of aCT are improved respectively by 3%, 169%, 264%, 317%, 355% for 50, 100, 300, 600 and 1200 projection views. Taking 50 projection views as a reference, the SNR improvement for conventional CT is 63%, 111%, 122%, 128% with the increase of projection views, while that for sCT is 168%, 441%, 587%, 687%. That is, the increase of projection views improves the performance of both conventional CT and aCT, but the improvement is much more obvious for aCT than for conventional CT.

Table 3.2 RMSE and SNR comparisons between conventional CT and aCT for different projection views.

Projection views		50	100	300	600	1200
RMSE	Conventional CT	0.5510	0.5214	0.5008	0.4960	0.4942
	aCT	0.2564	0.1733	0.0930	0.0667	0.0533
SNR	Conventional CT	1.9206	3.1302	4.0499	4.2771	4.3787
	aCT	1.9730	5.2999	10.6764	13.5568	15.5221

Figure 3.5 shows the reconstruction results from 300 projections. CNR was also calculated in the ROIs (31 holes in the phantom) for conventional CT and aCT (Figure 3.5(c)). In the ROIs that consist of water, mixture, Gd, I, or Fe, the ROIs reconstructed from aCT have higher CNRs than conventional CT, which is also consistent with what is visually observed. The CNRs of aCT are always higher than those of conventional CT. As shown in Figure 3.6(a), with the increase of projection views, the CNRs of both aCT and conventional CT increase, but CNRs of aCT are always higher than those of conventional CT, especially in the case of fewer projections.

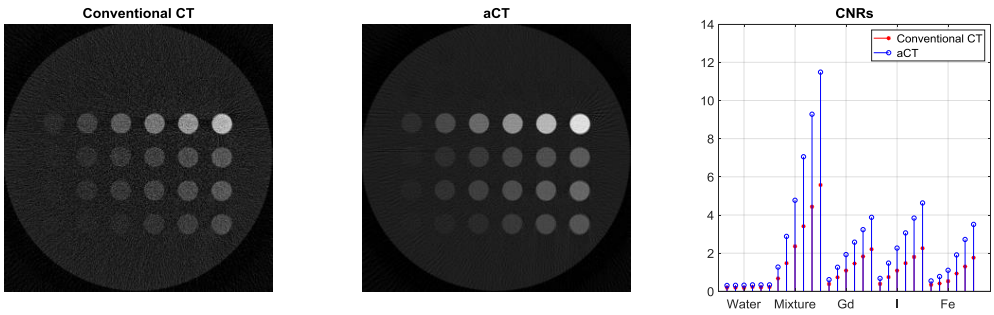

(a) (b) (c)

Figure 3.5 Images reconstructed from: (a) conventional CT; (b) aCT, and (c) CNRs of ROIs, with 300 projection views, 0.1 mA source current and 100 kVp.

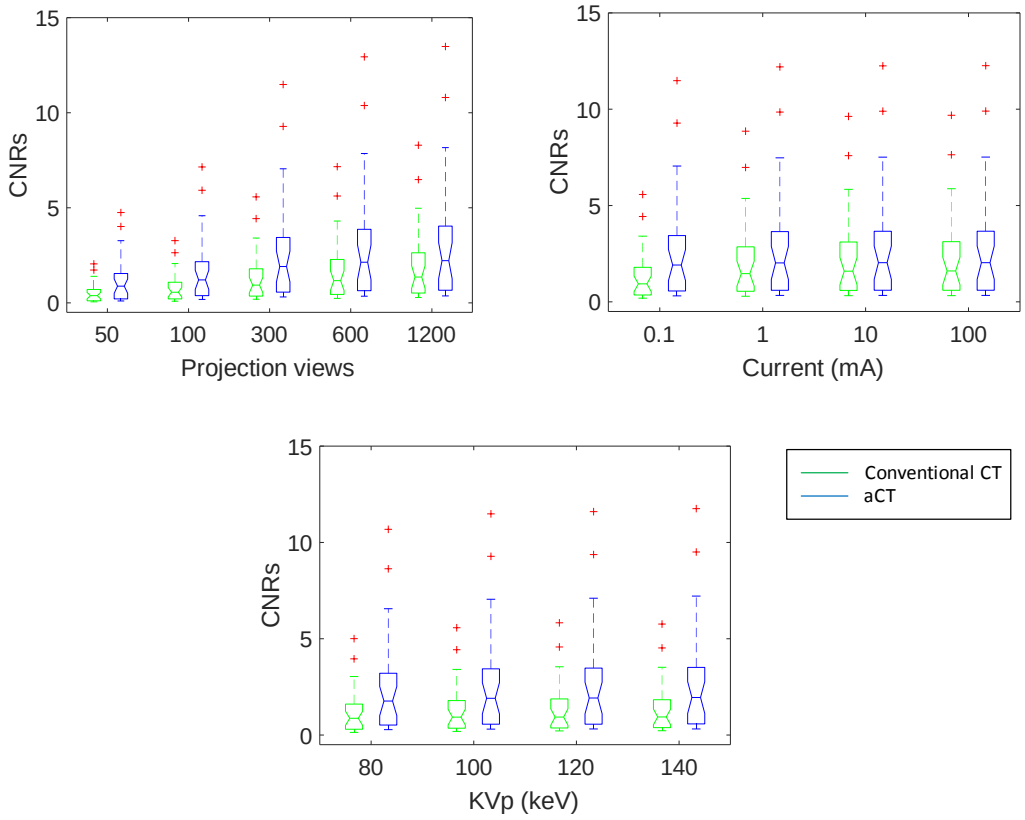

Figure 3.6 Comparison between conventional CT (green line) and aCT (blue line) in terms of CNRs for: (a) different projection views; (b) different source currents; (c) different source voltages.

B. Current

The current determines the dose of X-rays for each projection view under the given source voltage. With the increase of current in the source, the number of generated photons will increase, which will increase SNR. Table 3.3 RMSE and SNR comparison between conventional CT and aCT with different source currents. gives the RMSEs and SNRs of conventional CT and aCT under different currents, with the fixed 100 keV source voltage and 300 projections. aCT exhibits clearly better performance than conventional CT in terms of RMSE and SNR. When the source current is increased from 0.1 to respectively 1, 10 and 100 mA, the SNR of aCT is increased respectively by 164%, 267%, 282%, 284% with respect to conventional CT. If fixing 0.1 mA source current as a reference, the SNR improvement is 9%, 9.6%, 9.7% for conventional CT, whereas for aCT, it is 51%, 59%, 60%. That is, with the increase of current, both conventional CT and aCT experience an increase in performance, but the increase is much more important in the case of aCT.

Table 3.3 RMSE and SNR comparison between conventional CT and aCT with different source currents.

Current (mA)		0.1	1	10	100
RMSE	Conventional CT	0.5008	0.4939	0.4935	0.4934
	aCT	0.0930	0.0516	0.0481	0.0477
SNR	Conventional CT	4.0499	4.4006	4.4372	4.4411
	aCT	10.6764	16.1667	16.9414	17.0320

Figure 3.6(b) illustrates the CNRs for different source currents. The CNRs of aCT are always higher than conventional CT, especially at low currents, namely low dose. With the increase of current, the CNRs of both aCT and conventional CT increase, but the increase is less important with respect to the case of increasing projection views.

C. Voltage

Voltage influences the energy spectrum of the source. Under higher voltage, the source generates more photons and the energy distribution also changes. In the present study, the reconstruction results for 80, 100, 120 and 140kVp were evaluated for the fixed current of 0.1 mA and 300 projection views. Table 3.4 compares RMSEs and SNRs for different source voltages. Under the same voltage, sCT exhibits smaller RMSEs and greater SNRs than conventional CT. With the increase of voltage, RMSE decreased and SNR increased for both sCT and conventional CT, but the rate of improvement tends to decrease.

Table 3.4 RMSE and SNR comparison of conventional CT and aCT with different source voltages.

Source voltage (keV)		80	100	120	140
RMSE	Conventional	0.6832	0.5008	0.3692	0.2949
	aCT	0.1250	0.0930	0.0828	0.0769
SNR	Conventional	3.5640	4.0499	4.6891	5.1759
	aCT	8.2532	10.6764	11.7297	12.4084

Figure 3.6(c) gives the CNRs for different voltages. The CNRs of sCT are always higher than those of conventional CT. With the increase of source voltage, the CNRs of both sCT and conventional CT increase.

In summary: 1) Under the same conditions, reconstructions from sCT always show better performances than those from conventional CT, especially at low dose; 2) With the increase of projection views, current and voltage, reconstructions from both conventional and sCT improve; 3) Performance improvement tends to be small when increasing just one parameter among projection views, current or voltage; 4) Performance improvement is more obvious with current than with voltage.

3.3.2.2 Enhanced aCT images

To study enhanced aCT images, energy bins were respectively set as 30-39, 40-49, 50-59, 60-69, and 70-79 keV. The K-edge energy is located in the energy bin of 50-59 keV for material Gd, and 30-39 keV for material I. So, for Gd, the effective attenuation in the energy bin 50-59 keV is the highest among the five bins, and for I in 30-39 keV.

Therefore, we focused on these two energy bins to study the visibility of Gd and I (with the fixed source current of 0.1 mA and projection views of 300). To enhance the CNR of Gd and I, we used the image of 70-79 keV due to its highest SNR among the five bins. Figure 3.7 shows, for the investigation of Gd, the comparison between the original image at the energy bin 50-59 keV and its enhanced version by adding the image from the energy bin 70-79 keV. Likewise, for the investigation of I, Figure 3.7 shows the comparison between the original image at the energy bin 30-39 keV and its enhanced version by adding the image from the energy bin 70-79 keV. As observed, by adding the data from another energy bin with the highest SNR to the current image of interest (with the highest SNR), we succeeded in obtaining an enhanced image presenting both higher CNR and higher SNR with respect to the original image. More quantitative results are given in Table 3.5. Actually, adding two images from two different energy bins improves CNR and SNR. If more bins are considered, improvement in SNR will be more obvious, but CNR may not be improved significantly because of lower CNR in other energy bins. For materials with K-edge, the improvement is particularly visible. Taking another example on the material Fe that does not have K-edge in the energy range stated above, we show in Figure 3.7 the original image at the energy bin 30-39 keV and its enhanced version by adding the image from the same energy bin 70-79 keV. We can observe similar results.

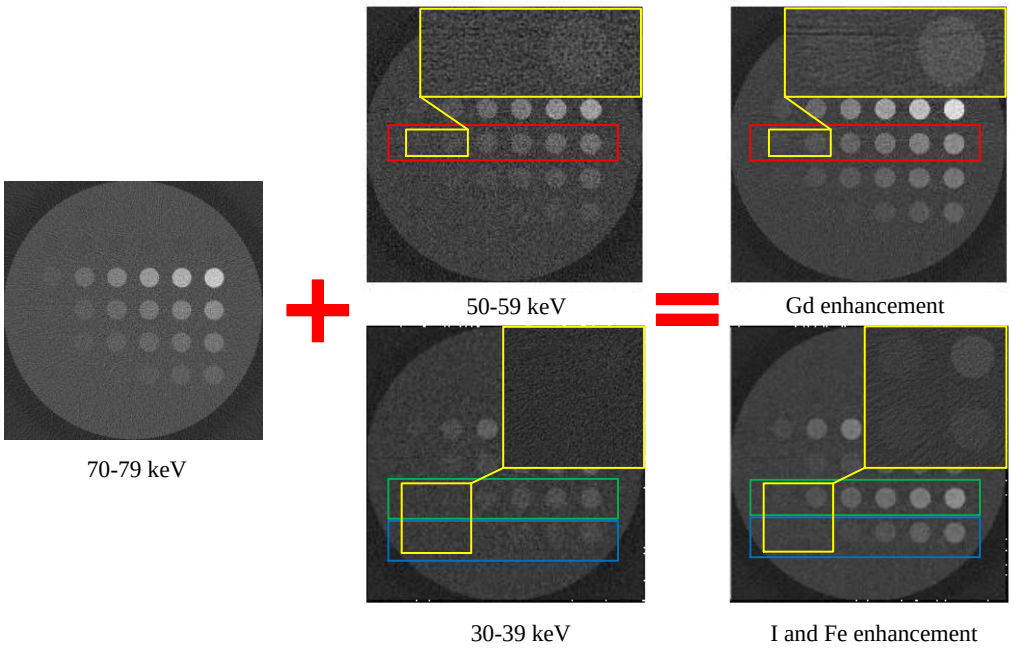

Figure 3.7 CNRs and SNRs comparison of original images (middle column) at the energy bins 30-39 keV and 50-59 keV and their enhanced version (right column) by averaging them with the image from the energy bin 70-79 keV (left column). The visibility of Gd (red box region), I (green box region) and Fe (blue box region) are clearly improved, and the region containing low-concentration materials (yellow box region) are zoomed up (right upper corner). All the images are displayed in a normalized form.

Table 3.5 Comparison of SNR of ROI and CNR between original and enhanced images.

	SNR of ROI (dB)						CNR					
Concentration (mg/cc)	5	15	25	35	45	55	5	15	25	35	45	55
50-59keV	3.48	5.07	6.68	8.30	9.87	11.41	0.67	1.54	2.42	3.30	4.18	5.03
Gd enhancement	4.21	6.14	8.10	10.04	11.95	13.81	0.72	1.68	2.66	3.62	4.57	5.50
30-39keV	2.23	3.27	4.26	5.25	6.22	7.28	0.60	1.35	2.04	2.74	3.42	4.16
I enhancement	3.08	4.51	5.91	7.31	8.73	10.18	0.66	1.47	2.24	2.99	3.76	4.57
Concentration (mg/cc)	15	30	50	100	150	200	15	30	50	100	150	200
30-39keV	2.21	2.66	3.22	4.73	6.20	7.68	0.59	0.90	1.30	2.36	3.41	4.45
Fe enhancement	2.86	3.31	3.91	5.45	6.97	8.56	0.65	0.98	1.43	2.60	3.74	4.89

To further evaluate the ability of sCT to enhance aCT images, we have also performed the same experiment on real data acquired using physical sCT. The used physical phantom contains Gd, I, Water and PMMA with various concentrations (Figure 3.8). It was scanned by 150 keV voltage divided into 5 bins: 27-47 keV, 48-58 keV, 59-68 keV, 69-79 keV, and 80-150 keV. The original multi-energy images and the enhanced images are shown in Figure 3.9. The contrast of materials Gd and I is clearly enhanced after combining two multi-energy images corresponding to two energy bins. Also, the SNR (calculated on ROIs) of the enhanced images is also significantly improved (Figure 3.10).

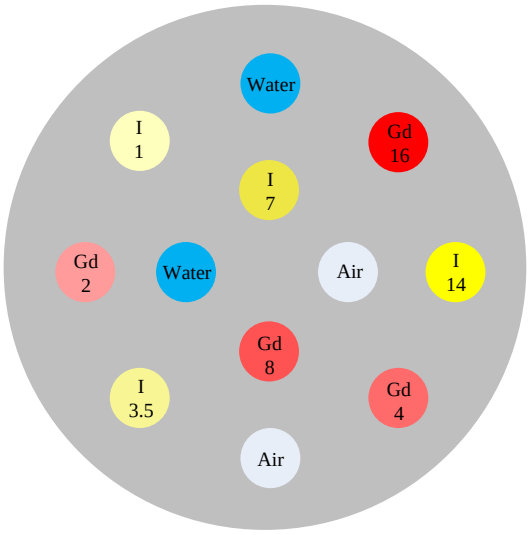

Figure 3.8 Phantom illustration for physical CT.

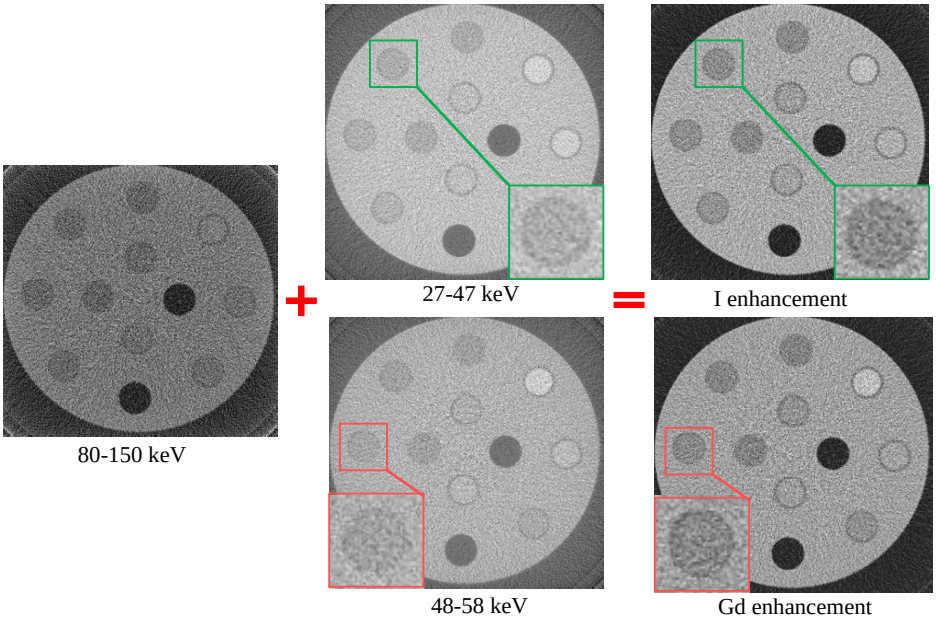

Figure 3.9 Enhancement of aCT on real data acquired using physical sCT.

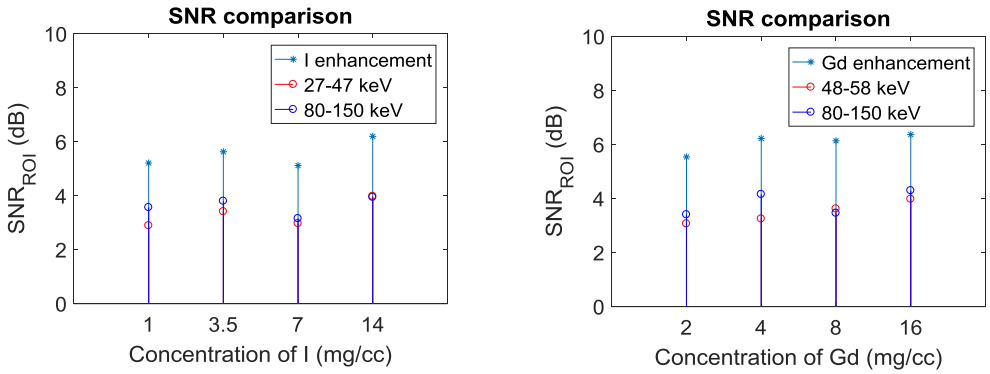

Figure 3.10 SNR comparison for the original images and the enhanced images.

3.3.3 fCT

fCT images from sCT are spatial material images shown in Figure 3.11 for different source currents. The ground-truth contains PMMA, Water, and Gd of 55 mg/cc, I of 55 mg/cc and Fe of 200 mg/cc. The fCT images at the source current of respectively 0.1 mA, 1 mA, 10 mA and 100 mA with the source tube fixed as 100 keV and projection view as 300. Visually, the increase of current reduces the noise and the fCT images are closer to ground-truth for all the materials under investigation.

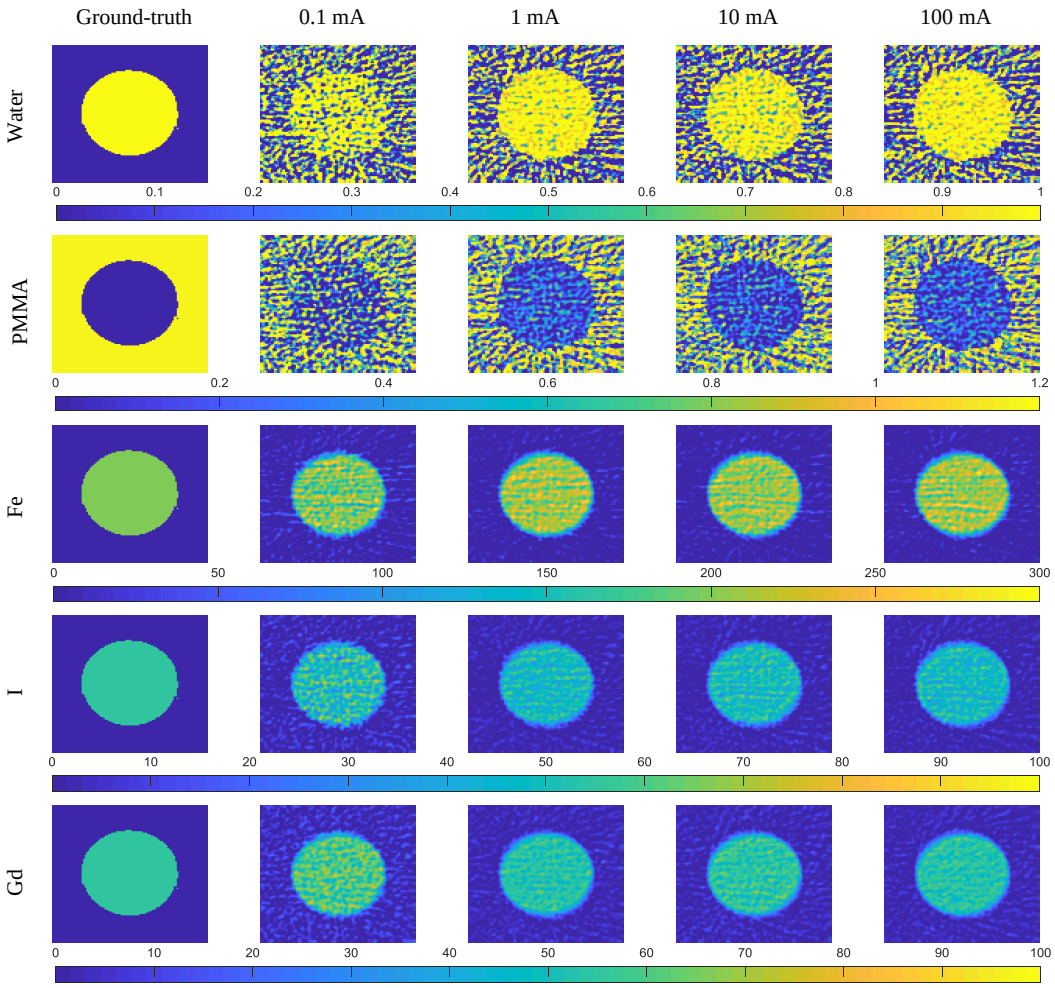

Figure 3.11 Material decomposition of the mixture 6# (PMMA, water, Gd of 55 mg/cc, I of 55 mg/cc and Fe of 200 mg/cc) in Figure 3.3 under four different source currents in sCT. The first column is the ground-truth of the materials. The source voltage was fixed as 100 keV and the projection views as 300.

Figure 3.12 shows the fCT images for different source voltages. The fCT images at the source voltage of respectively 80 keV,100 keV, 120 keV and 140 mA with the source tube fixed as 0.1 mA and projection view as 300. Figure 3.13 shows the fCT images for different projection views, including 50, 100, 300, 600 and 1200, with the source tube fixed as 0.1 mA and 100 keV. The results with higher voltages and more projection views is more resistant the noise and the fCT images are closer to ground-truth for all the materials under investigation.

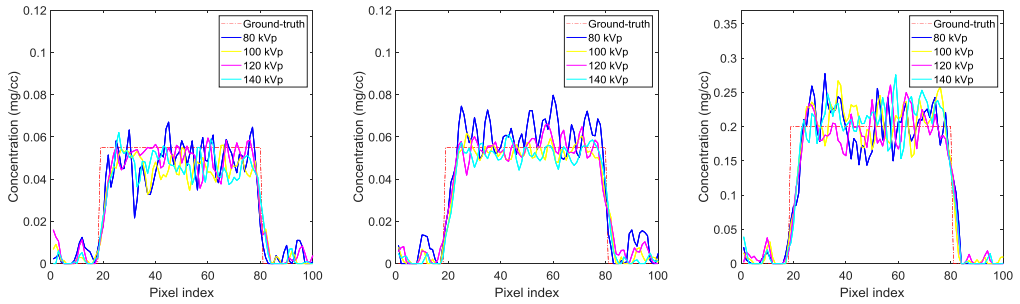

(a) (b) (c)

Figure 3.12 Material decompostion results of the mixture 6# in Figure 3.2 for different voltages kVp. (a) Gd; (b) I; (c) Fe.

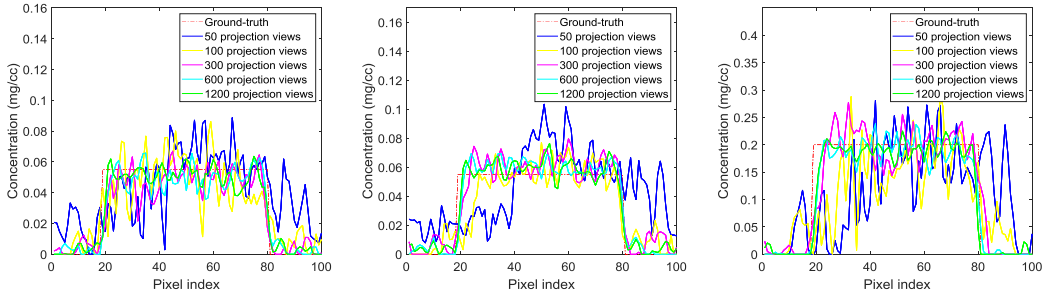

(a) (b) (c)

Figure 3.13 Material decompostion results of the mixture 6# in Figure 3.2 for different projection views. (a) Gd; (b) I; (c) Fe.

More quantitatively, RMSEs of fCT images are given in Table 3.6 for different parameters, including source current, source voltage and projection views. The RMSE values are much greater for PMMA and water than for the other 3 materials, due to the fact that PMMA and water have similar attenuation coefficient characteristics, thus making them difficult to be separated in noisy conditions. Because of their K-edge characteristic, Gd and I are better decomposed.

Meanwhile, fCT from sCT was also validated on the physical phantom shown in Figure 3.8. The results are displayed in Figure 3.14. The background made of plastic without K-edge effect being similar to water, it was, as expected, decomposed into water (or more exactly water-like material but of higher concentration than water). Gd and I of high concentrations (yellow holes) are clearly brought out; Gd (or I) of low concentrations inferior or equal to 4 mg/cc (or inferior or equal to 3.5 mg/cc) are much more difficult to distinguish. Although not perfect because of the presence of noise and artifacts, the decomposed images depict clearly the spatial distribution of materials in the phantom.

Table 3.6 RMSEs of fCT for each material and different parameters.

Parameters \ Material		PMMA	Water	Gd	I	Fe
Source current (mA)	0.1	0.2722	0.2748	0.0030	0.0030	0.0070
	1	0.2329	0.2366	0.0021	0.0021	0.0059
	10	0.2393	0.2403	0.0019	0.0020	0.0057
	100	0.2321	0.2369	0.0019	0.0020	0.0057
Source voltages (kVp)	80	0.3060	0.3426	0.0047	0.0051	0.0195
	100	0.2722	0.2748	0.0030	0.0030	0.0070
	120	0.2176	0.2172	0.0019	0.0017	0.0038
	140	0.1894	0.1928	0.0016	0.0014	0.0033
Projection views	50	0.3018	0.3370	0.0050	0.0052	0.0175
	100	0.2959	0.3159	0.0040	0.0042	0.0126
	300	0.2722	0.2748	0.0030	0.0030	0.0070
	600	0.2534	0.2494	0.0024	0.0024	0.0052
	1200	0.2355	0.2313	0.0020	0.0020	0.0042

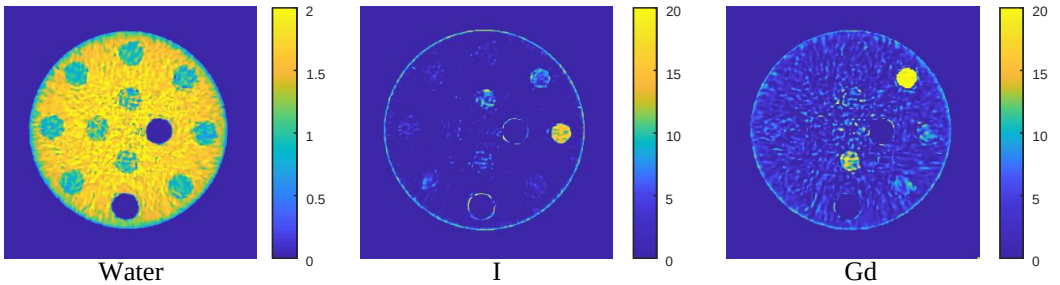

Figure 3.14 fCT images from sCT of the physical phantom. The value of pixels represents the concentration of the material in mg/cc.

3.3.4 sCT parameter settings

3.3.4.1 Energy bin numbers selection

As demonstrated till now, sCT can be used to perform simultaneously, in one single acquisition, both aCT and fCT of the object. A fundamental characteristic of sCT is its ability to acquire images at multiple energy bins (at least 3 to be different from dual-energy CT). Theoretically, the number of energy bins will affect the quality of aCT and fCT. Intuitively, for a fixed energy range, if the number of energy bins is large, the width of each energy bin will be narrow and the photons reaching each detector will decrease, thus leading to more important noise and lower reconstruction quality. In contrast, less energy bins mean wider energy bin width and less energy selectivity, thus resulting in higher reconstruction quality but lower material decomposition quality. It was shown that if the energy bin edge is set near the K-edge of a material,

decomposition results will be improved (Shikhaliev 2012). Therefore, to ensure quality in both reconstruction and decomposition, a compromise is to be done between image quality and energy bin numbers. In the following, we present the results on the influence of energy bins on the quality of aCT and fCT.

In our experiments, the source voltage was set as 100 keV, source current as 0.1 mA, and projection views as 300. The available energy range was 30-89 keV, which was respectively divided into 2, 3, 4, 5, 6, 10 and 12 bins. This results in 7 different energy-bin widths of 30, 20, 15, 12, 10, 6 and 5 keV, respectively. Reconstruction algorithm was FBP and material decomposition was achieved using $\ell 1$-norm minimization on reconstruction results. Figure 3.15 shows the RMSEs of aCT and fCT for different number of energy bins. For aCT, its RMSEs increase with the increase of energy bins. This is due to the decrease of photon numbers within each energy bin, thus increasing the noise. For fCT, its RMSEs do not exhibit a clear trend. In theory, with more energy bins, material attenuation curve will be more densely sampled and information will be more redundant, which is beneficial for material decomposition. However, more energy bins will also increase the noise within each bin due to the narrower energy bin width, which will have negative influence on material decomposition. Thus, in the end, material decomposition based on reconstructed images does not always improve with the increase of energy bin numbers.

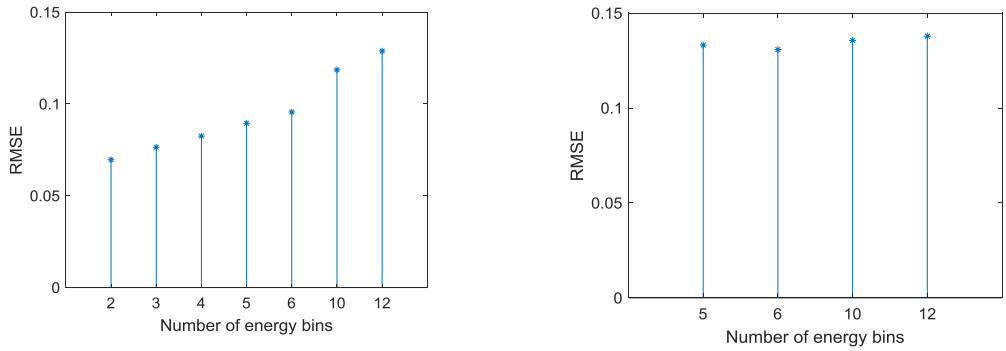

(a) (b)

Figure 3.15 RMSEs of aCT and fCT for different number of energy bins. (a) aCT; (b) fCT.

3.3.4.2 Current selection with respect to conventional CT

As observed, when used as aCT, sCT gains, under the same imaging parameters, better performance compared to conventional CT. The question is then what source current might be taken in conventional CT to get the same image quality as that in aCT. This is a crucial issue in clinical applications since source current is directly related to X-ray dose.

To answer this question, a phantom shown in Figure 3.16 was designed, which presents 9 ROIs (5 holes and 4 rings) filled with material Gd (green parts) of density 5 mg/cc and I (yellow disks) of density 5 mg/cc on the cylinder made of PMMA. Also, 5 ROIs are labelled in the phantom, including 4 holes of I with the radius of 30 mm (number 1), 15 mm (number 2), 7.5 mm (number 3) and 3 mm (number 4), and 1 hole of

Gd (number 5) with the radius of 60 mm. The radius of PMMA is 300 mm, and reconstruction size is 800×800. The projection views and source voltage were fixed as 300 and 100 kVp, respectively.

In the experiment, the source current for aCT was selected as 0.1 mA because the number of photons with this current is in the same order of magnitude as that with physical sCT operating with 200 mA and bow tie filter. For the same source current 0.1 mA, ROI 4 (radius 3 mm) is detected in aCT but is not distinguished in conventional CT (zoomed version in the upper right corner in Figure 3.16). Likewise, for ROI 3 (radius 7.5 mm), it is clearly visible in aCT but is not readily visible in conventional CT. When the source current for conventional CT is increased 10 times with respect to aCT, from 0.1 mA to 1 mA, the reconstructions of conventional CT and aCT show visually similar quality, and the reconstructed images also have the same order of magnitude. The 10-times increase of source current for conventional CT has made the SNR of the latter close to, but still lower than, that of aCT. The results show that conventional CT could get the same reconstruction quality as that of aCT by increasing 10 times the source current. Since increasing source current (fixing the other parameters) amounts to increasing radiation dose, 10 times the cube current implies roughly raising the dose to 10 times. In other words, according to these simulation results, if replacing conventional CT by sCT, only about $1/10$ of the dose would be necessary for the same reconstruction quality.

Table 3.7 gives the SNRs of the 5 hole ROIs under other currents. When increasing the current of conventional CT to 1 mA, namely 10 times that of sCT, the SNR of conventional CT almost achieves but is still lower than the SNR of sCT. Furthermore, when further increasing the current of conventional CT, the improvement of SNR slows down, which is consistent with the simulation results in Section 3.1. By calculating the ratio of sCT SNR (averaged over all the ROIs) to conventional-CT SNR (averaged over all the ROIs) for the same dose (0.1 mA), the sCT SNR is 3.70 times the conventional-CT SNR.

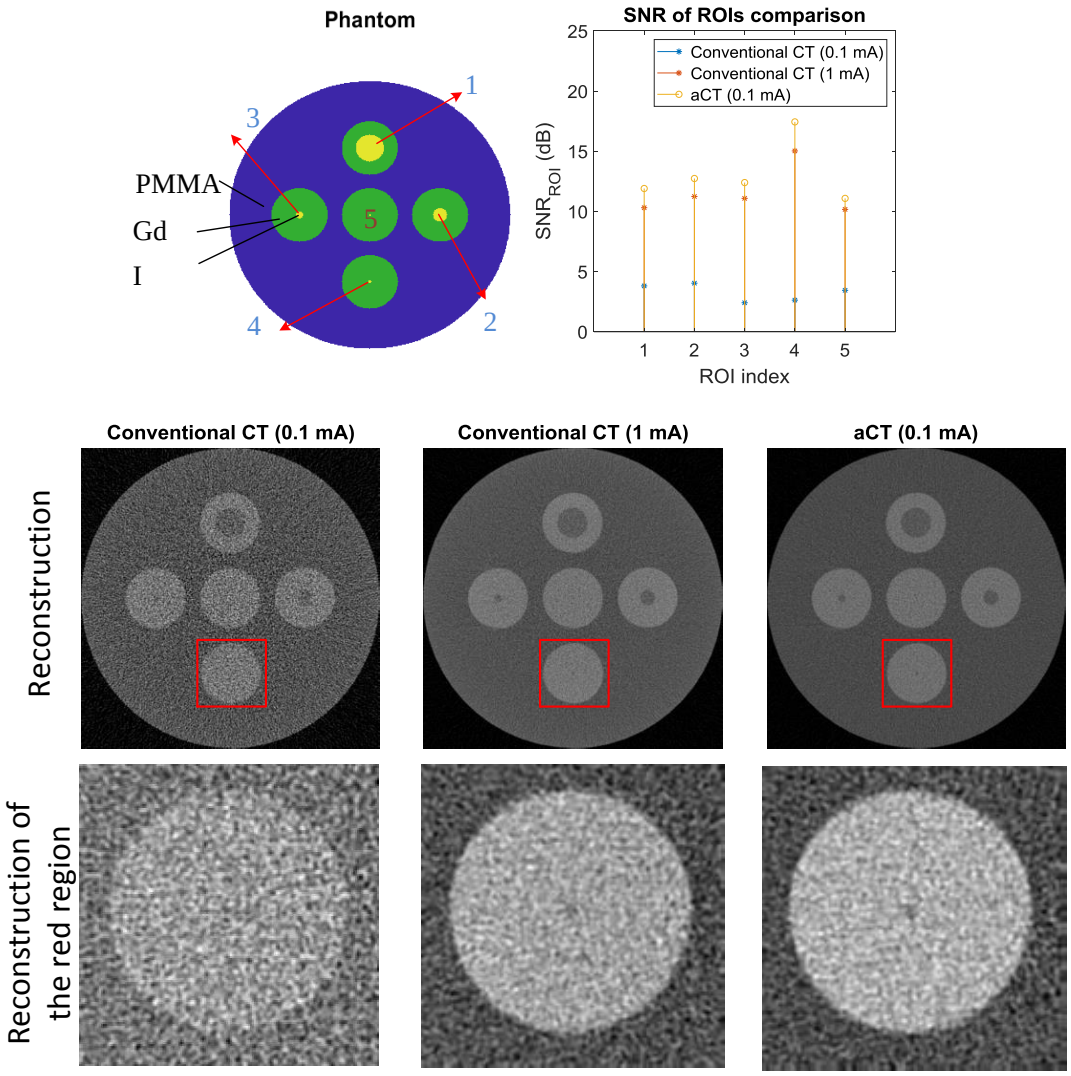

Figure 3.16 Comparison between aCT image from sCT and conventional CT image. The zoomed region contains the small 3-mm-radius hole (in the center of the region filled with iodine of density 5 mg/cc).

Table 3.7 SNRs of 5 hole ROIs for different source currents.

CT type \ Radius / Current (mA)		I (5 mg/cc)				Gd(5 mg/cc)	Average SNR ratio by sCT
		30	15	7.5	3	60	
sCT	0.1 mA	11.59	13.24	12.09	12.14	11.49	1
Conventional CT	0.1 mA	3.72	3.88	3.15	2.27	3.33	3.70
	1 mA	10.31	10.93	9.92	9.45	10.00	1.20
	10 mA	18.58	23.36	30.62	31.20	21.12	0.49
	100 mA	20.39	28.02	73.28	98.32	26.22	0.25

3.4 Discussion

We have investigated the potentialities of sCT with respect to conventional CT through simulations. The results showed that, based on photon-counting technology, sCT can accomplish not only usual tasks of conventional CT but also at the same time new functional imaging, and this with one single acquisition. Compared to conventional CT, aCT function of sCT gained better performance under the same condition. This can be explained by the fact that the photon utilization efficiency of sCT is higher than that of conventional CT (Willemink et al. 2018). As a result, sCT is more resistant to noise. Moreover, the possibility of averaging signals corresponding to different energy bins in sCT allowing further reducing noise. It is however worth noting that, in our simulation, only statistical noise was considered whereas, in practice, conventional CT has noticeable quantum noise (caused by random distribution over the surface of detectors) and electronic noise (caused by analog electronic circuits converting analog signal to digital signal in the detection system) (Hanson 1981), which will make data even noisier. Therefore, performance improvement of aCT function from sCT with respect to conventional CT would be more significant.

Combining data from different energy bins enabled us to enhance the image by improving its CNR and SNR. The involved mechanism is the following. In the case of material with K-edge, the attenuation coefficient suddenly increases at the K-edge energy, thus leading to larger CNR. However, the SNR at the energy bin covering the K-edge is not necessarily as high as expected. Therefore, combining the energy bin with K-edge and that with high SNR leads to a synthesized image presenting both high CNR and SNR. In the case of material without K-edge, due to the attenuation curve property that the difference of attenuation is larger at low energy than at high energy, the CNR is higher at low energy bin than at high energy bin. Thus, as in the case of K-edge material, combining low and high energy bins produces a synthesized image presenting both high CNR and SNR. On the other hand, combining data increases in fact the number of involved photons, thus reducing noise. At the same time, noise in each energy bin obeys Poisson distribution and noises in different energy bins are independent; adding the data then reduces the noises. In the present study, data from two energy bins were added to obtain the enhanced image; other methods to fusion different energy-bin data are however possible.

Material decomposition is one of the two prominent functions of sCT. With the increase of projection views and current, the material decomposition performance of sCT improved significantly. This is due to the fact that, in the present study, fCT images were obtained from reconstructed images. As a result, material decomposition performance was directly influenced by the quality of reconstructed images.

sCT allowed us to achieve simultaneously aCT and fCT. However, aCT and fCT imaging qualities may evolve in the opposite direction. For instance, increasing the number of energy bins (with the other parameters fixed) means, for the same energy range, narrower bin-width, thus resulting in larger noise in reconstructed images and deteriorating aCT quality. But at the same time, more energy bins mean providing more

points on the attenuation coefficient curve, thus improving fCT quality by increasing the resolution in energy (i.e. energy-resolving capability). Therefore, choosing an appropriate number of energy bins is an important issue in sCT for a given application. In the present study, 5 or 6 energy bins were a good compromise between aCT imaging quality and fCT imaging quality.

As observed, aCT from sCT has detected much smaller objects than conventional CT under the same condition. This can be explained from the following two aspects. First, in conventional CT, the detection mechanism is to convert X-ray photons to visible photons that are then converted into electrical signals, while, for sCT, X-ray photons are directly converted into electrical signals. Therefore, sCT less suffers from noise. Second, by exploiting complementary information from different energy bins, the contrast of small objects is enhanced, making it easier to detect smaller objects with respect to conventional CT.

The simulations in the present study were based on ideal energy-integrating or photon-counting detectors (all the photons are concentrated in the centre of detectors) with Poisson noise added to the measurements. In practice, for physical photon-counting detectors, many factors such as cross-talk (caused mainly by Compton scattering and x-ray fluorescence effect) and pile-up (caused by photon count rate) will degrade their performance compared to the ideal photon-counting detectors. Likewise, for physical energy-integrating detectors that suffer from additional electronic noise, performance will also be degraded. The difference in performance between physical sCT (based on photon-counting detectors) and physical conventional CT (based on energy-integrating detectors) would be largely reduced compared to ideal situations where only Poisson noise is considered in ideal detectors.

3.5 Conclusion

We have investigated the potentialities of sCT with respect to conventional CT through simulations and physical validations. We demonstrated both qualitatively and quantitatively that owing to its multi-energy data characteristics, sCT can be used to achieve simultaneously anatomical and functional CT imaging with one single acquisition. When used as aCT, sCT allows obtaining conventional CT images as those generated by conventional CT, but with much better image quality. This is true for different configurations of imaging parameters such as projection views, current and voltage. Another advantage of sCT, and not among the least, is its higher quality than conventional CT under the same dose. Furthermore, sCT offers the possibility to enhance intrinsically anatomical images in aCT by making use of different images corresponding to different energy bins. The resulting images present substantially improved SNR and CNR. Meanwhile, when used as fCT, sCT enables us to get insights into the quantitative composition of materials in a pixel by means of appropriate material decomposition algorithms. For example, inside a pixel we can know what materials are present and what their concentration is. Such simultaneous multimodality

imaging ability of sCT with one single acquisition could change the way of using conventional CT and opens many new applications.

Chapter 4 Image reconstruction using multi-energy information in sCT

Abstract

sCT appears as a promising imaging technique for clinical applications thanks to its ability to offer better image quality and the possibility of quantitatively analyze the composition of materials in a pixel. However, due to the dispatching of photons into different energy bins, the quality of image at each energy bin is considerably degraded. In this chapter, we propose a reconstruction method for sCT images by combining multi-energy information. The method is based on clustering pixels containing similar material compositions, performing linear fitting within each class for all the energy images two-by-two, projecting the pixel values of the images at other energy bins to the pixel of the image at the current energy bin, and combining (median filtering) the original pixel value and projected pixel values. The results on both simulation and real data demonstrated the effectiveness of the proposed method, in terms of both image reconstruction quality and material decomposition accuracy.

4.1 Introduction

As the novel kind of CT, sCT gets more than two pairs of data in one scan due to the photon counting detectors, which have the ability to count the number of photons with different energies separately. Therefore, sCT can acquire at least two attenuation coefficient information of the object referred to different energy bins, and meanwhile the material composition, including the category and concentration (Schirra et al. 2014).

However, more energy bins also means smaller photon numbers within one bin, which will obviously decreased the image reconstruction quality. Therefore, various methods are developed for improving the reconstruction quality of CT images, including in the projection and image domain. In the projection domain, Hsieh developed an adaptive filtering according to the noise property to reduce the artifacts (Hsieh 1998); La Riviere proposed a penalized likelihood smoothing model on the sinogram (La Rivière 2005); Wang et al. presented a penalized weighted least-squares approach to reduce sinogram noise (Wang et al. 2006). However, because of the difficulty to accurately model the noise, some operations will bring in unexpected artifacts in the reconstruction, which could be avoided in the image domain. In image domain, iterative methods are still the most widely used in the reconstruction, which has developed from the original algebraic reconstruction technique (Gordon et al. 1970) to the methods with empirical knowledge. Various prior knowledge was implied for different practical applications, Gao proposed a compressive sensing approach which utilizes a prior rank, intensity and sparsity model (PRISM) for reconstruction (Manley 2013); Zhang developed a method with the sparsity and similarity in the sCT images for reconstruction (Zhang et al. 2016); Radiology proposed a constrained total nuclear variation method for joint reconstruction of multi-energy reconstruction (Rigie et al. 2015). No matter which prior knowledge is utilized for the reconstruction, it could improve the reconstruction quality in some applications.

With respect to existing methods, we propose to develop a reconstruction method by exploiting the intrinsic relation between the spatial images at different energy bins. The method is based on clustering pixels containing similar material compositions, performing linear fitting within each class for all the energy images two-by-two, projecting the pixel values of the images at other energy bins to the pixel of the image at the current energy bin, and combining (median filtering) the original pixel value and projected pixel values. The rest of the chapter is organized as follows. In section 4.2, the framework and details of the proposed method is introduced. In section 4.3, both simulation and real data are used to evaluate the performance of the proposed method. In sections 4.4 and 4.5, discussion and conclusion are given.

4.2 Method

4.2.1 Theory basis of the method

Denoising is a typical research problem in image processing, and there already exist many methods that allow us to obtain relatively satisfied results, such as BM3D (Block-

Matching and 3D filtering) (Lee and Song 2011), NLM (non-local means) (Buades et al. 2010), TV (total variation) (Chambolle and Lions 1997) and so on. These techniques were initially proposed for denoising natural images, which can of course work for conventional CT images. But, they do not account for intrinsic characteristics of sCT images. Therefore, we propose to introduce a new denoising mechanism in our image reconstruction by making use of the relationship between the spatial images at different energy bins.

In sCT, for the same pixel (position) in the reconstructed images at different energy bins, the relationship between the image pixel values is directly linked to material attenuation coefficients at these energy bins. Thus, information at different energy bins can be utilized to improve CT image reconstruction quality. In (Zhang et al. 2016), Zhang et al. found the mapping relationship between attenuation coefficients at different energy bins and introduced a piecewise fitting method for the regularization of their iterative reconstruction method. This fitting method combines the information among all the other energy bins to denoise and improve the quality of the current reconstructed image. This method utilizes two linear fittings to represent the relationship among energy bins and works only for materials without K-edge. For materials with K-edge, it does not work.

However, in medical diagnosis, Gd and I are usually utilized as contrast agent injected to the human body, which present K-edges within the photon energy range in sCT, as shown in Figure 4.1, where the mass attenuation coefficient curves of materials PMMA, water and Fe are also illustrated. PMMA and water do not have K-edge, but Fe has the K-edge energy less than 20 keV, the photons of which however are already filtered before reaching the scanned human body. In this situation, the method proposed in (Zhang et al. 2016) is not suitable for making use of information at different energy bins.

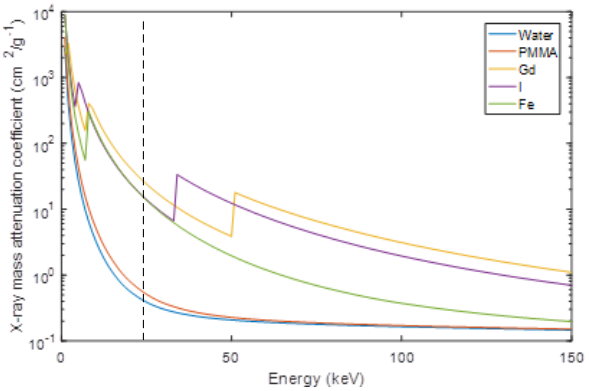

Figure 4.1 Mass attenuation coefficient for PMMA, Water, Gd, I, and Fe from 0 to 150 keV.

To cope with the above problem, we propose a new method that allows dealing with materials with K-edge. First, we explain the theory basis of linear fitting. The attenuation coefficient at a pixel can be represented as

$$\mu(\vec{x},E) = f_p(\vec{x})g_p(E) + f_c(\vec{x})g_c(E) + \sum_{\alpha=1}^{N}\mu_{m\alpha}(E)\rho_\alpha(\vec{x}) \quad , \tag{4.1}$$

where $g_p(E)$ and $g_c(E)$ are the Photoelectric absorption and Compton effect, $f_p(\vec{x})$ and $f_e(\vec{x})$ are the constants which are decided by the materials in pixel $\vec{x}$, N is the number of K-edge materials in in pixel $\vec{x}$, $\mu_{m\alpha}(E)$ is the mass attenuation coefficient of K-edge material α at energy E and $\rho_\alpha(\vec{x})$ is the corresponding density. Equation (4.1) is represented by two parts,

$$\mu(\vec{x},E)=\mu_{No}(\vec{x},E)+\mu_{K-edge}(\vec{x},E) \quad , \tag{4.2}$$

where $\mu_{K-edge}(\vec{x},E)$ denotes the K-edge effect, and $\mu_{No}(\vec{x},E)$ the photoelectric absorption and Compton effects. According to the work in (Zhang et al. 2016), any material can be represented as a linear combination of two base materials (water and bone), namely

$$\mu_{No}^{\zeta}(\vec{x},E)=a_1\mu_{No}^{Water}(\vec{x},E)+a_2\mu_{No}^{Bone}(\vec{x},E) \quad , \tag{4.3}$$

where a_1 and a_2 are the material dependent constants. As a result, Equation (4.1) is written as

$$\mu(\vec{x},E)=a_1\mu_{No}^{Water}(\vec{x},E)+a_2\mu_{No}^{Bone}(\vec{x},E)+\sum_{\alpha=1}^{N}\mu_{m\alpha}(E)\rho_\alpha(\vec{x}), \tag{4.4}$$

Also, the research points out that the materials without K-edge inside human body are classified into Water-like material ($a_1\approx 1, a_2\approx 0$) and Bone-like material ($a_1\approx 0, a_2\approx 1$). Thus, the Equation (4.4) degraded to

$$\mu(\vec{x},E)=\mu_{No}^{Water}(\vec{x},E)+\sum_{\alpha=1}^{N}\mu_{m\alpha}(E)\rho_\alpha(\vec{x}), \tag{4.5}$$

or

$$\mu(\vec{x},E)=\mu_{No}^{Bone}(\vec{x},E)+\sum_{\alpha=1}^{N}\mu_{m\alpha}(E)\rho_\alpha(\vec{x}), \tag{4.6}$$

For a given pixel, $\vec{x}$ is known and Equation (4.5) becomes

$$\mu(E)=\mu_{No}^{Water}(E)+\sum_{\alpha=1}^{N}\mu_{m\alpha}(E)\rho_\alpha , \tag{4.7}$$

Thus, if a pixel only contains one material with K-edge, which is the most common case in medical diagnosis, the attenuation coefficient is actually the linear function of concentration within each energy bin. For one pixel of all the energy bins, as the concentration ρ_α is fixed and the attenuation of Water has slightly changes which can be regarded as a constant, it is also a linear function.

In the present study, we focus on the improvement of reconstruction quality of sCT images with K-edge. First, the simulation data is utilized because the ground-truth of attenuation coefficients is known. The simulation phantom described in Chapter 3 is employed for analyzing the attenuation coefficient relationship among the energy bins. It contains different concentrations of materials with K-edge (Gd and I): 5mg/cc, 15mg/cc, 25mg/cc, 35mg/cc, and 45mg/cc. The concentrations of the material without K-edge (Fe) are 50mg/cc, 100mg/cc, 150 mg/cc, 200mg/cc, and 250mg/cc. The mixtures are made of Gd, I and Fe with the same concentrations as above.

Figure 4.2 illustrates the relationship between two attenuation coefficient sets corresponding to two energy bins for different materials and different densities. The

points having the same color represent the same material composition in a pixel. The points in the same color represent the same material composition in a pixel. X axis is the attenuation coefficients of the points for energy bin 30-39 keV, and y axis is the attenuation coefficient for energy bin 40-49 keV (or 70-79 keV). Although they are with different concentrations, which means different attenuation coefficients within one energy bin, the points in the same color can be fitted as a straight line, as obvious for Gd (the points in blue), I (the points in orange) and Fe (the points in yellow). For mixtures (the points in purple) with material Gd, I and Fe, they are not but near a straight line, which is due to the different K-edge energies. The case where we have the same material composition but with different densities is illustrated in Figure 4.3 (for the energy bin 30-39 keV). The points having the same color are from the same energy bin. Different fitting lines represent different pairs of energy bins. We observe that for the same composition of materials, the relationship between two attenuation coefficient sets corresponding to two energy bins can be fitted by a linear function. Also, each energy-bin pair has their specific fitting coefficients. Hence, if pixels having similar compositions are clustered and the fitting coefficients are estimated, the spatial image at one energy bin can be projected to any other energy bin.

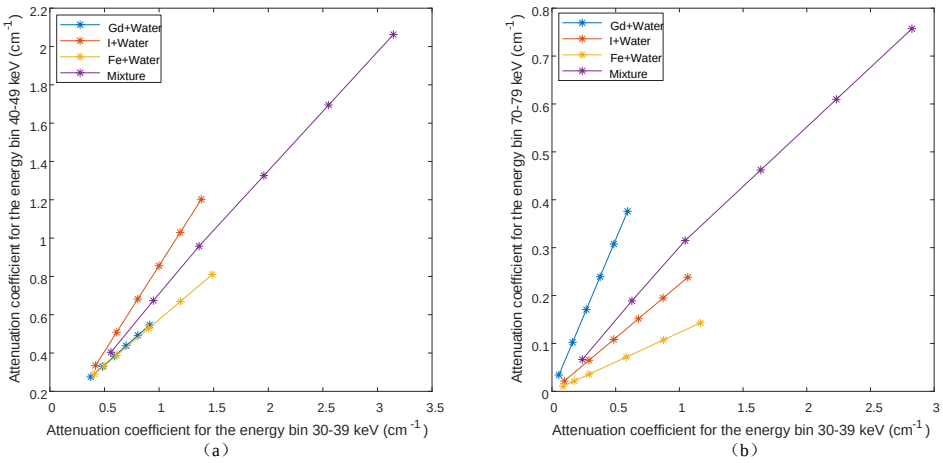

Figure 4.2 Attenuation coefficient relationship between two energy bins for different materials: (a) between energy bins 40-49 keV and 30-39 keV; (b) between energy bins 70-79 keV and 30-39 keV. The 6 points on each line represent the 6 concentrations of the same material.

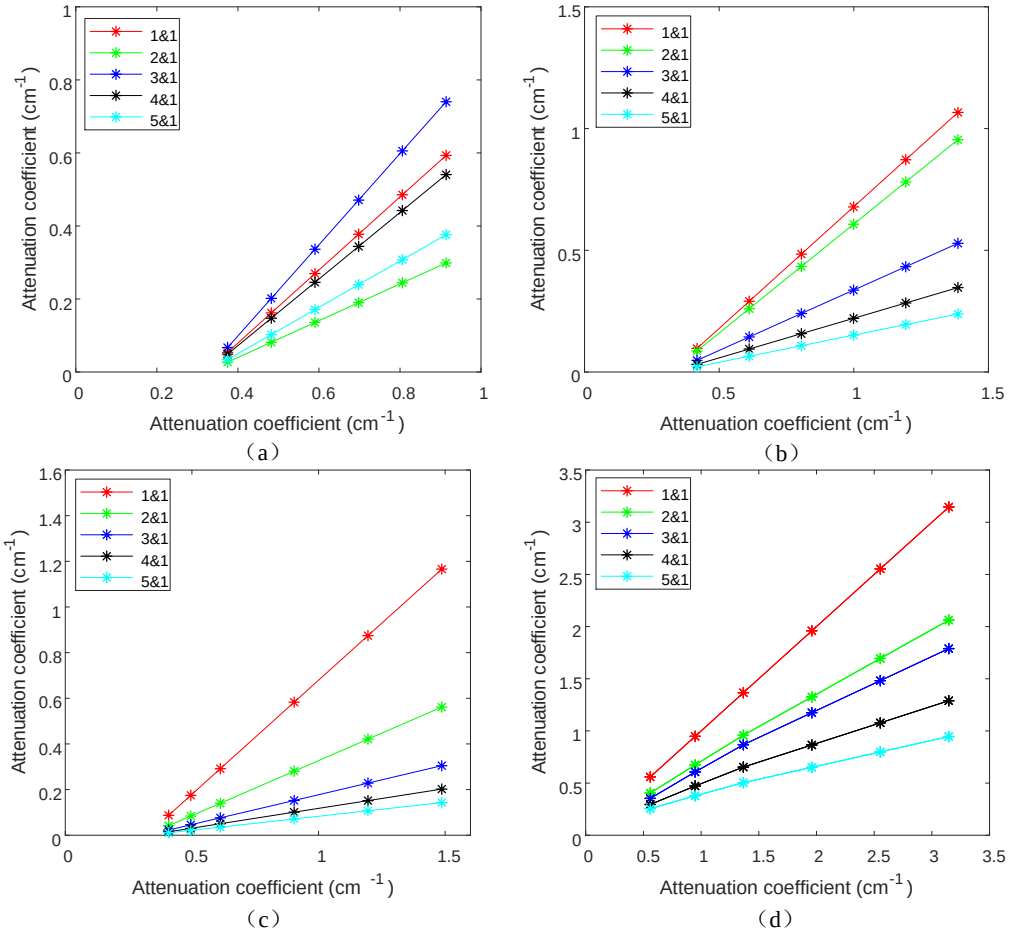

Figure 4.3 Attenuation coefficient relationship between energy bin 1 (horizontal axis, 30-39keV) and the other energy bins (vertical axis) for different materials. (a) Gd+Water; (b) I+Water; (c) Fe+Water; (d) Mixture, and 1: 30-39 keV; 2: 40-49 keV; 3: 50-59 keV; 4: 60-69 keV; 5:70-79 keV. The 6 points on each line represent the 6 concentrations of the same material.

The framework of our method is illustrated in Figure 4.4. First, primary reconstruction at each energy bin is achieved using basic reconstruction methods (FBP for simulation and SART for physical CT in our thesis). The next step is to find the image pixels that have similar values and label them as the same class. To do this, commonly used k-means algorithm is adapted. Then, linear fitting is made for all the image pixels of any two energy bins within each class separately, thus yielding the fitting coefficients for any two energy bins for each class. By using such image value fitting two-by-two, an image pixel value at one energy bin can be estimated from the image pixel values at all the other energy bins. That is, for a sCT system producing five images corresponding to five energy bins, a pixel will have five attenuation coefficients (i.e. pixel values): the current (original) image value and the other four image values mapped (estimated) from the other four energy bins. Finally, a filter is applied to the five values to obtain a single value that presents reduced noise, thus improving the quality of the reconstructed image. In the next paragraphs, the main elements of the framework will be presented in detail.

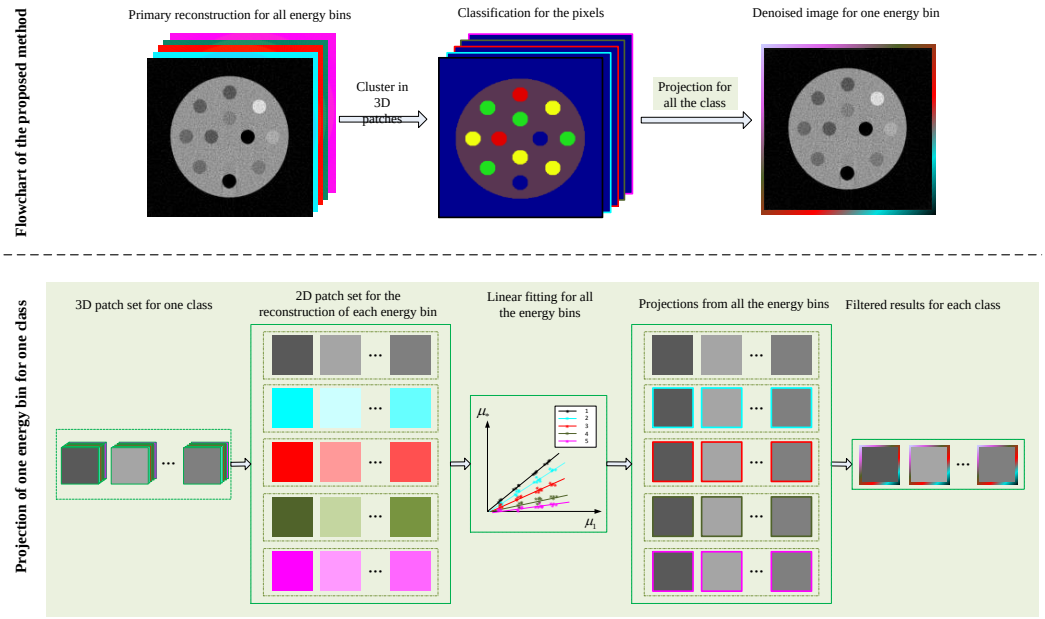

Figure 4.4 Flowchart of the proposed method by one energy bin mapping operation.

4.2.2 Material-dependent clustering

As linear relationship exists between pixels having similar composition and different material compositions obey different fitting, the first step is to classify the pixels in the reconstructed image. The classification is operated on the 3D image, which is formed by stacking the 2D images at different energy bins. The classification is done pixel by pixel. However, in view of the influence of noise and spatial correlation between pixels, we will perform the classification patch by patch. To this end, 2D patch in primary reconstructed images at all bins are arranged to form a set of 3D image cube, namely, 3D patch, the third dimension of which represents energy dimension. Denoting the primary reconstruction image as

$$U=\left[\mu(1);\mu(2);...;\mu(k);...\mu(K);\right], \tag{4.8}$$

where K is the total number of energy bins, and $\mu(k)$ is the reconstructed image for the kth energy bin, which is reshaped as

$$\mu(k)=\begin{bmatrix}\mu_{11}(k) & \cdots & \mu_{1N_I}(k)\\ \vdots & \ddots & \vdots\\ \mu_{N_I1}(k) & \cdots & \mu_{N_IN_I}(k)\end{bmatrix}, k=1,2,...,K \quad , \tag{4.9}$$

where $N_I \times N_I$ is the image size. Then the cluster unit X is represented by

$$X_{ij}=\left[x_{ij}(1);x_{ij}(2);...;x_{ij}(K);\right] \quad , \tag{4.10}$$

$$x_{ij}(k)=\begin{bmatrix}\mu_{\left(i-\frac{P+1}{2}\right)\left(j-\frac{P+1}{2}\right)}(k) & \cdots & \mu_{\left(i-\frac{P+1}{2}\right)\left(j+\frac{P-1}{2}\right)}(k)\\ \vdots & \mu_{ij}(k) & \vdots\\ \mu_{\left(i+\frac{P-1}{2}\right)\left(j-\frac{P+1}{2}\right)}(k) & \cdots & \mu_{\left(i+\frac{P-1}{2}\right)\left(j+\frac{P-1}{2}\right)}(k)\end{bmatrix}, k=1,2,...,K, \mu_{ij}(k)\in\mu(k), \tag{4.11}$$

where $x_{ij}(k)$ is the 2D patch in the energy bin k centred at the position (i,j), $\mu_{ij}(k)$ is the primary reconstruction in the k th energy bin at the position (i,j), X_{ij} denotes the

3D patch to be clustered centered at the position (i, j), $P \times P$ is the 2D patch size for one energy bin, of which P is usually selected as an odd number. Thus, each 3D patch is with the size of $P \times P \times K$.

The key will be to extract the features of 3D patches for clustering. To do this, the following factors are to be taken into account.

For a given reconstructed spatial image, most of its pixels contain water. Thus, water can be considered as a constant and will be first removed from the spatial image at each energy bin. The processed cluster unit can then be expressed as

$$x_{ij}^{'}(k) = x_{ij}(k) - x_{water}(k), k = 1,2,...,K \,, \tag{4.12}$$

$$X_{ij}^{'} = \left[x_{ij}^{'}(1); x_{ij}^{'}(2); ...; x_{ij}^{'}(K); \right]. \tag{4.13}$$

1) For different patches, the parameters such as mean, first-order differential and second-order differential of attenuation coefficients and its mean, these parameters are combined into a vector as the feature for classification.

$$V_{ij} = \left[\overline{X_{ij}^{'}}; \nabla X_{ij}^{'}; \overline{\nabla X_{ij}^{'}}; \nabla^2 X_{ij}^{'}; \overline{\nabla^2 X_{ij}^{'}} \right], \tag{4.14}$$

where $\overline{X_{ij}^{'}}$ ($\overline{\nabla X_{ij}^{'}}$ or $\overline{\nabla^2 X_{ij}^{'}}$) is the mean of $X_{ij}^{'}$ ($\nabla X_{ij}^{'}$ or $\nabla^2 X_{ij}^{'}$), $\nabla X_{ij}^{'}$ and $\nabla^2 X_{ij}^{'}$ are the first-order and second-order differential for $\overline{X_{ij}^{'}}$, respectively.

2) K-means algorithm is chosen to cluster the features for its fast speed. The number of classes is the most important parameter for k-means: if the number is set too small, different materials will be classified into the same class, thus resulting in the inaccurate fitting in the next step; on the contrary, if the number is set too large, thus for each class, the number of patches will be small, the same class would be possibly regarded as different classes, which will decrease the amount of data and is not beneficial to fitting. In other words, setting the number of classes too small will make the patch mistakenly classified, and setting it too large will reduce the number of patches in each class. Relatively speaking, the influence of the class number on the precision is acceptable when it is set larger compared with that smaller. To get a reliable fitting, in our experiment, it is set as twice as the number of the material composition.

   Meanwhile, k-means algorithm is sensitive to the selection of the initial points. If one patch is clustered to the wrong class, it will reduce the accuracy of the fitting results. Thus, to overcome this problem, the k-means algorithm is is revised in our problem and the following operation is made in our method. In the process of cluster, several k-means with random initials are made on the 3D patches. If the patches in two continuous operations are clustered to the same class, they will be regarded as the reliable patches and the class label is kept for further fitting; otherwise, they will be regarded as the sensitive ones, and will not be fitting in the next steps.

4.2.3 Linear fitting between bins

For the patches in the same class, fitting is made between each two energy bins. Let $\{V_{m1}, V_{m2}, ..., V_{mN_m}\}$ be the patches of class m, where N_m is the patch number for class m,

$m=1,2,...,M$, and M is the total class number. Considering that one point is often polluted by the noise, if fitting is made point by point, it is more likely to be affected by the noise. Therefore, the $P\times P$ points in the 2D patch in each bin is utilized for fitting. Meanwhile, to keep the edges of the image, the weighted mean of the points in each bin is utilized for fitting, of which the weight is defined as

$$W=\frac{1}{P^D} \ , \tag{4.15}$$

where D is the city distance from the neighbor position to the central pixel within the 2D patch. In our method, least square errors method (LSE) is adopted to make the fitting between every two bins. As a result, for each class, $K\times K$ group fitting coefficients will be generated, which will be utilized for further mapping.

The fitting results from bin p to bin q is calculated by

$$\mu_{ij}^{p}(q)=a_{pq}(m)\bar{\mu}_{ij}(p)+b_{pq}(m), m=1,2,...,M, p,q\in 1,2,...,K, if\ \mu_{ij}\in m \ , \tag{4.16}$$

where $\mu_{ij}^{p}(q)$ donates the fitting attenuation coefficient for the bin p to the energy bin q, $\bar{\mu}_{ij}(p)$ is the weighted average within the 2D patch for the energy bin p, $a_{pq}(m)$ and $b_{pq}(m)$ designate the fitting coefficients for the mth class. Thus, after traversing all the patches in the M class, for all the positions in each energy bin, $K-1$ fitting results will be obtained from the other bins. If accounting the bin itself, K reconstruction will be utilized for next operation (post-denoising).

4.2.4 Reconstruction denoising via fitting results

After the fittings, we obtain K reconstructed images corresponding to the K energy bins. The next step is to improve the current reconstructed image by making use of the fitting results (i.e. the *K*-1 images generated from the fittings). The first idea would be to average the K images to reduce noise that is the principal problem in sCT. To this end, weighted averaging is adopted because it has the advantage of producing stable denoising results. However, considering the characteristic of the data acquired from each energy bin, targeted filter is selected to get better performance for denoising. If the position of the reconstructed image at one energy bin suffers from noise, the fitting result from this bin to all the remaining bins will also be noised because the fitting involves all the energy bins. Thus, based on the fact that reconstruction noise at each energy bin is independent from each other, for a given position, both the current reconstructed image and all the fitted images are taken into account for the image averaging. In the present study, we choose median filter to achieve denoising. It can be expressed as

$$\tilde{\mu}_{ij}(q)=Med\left\{\mu_{ij}^{1}(q),\mu_{ij}^{2}(q),...,\mu_{ij}^{K}(q)\right\}, q=1,2,...,K \ , \tag{4.17}$$

Actually, with respect to the original reconstructed image, fitting results that are too far away from the original image are regarded as unreliable. Such situation may be caused by the mixtures or wrong clustering. Therefore, to keep the reliability of the final results, if relative errors between the fitted values and original values are larger

than a threshold, the fitted values will be abandoned and the corresponding pixels will keep the original values, namely

$$\tilde{\mu}_{ij}^{'}(q)=\begin{cases}\tilde{\mu}_{ij}(q) & if \quad \left|\tilde{\mu}_{ij}(q)-\mu_{ij}(q)\right|/\left|\mu_{ij}(q)\right| < threshold \\ \mu_{ij}(q) & if \quad \left|\tilde{\mu}_{ij}(q)-\mu_{ij}(q)\right|/\left|\mu_{ij}(q)\right| \geq threshold\end{cases}. \qquad (4.18)$$

Therefore, the operation is performed after the median fitting to revise the final results.

4.3 Results

4.3.1 Simulation

4.3.1.1 Phantom and evaluation metrics

The projection data of sCT was simulated using INSA software Virtual X-ray Imaging (VXI) (Duvauchelle et al. 2000). A sCT system consisted of a PCD with 700 pixels arranged in line. The spectrum was simulated based on Birch & Marshall model for tungsten target material without filtration; the target angle was 17°, with tube voltage of 100kVp, tube current 100 μA and spectrum resolution 1 keV. The detector has energy-resolving ability 5 energy bins. The energy bin ranges are 30-39, 40-49, 50-59, 60-69 and 70-79 keV. In our experiment, the phantom was scanned with 600 projection views from 0° to 360° of equal interval, and the reconstruction image size is 380×380. The parameters in the method are set: the 3D patch size as $3\times3\times5$, and the revised threshold as 0.3.

The simulation phantom was designed to be the same as the physical phantom shown in Figure 3.8. It is a big cylinder made up of PMMA with the radius of 130 mm, which was digged out 12 holes to fill up the materials water, gadolinium (Gd) and iodine (I). For Gd, the concentrations were separately set as 2, 4, 6, 8 mg/cc, and for I as 1, 3.5, 7 and 14 mg/cc. The 12 holes are regarded as the regions of interest (ROIs), and the evaluations are made for the ROIs. To validate the performance of the algorithm, simulation and both real data are utilized.

Reconstruction and decomposition metrics are both calculated to evaluate the performance of the algorithm. For reconstruction in simulation, root mean square errors (RMSE), contrast to noise ratio (CNR) and signal-to-noise ratio (SNR) of the 12 ROIs are utilized, which has already been defined in Chapter 3. While for the physical phantom, considering that there is no ground-truth, CNR is utilized for the evaluation. For the real data, including the physical phantom and the rabbit, the reconstructions and monochromic energy (monoE) of the K-edge are also visually displayed for comparison.

The material decomposition results are acquired by the L1-norm method with the same parameters. For the decomposition results, the results are first compared with the ground-truth visually in the material decomposition image. In addition, the values within the ROIs are fitting by their mean value, and the standard deviations are compared with the ground-truth.

4.3.1.2 Reconstruction comparison

Figure 4.5(a) illustrates the original reconstruction by FBP for five energy bins and the fitting results from the four bins to the energy bin 70-79 keV. Figure 4.5(b) shows the final reconstruction with the results from Figure 4.5(a), and also the ground-truth, the reconstruction from FBP, TV, for the energy bin of 70-79 keV. It can be observed that the results of our method stay the same level as that of the ground-truth, and that the restored information is close to the background.

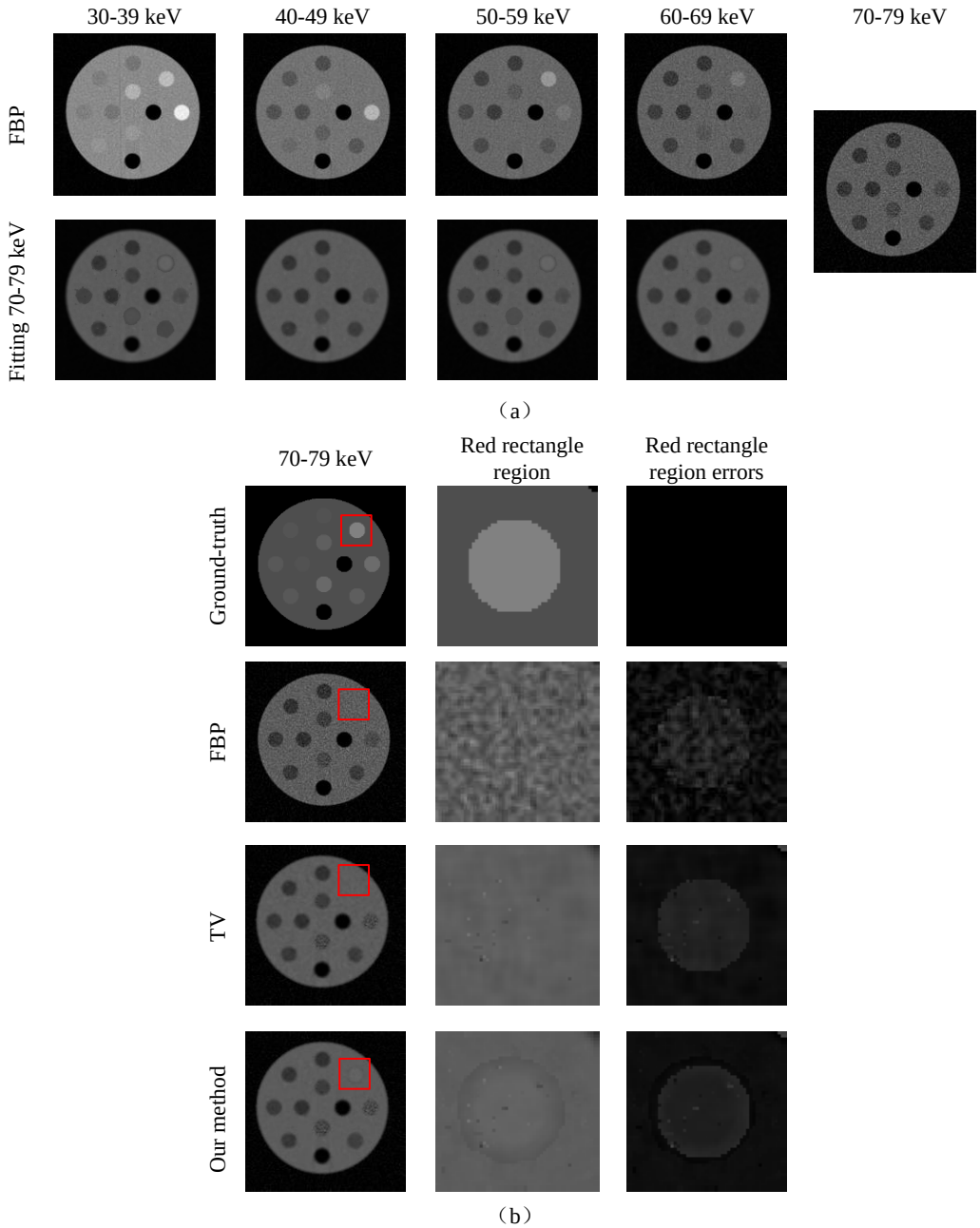

Figure 4.5 Denoised reconstruction for bin of energy 70-79 keV.

Table 4.1 gives the RMSEs and SNRs of the original image and our fitted image. It is observed that our method has the smallest RMSE and the largest SNR. For the method SART_TV, the reconstruction shows the smoothest outline, however the values

of the reconstructed image have been altered due to the TV item, which results in large RMSE and small SNR. Compared to FBP, the improvement in RMSE for different energy bins is respectively 1.53%, 6.00%, 4.50%, 9.07%, 14.36%, and the improvement in SNR is respectively 1.01%, 4.38%, 3.48%, 7.18%, 12.34% . Thus, it can be concluded that the proposed fitting method improves RMSEs and SNRs for all the energy bins. Concerning CNR, our method shows better performance compared to FBP, but does not do as good as TV. This is due to the fact that the phantom is made up of isotropic and average distribution in the ROIs, and TV has better ability to smooth the region, but meanwhile at the risk of altering the values of the reconstruction, which will have great effect on the subsequent material decomposition.

Table 4.1 Comparison of results on RMSEs, SNRs and CNRs.

		30-39keV	40-49keV	50-59keV	60-69keV	70-79keV
RMSE	FBP	0.046	0.042	0.040	0.040	0.041
	TV	0.082	0.068	0.062	0.057	0.054
	Our method	0.045	0.039	0.038	0.036	0.035
	Improvement to FBP	1.53%	6.00%	4.50%	9.07%	14.36%
SNR	FBP	13.685	12.644	12.073	11.365	10.389
	TV	6.149	5.985	5.8341	5.852	5.866
	Our method	13.823	13.198	12.493	12.181	11.67
	Improvement to FBP	1.01%	4.38%	3.48%	7.18%	12.34%
CNR	FBP	1.194	1.259	1.332	1.257	1.216
	TV	1.255	1.400	1.491	1.465	1.500
	Our method	1.227	1.298	1.352	1.346	1.349
	Improvement to FBP	2.76%	3.04%	1.51%	7.03%	10.94%

4.3.1.3 Decomposition comparison

As functional CT is one of the most applications for sCT, the decomposition results are compared based on the reconstruction images. L1-norm method is utilized to decompose the reconstruction into Water, PMMA, I and Gd, as shown in Figure 4.6. It is observed visually that decomposition results from our fitting methods contain less noise and are closer to the ground-truth.

What's more, the fitting line is utilized to evaluate the performances of material decomposition, as shown in Figure 4.7. It is observed that although our method is not as smooth as the results of TV, the line of the fitting results is closer to the ground-truth compared to the other methods.

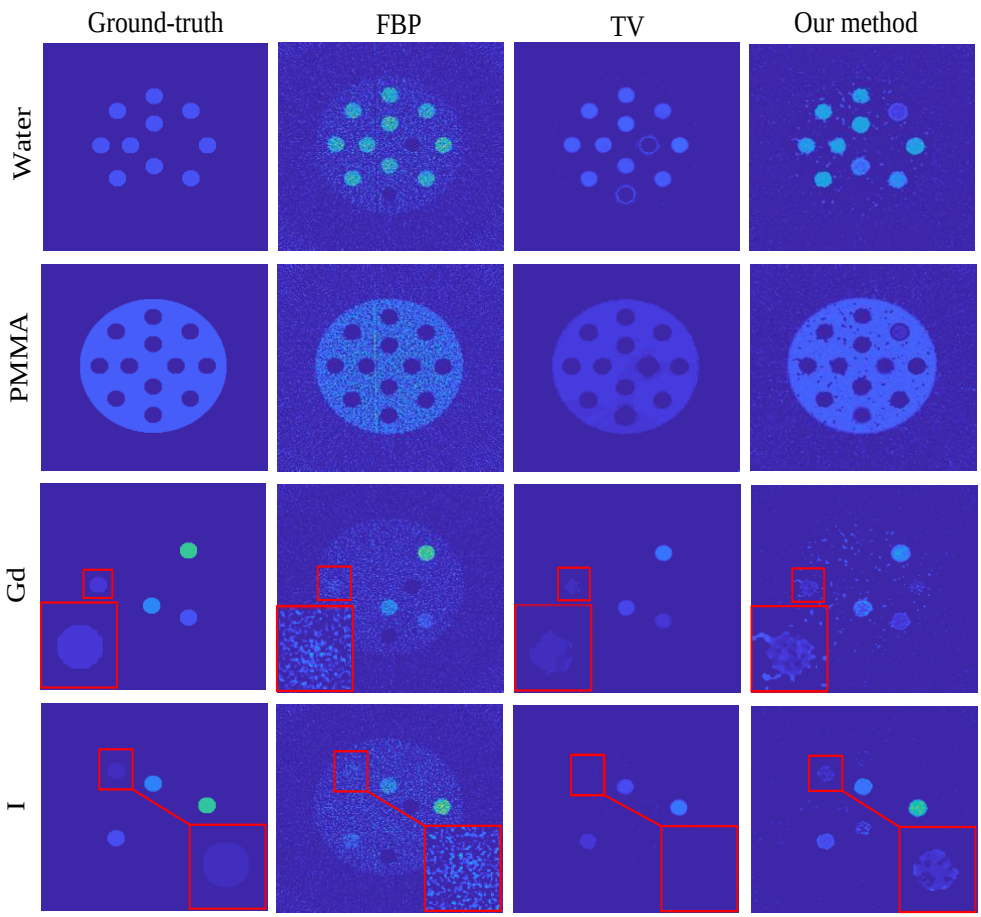

Figure 4.6 Decomposition comparison of the original reconstruction and denoised reconstruction.

4.3.2 Real data

4.3.2.1 Physical phantom

Two physical phantoms (shown in Figure 4.8) respectively filled with Gd (or I) and water were utilized to demonstrate the performance of our method. The phantom is made of PMMA with the diameter of 100mm. The concentration for Gd is set from 0.1 mg/cc to 15 mg/cc, and that for I is from 0.1 mg/cc to 15 mg/cc, as marked by the number in each disk. The phantom was scanned by IQON sCT with the source current as 220 mA, source voltage as 120 keV and projection views as 2400, which is averagely distributed in the 360^0 . The sCT system contains 924 detectors, each of which contains 5 energy bins, with the thresholds as 30, 51, 62, 72 and 81 keV. The performance is evaluated in terms of both image reconstruction and material decomposition.

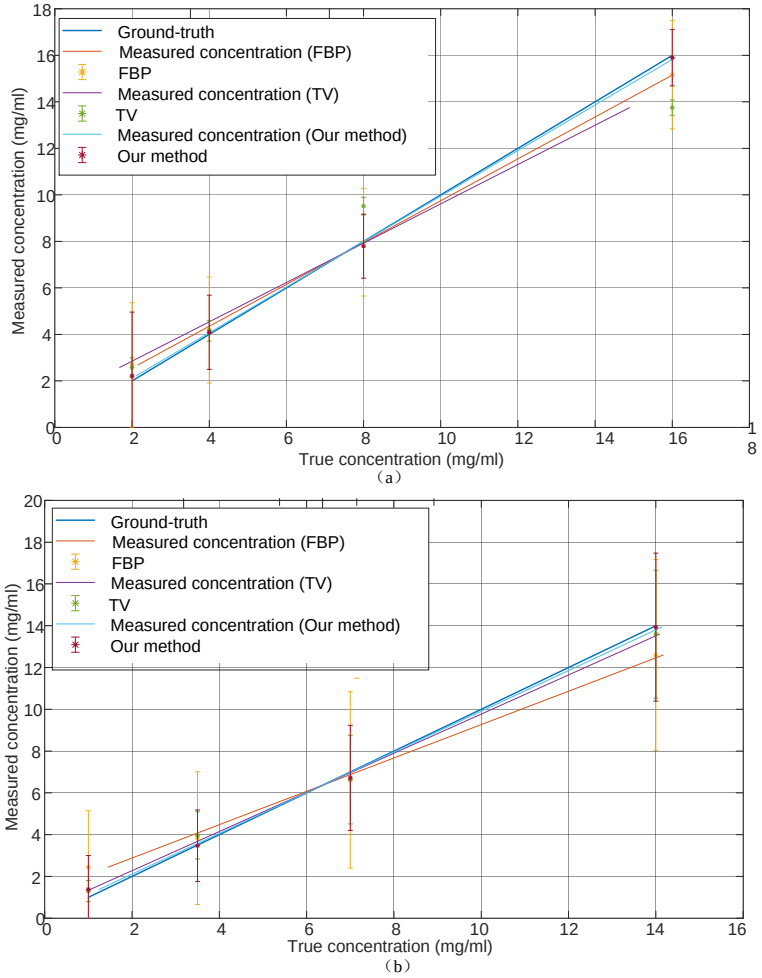

Figure 4.7 Decomposition results evaluation of FBP, TV and our method. (a) Gd; (b) I.

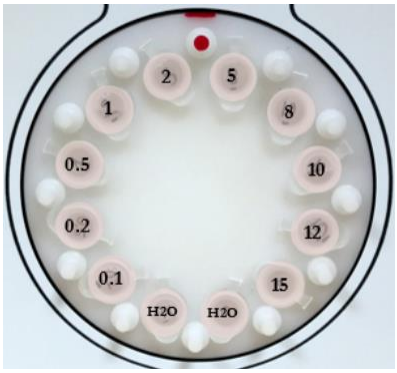

Phantom with water and I

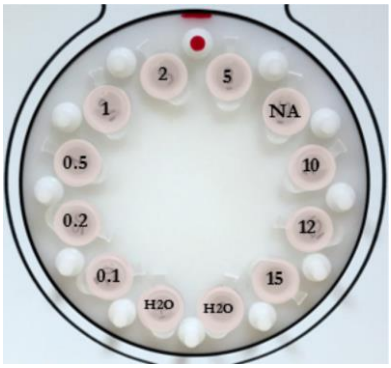

Phantom with water and Gd

Figure 4.8 Physical phantom.

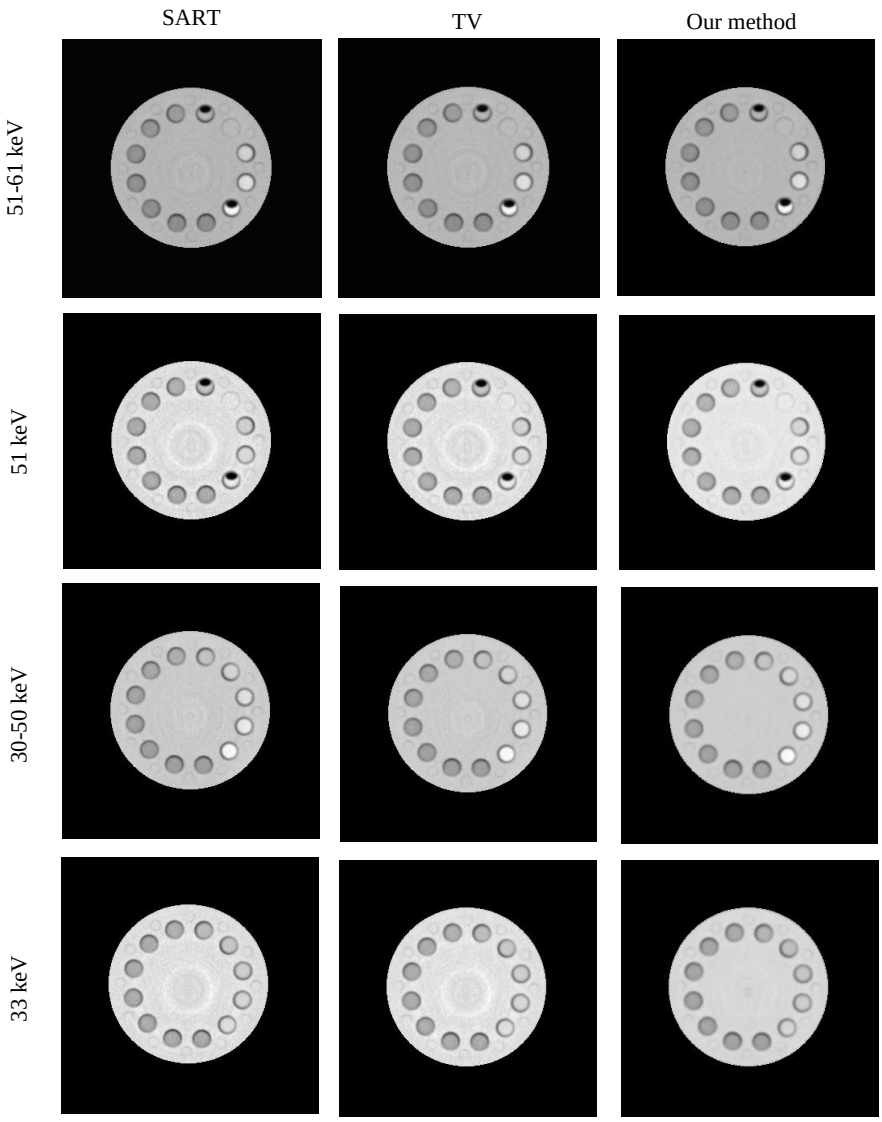

Figure 4.9 Reconstruction for the energy bin with K-edge and monoE reconstruction of the K-edge for Gd, I, respectively.

Figure 4.9 shows the reconstruction of each energy bin by SART, TV and our method. The first two rows show the results of the phantom with Gd and the last two rows displays the reconstruction of the phantom with I, for the bin with K-edge energy and the monoE reconstruction of K-edge. It is observed that after utilizing the information from other energy bins, the artifacts of the reconstruction for each energy bin are visually reduced.

As there lacks the ground-truth for physical data, the CNRs for the ROIs are calculated to make a comparison, as show in Table 4.2. It is observed that our method improves the CNR for the ROIs compared with SART, and most of the time shows better performance with TV.

Table 4.2 Reconstruction comparison on CNRs.

		30-50 keV	51-61 keV	62-71 keV	72-80 keV	81-150 keV
Gd+Water	SART	1.088	1.273	1.128	0.973	0.912
	TV	1.118	1.307	1.157	1.003	0.919
	Our method	1.125	1.303	1.167	1.017	0.956
	Improvement to SART	3.40%	2.40%	3.44%	4.53%	4.77%
I+Water	SART	1.500	1.370	1.229	1.223	1.307
	TV	1.548	1.387	1.282	1.293	1.374
	Our method	1.551	1.432	1.283	1.296	1.422
	Improvement to SART	3.44%	4.49%	4.32%	5.97%	8.80%

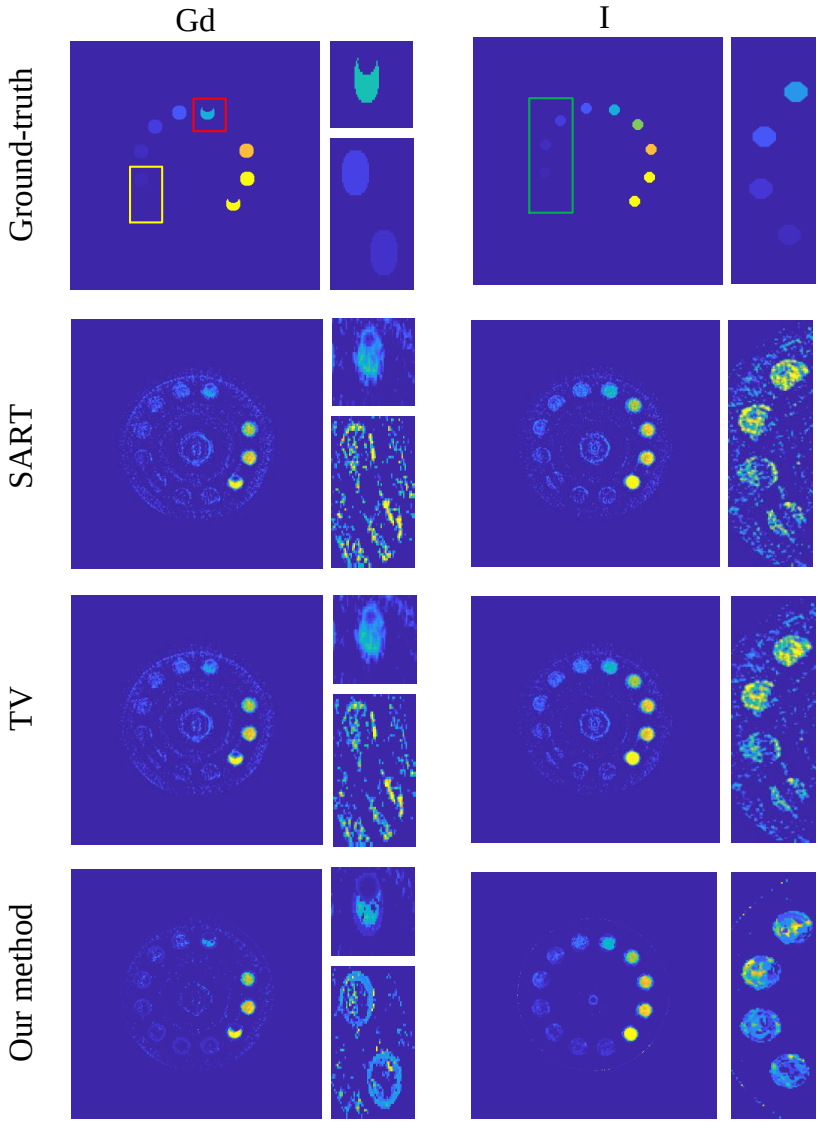

Figure 4.10 Decomposition results for physical phantom with Gd and I, respectively. The right column for each image is the region with low concentrations (yellow and green rectangle) and of special shape (the red rectangle) in the blown-up form. The images for the same region for all the methods are displayed in the same scale.

Figure 4.10 displays the ground-truth of the physical phantom and the material decomposition results by SART, TV and our results. Meanwhile, the ROIs with low

concentrations (yellow and green rectangle) and of special shape (red rectangle) are zoomed up. The display window is normalized for the same region. We observe that our method is more effective both for the ROIs of low concentrations and for the ROIs of special shape. It distinguishes more pixels of low concentration and supplies more information. For other non-ROI regions, our method also reduces more artifacts.

Also, the material concentration and standard error for each ROI are given in Figure 4.11. The axis is the logarithm of the concentration, as the concentration of materials in the phantom has mainly low values, which makes it difficult to distinguish in practice. The ground-truth is a line passing through the origin of coordinate system. As observed, the results of our methods are most of the time the nearest to the ground-truth, and have the smallest standard errors. Also, the fitting line of our method shows the best performance compared with the other two methods.

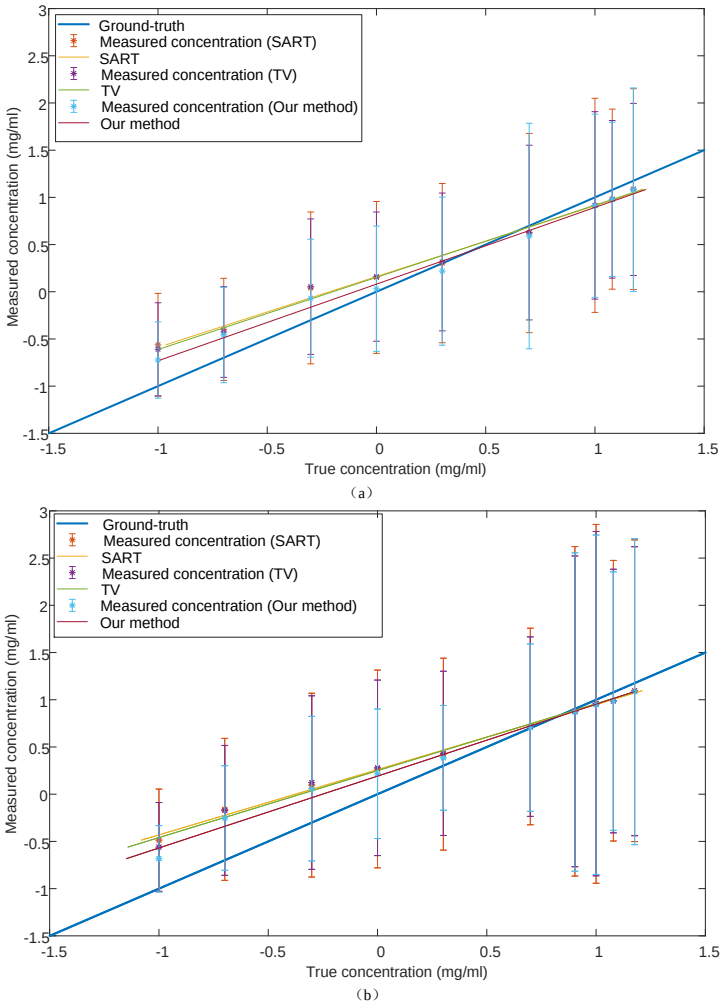

Figure 4.11 Decomposition value comparison: the axis is the logarithm of the concentration; each star represents the mean value within the ROI and the line segment through each star is the responding absolute standard error. (a) Gd; (b) I.

4.3.2.2 On rabbit

The rabbit injected with Gd was fixed in the container to be scanned by the physical CT. The system parameters of sCT are set the same as that for the physical phantom described in 4.3.2.1. Figure 4.12 shows the reconstructions from the sinograms of 30-50 keV that contains the K-edge energy of I and those of 51-61 keV that contains the K-edge energy of Gd. For the reconstruction at one energy bin, it is not easy to observe the difference since the width of the energy bin is too large. In contrast, in the monoE reconstruction, it is clearly observed that the reconstructions with our method reduce artifacts compared with the other two methods.

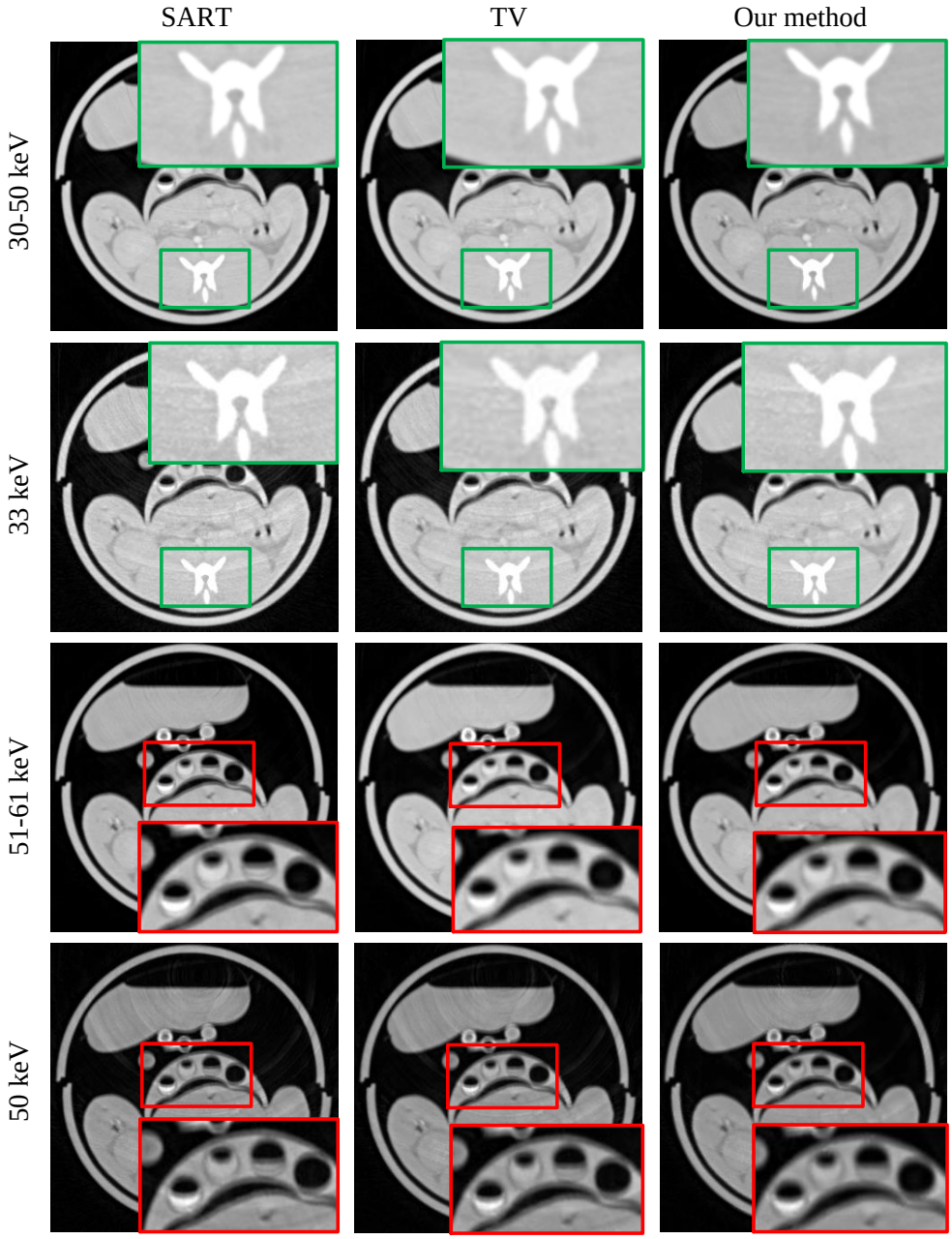

Figure 4.12 Reconstruction for the rabbit for energy bin with K-edge and monoE reconstruction for K-edge, respectively.

Now, we decompose the images into water, Gd and I. Thus, water-like material (such as plastic) will be decomposed into water, and I-like material will be into I (such as the bone whose main material is Ca). What's more, four tubes filled with Gd with concentrations of 10, 5, 2 and 0 mg/cc (the rectangle in Figure 4.13) are fixed into the container and scanned together with the rabbit to act as a reference. It is observed that our method suffers fewer artifacts compared to the other two methods, especially in the material I (the second row).

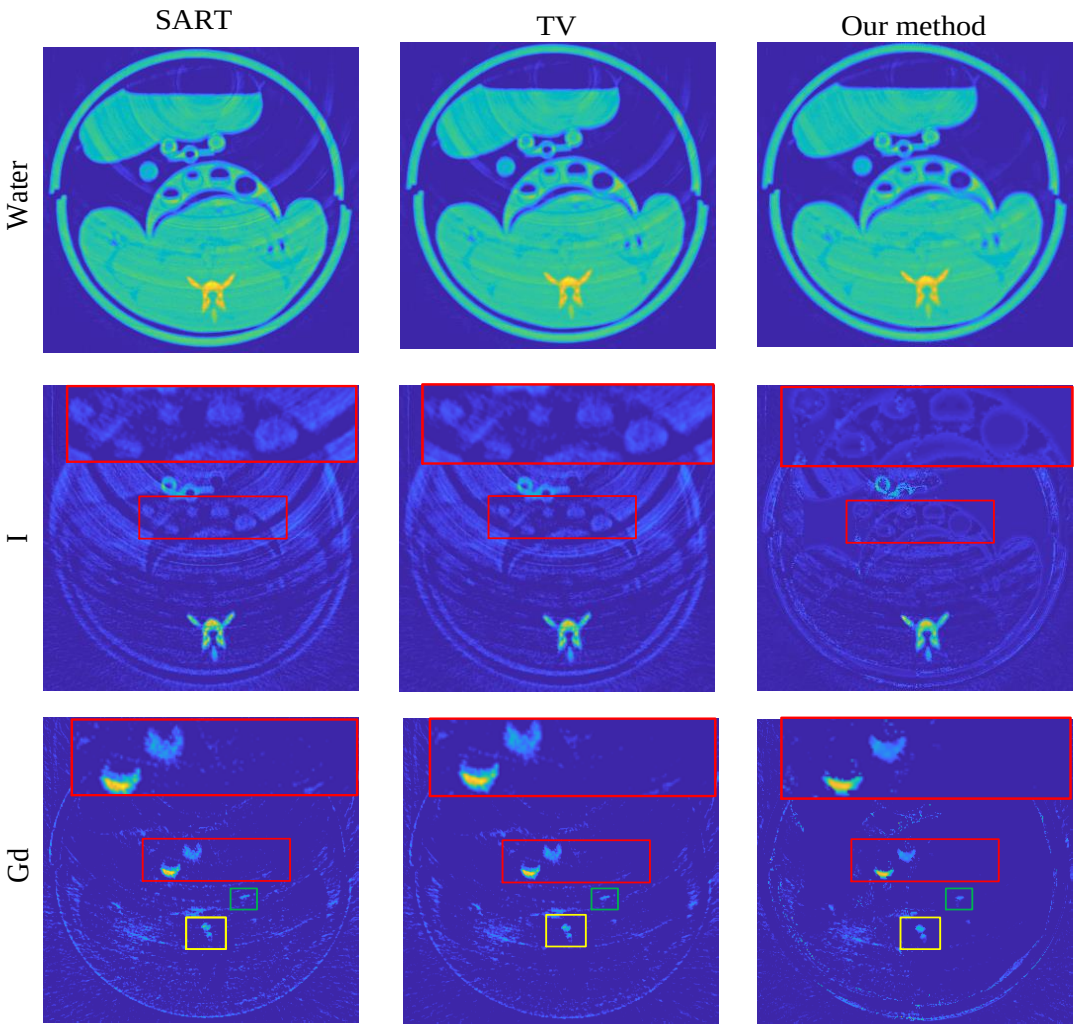

Figure 4.13 Decomposition results of the rabbit injected by Gd.

4.4 Discussion

We have proposed a reconstruction method for sCT images by combining multi-energy information. Based on the similarity of object composition, material-like pixels are clustered into the same class for fitting. The fitted images at other energy bins are then filtered (median filtering) to obtain the final reconstructed image at the current energy bin, which enables the reconstruction and decomposition more accurate.

The results on both simulation and real data showed that our method works well not only for reconstruction but also for material decomposition. In the simulation, our method operated on the primary results obtained using FBP. The results are not as

smooth as the TV method. This is due to the fact that our method does not smooth neighboring pixels. Nevertheless, the results of our method are closer to the ground-truth because our method revises pixel values at each energy bin through fitting mechanism. This improves reconstruction and material decomposition on real data that contains more complex noise and artifacts. It can be clearly observed that our method eliminates artifacts, both in the case of physical phantom and in the case of rabbit.

The performance of our method is also significantly affected by the cluster results of the pixels with the reconstruction. As the linear relationship of the attenuation coefficients for each energy bin exists in the pixels with similar material composition, the correct classification for each pixel is a fatal procedure in the method. Thus, the feature selection for each pixel is a key consideration in the method, of which the features reflecting the characteristic of each class will be the aim.

The process of the fitting results is another important process in the method. Due to its performance in pepper and salt noise and the fact that the reconstruction noise for each pixel is hard to model, the median filter is adapted to select the final value from all the fitting values from all the energy bins. Also, other filter could also be explored for this step, such as weighted average. Weighted average is also tried, which will also improve the performance but most of the time does not function as well as the median filter.

4.5 Conclusion

We have proposed a reconstruction method for images in sCT by using multi-energy information. For each energy band, we reconstruct the current image utilizing the images from the other energy bins. To do this, we first classify the similar pixels by the k-means algorithm. Then, we make linear adjustments between two images corresponding to two energy bins within each class. These linear adjustments are made two by two for all the images corresponding to all the energy bands, which leads, for a current (original) image to a given energy bin, to several other (estimated) images corresponding to the others energy bins. At the end, for each fixed pixel, a filtering (median) in the energy direction generates the final reconstructed image, which has a better quality. The results on both simulated and real data (physical phantom and rabbit) demonstrate the effectiveness of the proposed method, which shows better performance in terms of both reconstruction and decomposition of materials.

Chapter 5 Simultaneous reconstruction and denoising in sCT

Abstract

sCT based on photon-counting detectors offers the ability of obtaining CT images for different energy bins with a single X-ray excitation. The signal-to-noise ratio (SNR) of the reconstructed CT images at an energy bin is however drastically decreased. Firstly, we present a study of different reconstruction methods that integrate explicit denoising within each energy bin in the reconstruction. The sCT reconstruction is then formulated as an optimization problem, in which four popular denoising techniques, including guided filter, wavelet transform, nonlocal means, and block-matching and 3D filtering, are investigated and the split Bregman algorithm is utilized to accelerate convergence speed. The so-obtained simultaneous reconstruction and denoising methods are evaluated in terms of root mean square error (RMSE), SNR and material decomposition performance. Considering the relationship of the information for all the energy bins in sCT, the post-processing operator proposed in Chapter 4 is introduced in the process of simultaneous reconstruction and denoising. The results of this simultaneously reconstruction and denoising with intra- and inter-bin information show smaller RMSEs and higher SNRs while giving better performance in material decomposition, especially for the materials with K-edge.

5.1 Introduction

For CT reconstruction, there exist three main categories of methods: analytical, iterative and learning method. Filtered back projection (FBP) is the representative one of analytical methods, which has high speed but is sensitive to the projection dose and noise. Learning method requires large amount of data set, so it has limited application in sCT.

Despite their convergence speed, iterative methods, which allow for incorporating prior knowledge into reconstruction process, improve the reconstruction quality, reduce the dose and is more robust to noise. For these reasons, a large number of researches have been devoted to iterative methods for CT reconstruction, including the TV (Rudin, Osher, and Fatemi 1992), PRISM (Manley 2013), spectral mean (Zhang et al. 2016) and so on. Although these methods obtained better results than traditional analytical method, they have not considered explicit denoising in sCT reconstruction.

However, a typical limitation of sCT is that the number of photons available in each energy bin is much smaller than the total number of photons detected, thus resulting in the dramatically decreased signal-to-noise ratio (SNR) within each bin. In other words, noise is a major problem in sCT. Based on this remark, we propose to introduce explicitly denoising mechanism into reconstruction, thus leading to the so-called simultaneous reconstruction and denoising for sCT images. In this chapter, we propose to utilize the information within each energy bin and among all the other energy bins as regularization terms for simultaneous reconstruction and denoising.

5.2 Method

5.2.1 Intra-bin denoising

5.2.1.1 Model

A. Simultaneous reconstruction and denoising model with intra-bin information

As described in Chapter 2, sCT projections can be mathematically described as

$$Y = AU, \tag{5.1}$$

In the case of PCD-based sCT, the actual number of photons received by the detector is seriously influenced by noise obeying Poisson distribution. Therefore, iterative methods appear more appropriate for the reconstruction of sCT images by offering the possibility of introducing denoising mechanism in the reconstruction scheme. This leads to the following simultaneous reconstruction and denoising model

$$\min_U \frac{1}{2}\|Y - AU\|_2^2 + \frac{\lambda}{2}\|U - F_U\|_2^2, \tag{5.2}$$

where F_U represents the denoised term, λ is the parameters balancing the data fidelity term and the denoising term. In the following section, four popular denoising algorithms are introduced and compared.

After the above simultaneous reconstruction and denoising, the reconstruction is further refined by applying the same filtering F_U to the reconstructed image.

B. Intra-bin denoising filter

Intra-bin denoising aims to utilize the information within one energy bin to improve the reconstruction quality. The CT image for each energy bin is denoised independently. Therefore, all the denoising method for natural images could be applied to sCT.

The errors of reconstructed images come from two sources: sCT system and reconstruction algorithm. In general, there are three ways to denoise an image: spatial denoising, transform denoising and combined spatial and transform denoising. In the following, four popular denoising filters involving the three denoising approaches are introduced.

a. Guided Filter (GF)

Proposed by Kaiming et al. (Kaiming He 2012), GF is known for its speed and good performance. In our objective function, the guided image is the image itself, thus GF is equal to an edge-preserving filter. GF supposes that the pixels in a local region are linearly distributed. Therefore, linear fitting is used in a patch for denoising. In GF, $U_{\vec{x}}$, the estimated value at pixel $\vec{x}$, is the linear transform of the original $\mu_{\vec{x}}$ in a window w_p centered at the pixel p, namely

$$U_{\vec{x}} = a_p U_{\vec{x}} + b_p, \forall \vec{x} \in w_p , \quad (5.3)$$

where a_p, b_p are linear coefficients assumed to be constant in the window w_p, and can be calculated by linear regression. Because a pixel is included in several windows and each window has independent linear coefficients, the final estimated value is the weighted average of the linear transform of all the included windows.

b. Wavelet transform (WT)

Wavelet transform is one of the most typical methods in transform-domain image denoising. Based on the sparse representation of images, wavelet transform decomposes the original image into several bases with coefficients. The main information of the image concentrates on the bases with larger coefficients, while the bases with coefficients near zero are usually regarded as noise. Thus, wavelet denoising consists of three steps: wavelet transform to obtain the coefficients of each base, coefficients shrinking using thresholds for preserving main information and removing noise, inverse wavelet transform to get denoised image. The wavelet denoising can be mathematically expressed as

$$U = W^{-1} H W U , \quad (5.4)$$

where W denotes the orthonormal wavelet transform matrix, and H the diagonal shrink filter. In the present work, soft threshold is utilized to retain the coefficients of the bases.

c. Non Local Means (NLM)

NLM was proposed by Baudes et al.(Buades et al, Coll 2006), which exploits the similarity between the pixels of nonlocal regions to denoise. The idea is extended from the phenomenon that the more weighted images will result in better image quality. Thus, if more similar patches in the same image are utilized, the denoising performance will

be improved. Therefore, NLM filter utilizes the patch as the basic unit and searches similar patches in the whole image. The filter can be expressed as

$$U = \sum_{\vec{y}\in\Omega_{\vec{x}}} \omega(\vec{x},\vec{y})U_{\vec{y}}, \quad (5.5)$$

where $\omega(\vec{x},\vec{y})$ is the weight standing for the similarity of pixels $\vec{x}$ and $\vec{y}$ in the original image μ, which can be measured and regularized by the Euclidean metric between two patches centered at $\vec{x}$ and $\vec{y}$, and $\Omega_{\vec{x}}$ is the searching window centered at $\vec{x}$.

d. Block-matching and 3D filtering (BM3D)

Proposed by Kostadin et al. (Davob et al. 2007), BM3D algorithm deals with the simultaneous use of spatial and transform information. Based on an enhanced sparse representation in transform domain, by grouping similar patches in the image into 3D stack, collaborative filtering in the transform domain, and blending the stack to the original position, BM3D allows for the improvement of image quality in SNR while preserving image details.

5.2.1.2 Optimization

To accelerate the convergence speed, we use the split Bregman algorithm to optimize the objective function. By introducing the parameter d, the problem is transformed into

$$\min_U \frac{1}{2}\|Y-AU\|_2^2 + \frac{\lambda}{2}\|d\|_2^2 \ s.t.\ d = U - F_U, \quad (5.6)$$

Thus, the complete form of split Bregman iteration scheme is

$$\left(U^{i+1}, d^{i+1}\right) = \underset{U,d}{\operatorname{argmin}} \frac{\lambda}{2}\|d\|_2^2 + \frac{1}{2}\|Y-AU\|_2^2 + \frac{\gamma}{2}\|d-(U-F_U)-b\|_2^2, \quad (5.7)$$

$$b^{i+1} = b^i + U^{i+1} - F_U^{i+1} - d^{i+1}, \quad (5.8)$$

The original problem can the decomposed into two sub-problems and solved by alternating minimization

$$U^{i+1} = \underset{U}{\operatorname{argmin}} \frac{1}{2}\|Y-AU\|_2^2 + \frac{\gamma}{2}\|d^i-(U-F_U^i)-b^i\|_2^2, \quad (5.9)$$

$$d^{i+1} = \underset{d}{\operatorname{argmin}} \frac{\lambda}{2}\|d\|_2^2 + \frac{\gamma}{2}\|d-(U^{i+1}-F_U^{i+1})-b^i\|_2^2, \quad (5.10)$$

Derivative is utilized to update the parameters, namely

$$U^{i+1} = \left(A^TA+\gamma I\right)^{-1}\left(\gamma F_U^i + \gamma d^i - \gamma b^i + A^TY\right), \quad (5.11)$$

$$d^{i+1} = \gamma\left(U^{i+1} - F_U^{i+1} + b^i\right)/\left(\lambda+\gamma\right), \quad (5.12)$$

The process of the algorithem is summarized as follows.

Algorithm 5.1: Split Bregman for the simuteous intra-bin denoising and image reconstruction

Input: Y, A

Output: U

Initialize: set i=0, $U^0=\vec{0}$.

Repeat

Calculate $U^{i+1}=\left(A^TA+\gamma I\right)^{-1}\left(\gamma F_U^i+\gamma d^i-\gamma b^i+A^TY\right)$

Calculate $d^{i+1}=\gamma\left(U^{i+1}-F_U^{i+1}+b^i\right)/\left(\lambda+\gamma\right)$

Calculate $b^{i+1}=b^i+U^{i+1}-F_U^{i+1}-d^{i+1}$

i=i+1

Until *Converges*

5.2.2 Combined Intra- and inter-bin denoising

5.2.2.1 Model

As described in Chapter 4, the proposed post-processing method which employs the multi-energy in formation to denoise in each energy bin shows better performance compared with the original image. Therefore, it is utilized as a regularization term in the objective function for simultaneous reconstruction and denoising. The inter-bin denoisnig operator is expressed as

$$\min_U \frac{1}{2}\|U-L_U\|_2^2, \tag{5.13}$$

where L_U donates the post-processing operator introduced in Chapter 4. Thus, adding the intra- and inter-bin denoising operators to the objective function, this leads to the following simultaneous reconstruction and denoising model

$$\min_U \frac{1}{2}\|Y-AU\|_2^2+\frac{\lambda}{2}\|U-F_U\|_2^2+\frac{\rho}{2}\|U-L_U\|_2^2, \tag{5.14}$$

where λ and ρ are the parameters balancing the denoising term and fitting term.

5.2.2.2 Optimization

Same as simultaneous reconstruction and denoising with the intra-bin information, split Bregman algorithm is utilized to optimize the objective function. By introducing the parameter d_F and d_L, the problem is transformed into

$$\min_U \frac{1}{2}\|Y-AU\|_2^2+\frac{\lambda}{2}\|d_F\|_2^2+\frac{\rho}{2}\|d_L\|_2^2 \; s.t.\; d_F=U-F_U, d_L=U-L_U, \tag{5.15}$$

Thus, the complete form of split Bregman iteration scheme is

$$\begin{aligned}\left(U^{i+1},d_F{}^{i+1},d_L{}^{i+1}\right)=\arg\min_{U,d}\ &\frac{1}{2}\|Y-AU\|_2^2+\frac{\lambda}{2}\|d_F\|_2^2+\frac{\rho}{2}\|d_L\|_2^2\\&+\frac{\gamma}{2}\left\|d_F-\left(U-F_U\right)-b_F\right\|_2^2+\frac{\sigma}{2}\left\|d_L-\left(U-L_\mu\right)-b_L\right\|_2^2\end{aligned}, \tag{5.16}$$

$$b_F{}^{i+1}=b_F{}^i+U^{i+1}-F_U^{i+1}-d_F{}^{i+1}, \tag{5.17}$$

$$b_L^{i+1} = b_L^{\,i} + U^{i+1} - L_U^{i+1} - d_L^{\,i+1}, \tag{5.18}$$

The original problem can the decomposed into three sub-problems and solved by alternating minimization

$$U^{i+1} = \arg\min_U \frac{1}{2}\left\|Y - AU\right\|_2^2 + \frac{\gamma}{2}\left\|d_F^{\,i} - \left(U - F_U^i\right) - b_F^{\,i}\right\|_2^2 + \frac{\sigma}{2}\left\|d_L - \left(U - L_U\right) - b_L\right\|_2^2, \tag{5.19}$$

$$d_F^{\,i+1} = \arg\min_{d_F} \frac{\lambda}{2}\left\|d_F\right\|_2^2 + \frac{\gamma}{2}\left\|d_F - \left(U^{i+1} - F_U^{i+1}\right) - b_F^{\,i}\right\|_2^2, \tag{5.20}$$

$$d_L^{\,i+1} = \arg\min_{d_L} \frac{\rho}{2}\left\|d_L\right\|_2^2 + \frac{\sigma}{2}\left\|d_L - \left(U - L_U\right) - b_L\right\|_2^2, \tag{5.21}$$

Thus, the parameters are updated by the following equations

$$U^{i+1} = \left(A^T A + \gamma I + \sigma I\right)^{-1}\left[A^T Y + \gamma\left(F_U^i + d_F^{\,i} - b_F^{\,i}\right) + \sigma\left(L_U^i + d_L^{\,i} - b_L^{\,i}\right)\right], \tag{5.22}$$

$$d_F^{\,i+1} = \gamma\left(U^{i+1} - F_U^{i+1} + b_F^{\,i}\right)\Big/\left(\lambda + \gamma\right), \tag{5.23}$$

$$d_L^{\,i+1} = \sigma\left(U^{i+1} - L_U^{k+1} + b_L^{\,i}\right)\Big/\left(\rho + \sigma\right). \tag{5.24}$$

Thus, the optimization steps are described as follows:

Algorithm 5.2: Split Bregman for the simuteous denoising and image reconstruction

Input: Y, A

Output: U

Initialize: set i=0, $U^0 = \vec{0}$.

Repeat

Calculate $U^{i+1} = \left(A^T A + \gamma I + \sigma I\right)^{-1}\left[A^T Y + \gamma\left(F_U^i + d_F^{\,i} - b_F^{\,i}\right) + \sigma\left(L_U^i + d_L^{\,i} - b_L^{\,i}\right)\right]$

Calculate $d_F^{\,i+1} = \gamma\left(U^{i+1} - F_U^{i+1} + b_F^{\,i}\right)\Big/\left(\lambda + \gamma\right)$

Calculate $d_L^{\,i+1} = \sigma\left(U^{i+1} - L_U^{k+1} + b_L^{\,i}\right)\Big/\left(\rho + \sigma\right)$

Calculate $b_F^{\,i+1} = b_F^{\,i} + U^{i+1} - F_U^{i+1} - d_F^{\,i+1}$

Calculate $b_L^{\,i+1} = b_L^{\,i} + U^{i+1} - L_U^{i+1} - d_L^{\,i+1}$

i=i+1

Until *Converges*

5.3 Experiments and results

5.3.1 Results on simulation

5.3.1.1 Intra-bin reconstruction and denoising

The simulation phantom utilized is the same as that described in Chapter 3, with projection views as 300, tube current as 0.1 mA, tube voltage as 100 keV, and detector number as 700. The reconstructed image is of size 160×160, and the parameters λ, γ are set as 20 and 100, respectively. Taking the theoretical attenuation coefficients as reference, Figure 5.1 shows the reconstructed images and reconstruction errors, with different configurations: direct reconstruction without denoising, simultaneous reconstructions with GD, WT, NLM and BM3D. It is obvious that compared to direct reconstruction, artifacts are largely removed using simultaneous reconstruction and

denoising. Figure 5.2 illustrates the profiles of the reconstructed images for the energy bin 50-59keV in the red line in Figure 5.1, which also clearly demonstrates that the introduction of explicit denoising in the reconstruction yields the reconstructed images closer to the reference as well as smaller variances.

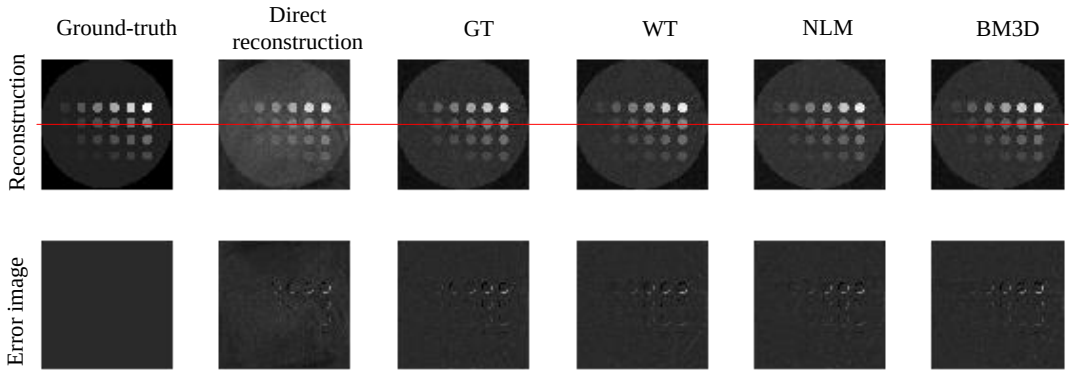

Figure 5.1 Reconstructed images (top row) and reconstruction errors (bottom row). From left to right: ground-truth, reconstruction without denoising, and reconstructions with GF, WT, NLM and BM3D, respectively.

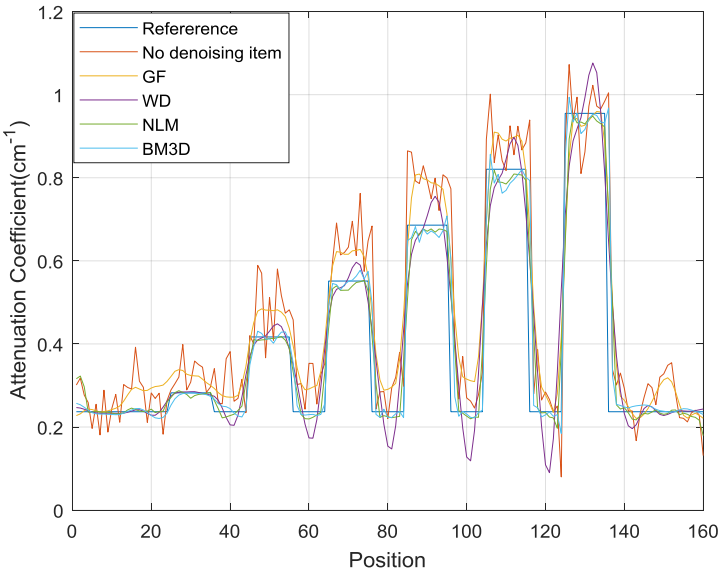

Figure 5.2 1D profiles along lines in Figure 5.1.

More quantitatively, Table 5.1 gives the RMSE and SNR values of images reconstructed without and with denoising. The results show that the simultaneous reconstruction and denoising methods achieve lower RMSEs and higher SNRs regardless of the used denoising techniques.

Table 5.1 RMSE and SNR of reconstructed images.

	Direct reconstruction	Simultaneous reconstruction and intra-bin denoising			
		GF	WT	NLM	BM3D
RMSE	0.0991	0.0707	0.0790	0.0692	0.0713
SNR(dB)	9.8028	13.5969	12.6393	13.7077	13.5551

We also compared different reconstruction methods in terms of material decomposition performance, namely fCT imaging, as shown in Figure 5.3. The used material decomposition method has been described in previous publication. The use of any of the above-described denoising techniques takes advantage over reconstruction directly and simply from sinogram, especially for PMMA and water, which have close attenuation coefficients.

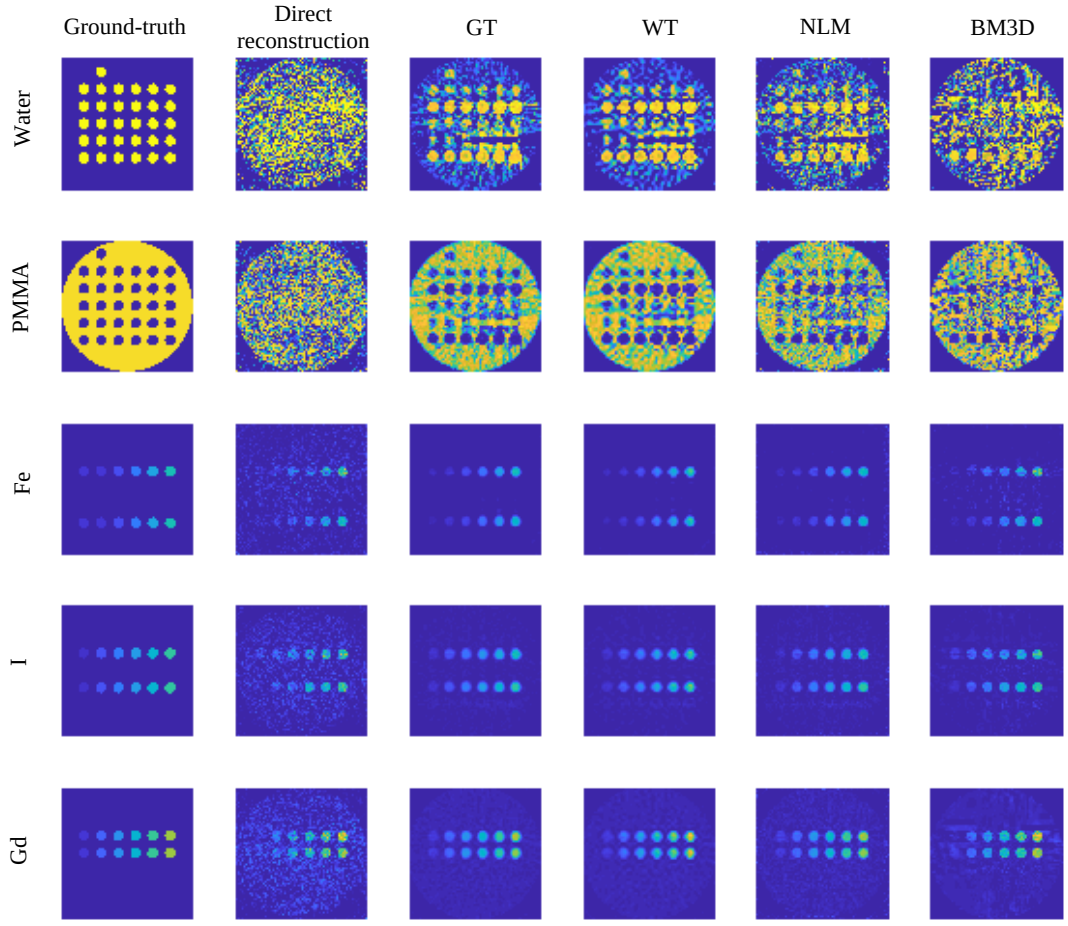

Figure 5.3 Comparison of different reconstruction methods in terms of material decomposition performance. From top to bottom: PMMA, Water, Fe, I and Gd. From left to right: ground-truth, direct reconstruction without denoising, simultaneous reconstruction and denoising with GF, WT, NLM and BM3D, respectively.

5.3.1.2 Combined inter- and intra-bin reconstruction and denoising

From the inter-bin denoising results, the results with NLM filters show better performances compared with the other three denoising filters. Thus, in this part,

reconstruction and denoising with combined intra- and inter-bin information just utilized the NLM for comparison. Also, considering the time efficiency of the calculation, the intra- and inter-bin reconstruction and denoising is cycled every five times in the experiment. That is to say, in five iterations, four are just the intra-bin operation, and one is intra- and inter-bin operation. The reconstructed image is still of size 160×160, and the parameters λ, ρ are set as 10 and 130, respectively. Figure 5.4 shows the reconstruction and error comparison for the energy bin 50-59keV on TV, reconstructions with NLM, and reconstruction with combined intra-bin NLM and inter-bin operation. It is observed that the method in our thesis has effective function on denoising, and at the same time conserves the edges compared with TV. The reconstruction with combined intra-bin NLM and inter-bin operation reduces the noise in the whole image, but it does not function as well as the reconstruction with NLM on the edges. Figure 5.5 illustrates the profiles of the reconstructed images for the energy bin 50-59keV in the red line in Figure 5.4, which also demonstratez that the reconstruction from our simultaneous reconstruction and denoising method is closer to the ground-truth as well as smaller variances, even though reconstruction from TV seems smoother.

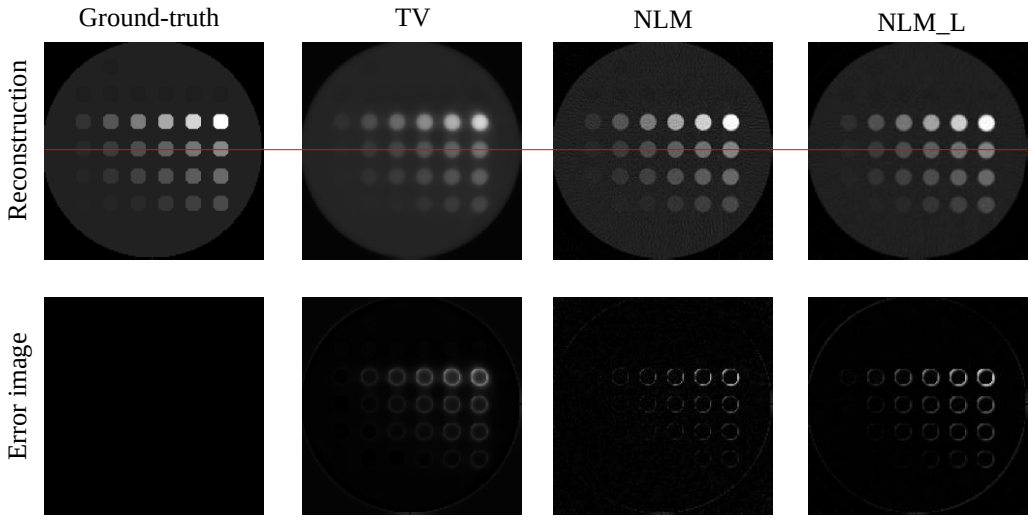

Figure 5.4 Reconstructed images (top row) and reconstruction errors (bottom row). From left to right: reference, TV, reconstructions with NLM, and reconstruction with combined intra-bin NLM and inter-bin operation, respectively.

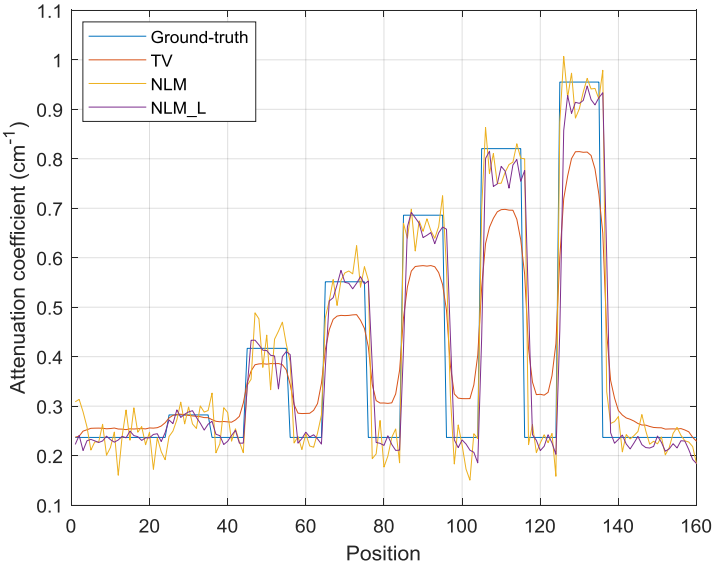

Figure 5.5 1D profiles along lines in Figure 5.4.

More quantitatively, Table 5.2 gives the RMSE and SNR values of reconstruction for comparison. The results show that the reconstruction with combined intra-bin NLM and inter-bin operation obtains the lowest RMSE and highest SNR compared with other methods.

Table 5.2 RMSEs and SNRs of reconstructed images for TV, reconstruction with NLM, and reconstruction with combined intra-bin NLM and inter-bin operation (NLM_L).

	TV	NLM	NLM_L
RMSE	0.0900	0.0692	0.0478
SNR(dB)	11.4790	13.7077	21.1451

Also, the material decomposition results for these methods are compared, as shown in Figure 5.6. As can be observed, although the decomposition results of our method are not as smooth as TV, they are closer to the ground-truth. The decomposition on the reconstruction images with combined intra-bin NLM and inter-bin operation reduce the noise globally, but for the material without K-edge, such as I, the results do not as good as the decomposition from reconstruction just with NLM.

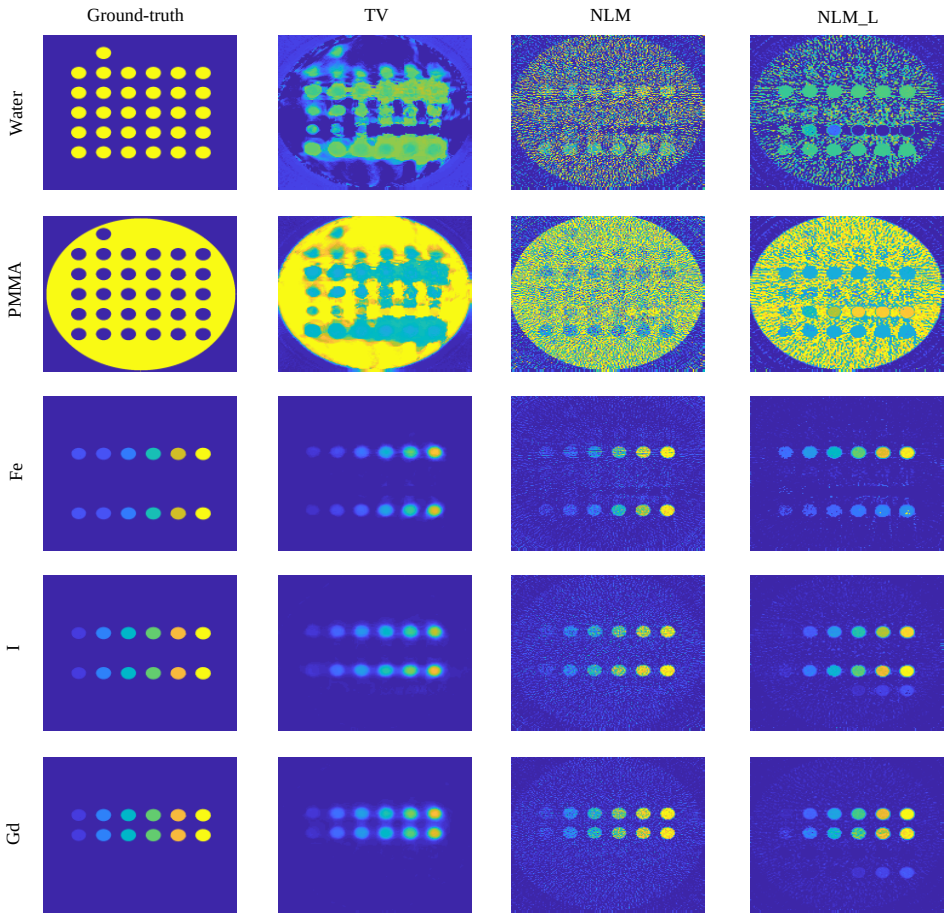

Figure 5.6 Comparison of different reconstruction methods in terms of material decomposition performance. From top to bottom: PMMA, Water, Fe, I and Gd. From left to right: ground truth, TV, reconstructions with NLM, and reconstruction with combined intra-bin NLM and inter-bin operation, respectively. The display scales have been normalized according to value range of the each material.

5.3.2 Results on physical phantom

To further evaluate the performance of the proposed simultaneous reconstruction and denoising method, we also made the same experiments on real data acquired using physical sCT. The used physical phantom is illustrated in Figure 3.8, which contains Gd, I, Water and PMMA with various concentrations. The scanning parameters were set the same as that described in Chapter 3, namely source voltage as 150 keV, which was divided into 5 bins: 27-47 keV, 48-58 keV, 59-68 keV, 69-79 keV, and 80-150 keV. The projection view is 600, and the detector number is 683. The image size is 320×320.

Figure 5.7 shows the reconstruction results from TV, reconstruction with NLM and and reconstruction with combined intra-bin NLM and inter-bin operation for this physical phantom. The display scales have been regularized according to the values of the image for each energy bin. It can be visually observed that NLM_L reduces the noise of reconstruction globally. Actually, it also change the values within each energy bin. As the physical data is heavily affected by the noise, this change is not obvious, but

it will have considerable influence on the image-domain material decomposition, which will be compared in the next paragraph.

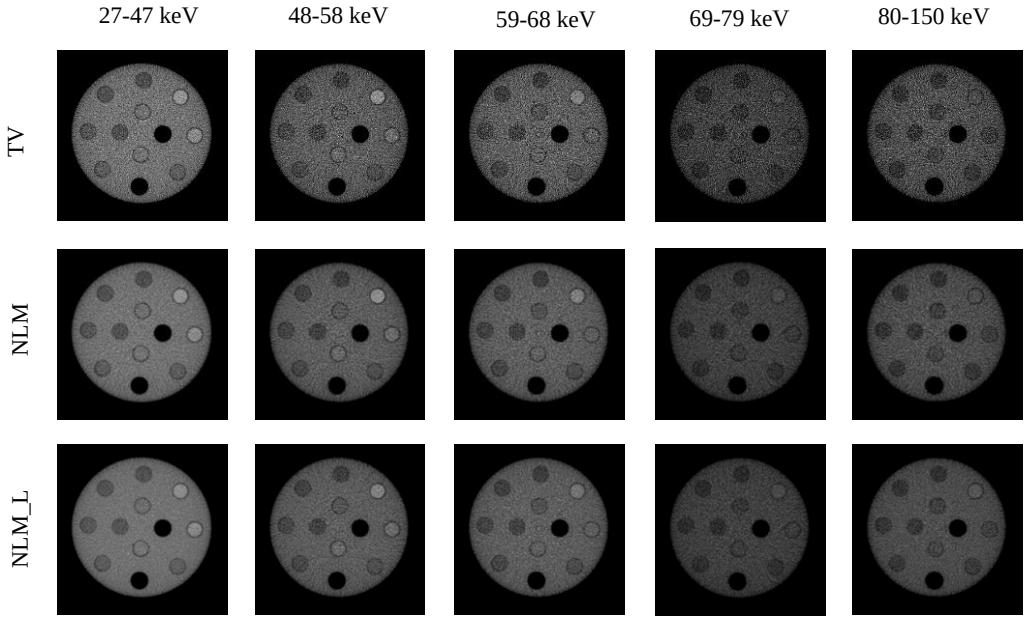

Figure 5.7 Reconstructed images for physical phantom. From left to right: TV, reconstructions with NLM, and reconstruction with combined intra-bin NLM and inter-bin operation, respectively.

More quantitatively, Table 5.3 gives the average CNRs and SNRs of ROIs (the disks) values of reconstruction for comparison, which was defined in Chapter 3. The results show that although all the reconstructions suffer in severe noise, our proposed methods still have higher CNR and SNR of ROIs.

Table 5.3 Average CNRs and SNRs of ROIs of reconstructed images for TV, reconstruction with NLM, and reconstruction with combined intra-bin NLM and inter-bin operation (NLM_L).

	TV	NLM	NLM_L
CNR	0.5141	0.7123	0.7012
SNR of ROI (dB)	1.5593	1.9971	2.0579

The material decomposition results for these methods are compared, as shown in Figure 5.8. As Water and PMMA are similar in the attenuation coefficient curve which make them difficult to separate in reality, and they are not medical interest in medical diagnosis, in the physical phantom, the decomposition just treat them into the same material, namely Water (or water-like more precisely). As can be observed, the physical material decomposition images suffer from serious noise. But the decomposition values from the reconstruction with combined intra-bin NLM and inter-bin operation are more close to the ground-truth, which meanwhile reduce the noise globally. Specially, the performance of Gd is more accurate than I, which is difficult to distinguish for all the methods.

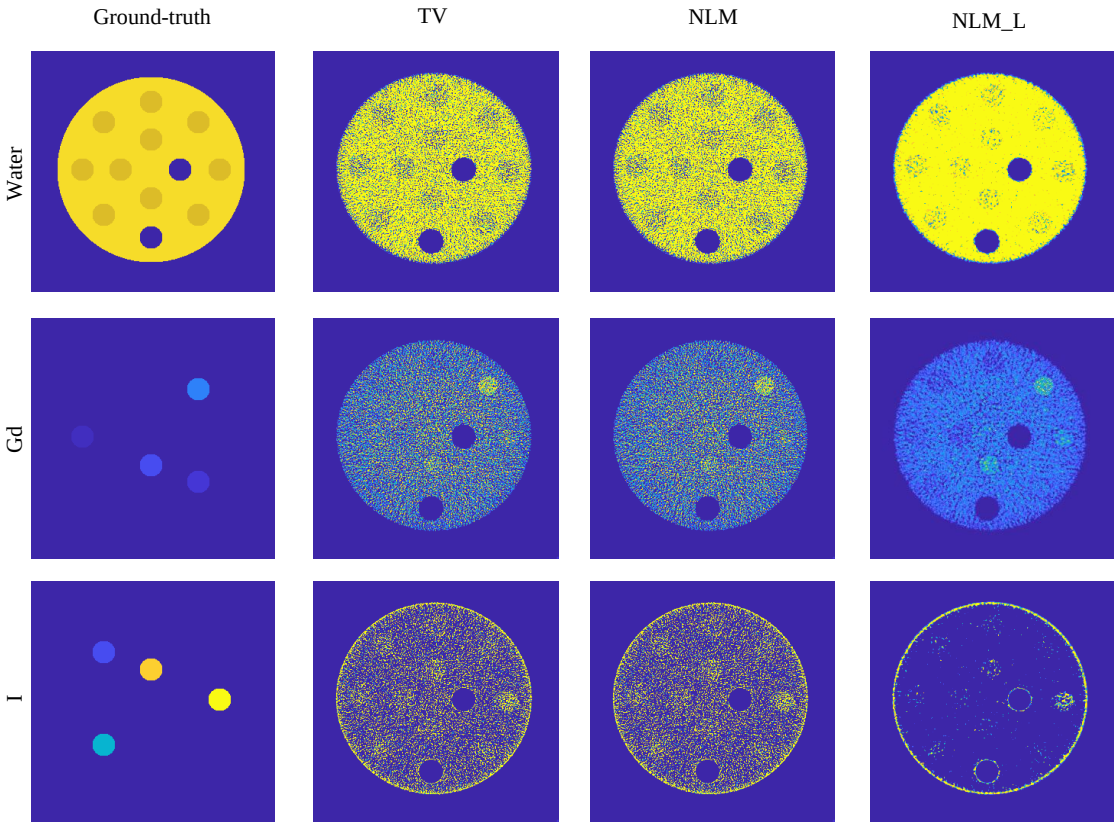

Figure 5.8 Comparison of different reconstruction methods in terms of material decomposition performance. From top to bottom: Water, Gd, and I. From left to right: ground truth, TV, reconstructions with NLM, and reconstruction with combined intra-bin NLM and inter-bin operation, respectively. The display scales have been normalized according to value range of the same material.

5.4 Discussion

We have proposed two simultaneous reconstruction and denoising method for sCT images. The results show that our method can not only improve the reconstruction image in reducing the RMSE and increasing the SNR, but also improve the accuracy of reconstruction-based material decomposition.

First, for the simultaneous reconstruction and denoising utilizing the intra-bin information, we explored the performance of four popular denoising methods, including the spatial method GF and NLM, transform method WT, mixed method BM3D. Their performances were evaluated using theoretical values, RMSE and SNR. The results show that with the combination of reconstruction and intra-bin denoising, the reconstructed images from sCT have smaller RMSEs, higher SNRs, and better performance in material decomposition. This model can also be applied to conventional CT.

For sCT, there exists relationship in the attenuation coefficient (namely the pixel values of the reconstruction) for each energy bin. As introduced in Chapter 4, the post-processing operation improves the image quality in sCT. Therefore, it is introduced as a

regularization term in the objective function for the simultaneous reconstruction and denoising. Thus, both the intra- and inter-bin information is utilized in the reconstruction. The results show that simultaneous reconstruction and denosing with the intra- and inter-bin information improves the RMSEs and SNRs of reconstruction, and has some improvement in the material decomposition, especial for the material with K-edge, such as Gd and I.

The results of reconstruction and material decomposition for physical phantom are not as good as those in simulations, which is mainly due to two reasons. Firstly, the projection views of the physical phantom are less. Compared with the physical data utilized in Chapter 4 which had 2400 projection views and 924 detectors, the data in this chapter were only 600 projection views and 643 detectors. The influences of these parameters on CT imaging have been discussed in Chapter 3. Secondly, the physical system suffers from more complex noise, such as the cross-talk and pile-up effect in the detectors, and the simulation only considers statistical noise. When the information is not large enough, the influence of the noise will be more evident.

This method also has its limitations. Although it improves the reconstructed quality globally, it often not work ideally in the edge. This is due to the cluster in the operation, in which step the edges are not always classified into the correct class. The wrong class will increase the errors of the values in the reconstruction, even if we have added the correction mechanism in the process. Therefore, some work to improve the processing of the edges is expected in the future.

The calculation efficiency is a nonnegative problem for this iterative method, which is mainly resulted from two sides. The first is the measurement data itself and the system matrix. In our experiment, for the physical data with 600 projection views and 643 detectors, if the size of the reconstruction image is 320×320, the sparse system matrix will be about 10 Gb. In the iteration process, it costs large space and long time for the calculation. Second, the parameters balancing the data fidelity term and regularization terms are selected through experiments, which also costs time to verify the performances.

In the material decomposition in simulation, the results from simultaneous reconstruction and denoisng utilizing intra- and inter-bin information are better than those from reconstruction with just intra-bin information in the materials Gd and I, which have K-edge, but not better in the materials without K-edge, such as Fe. This is explained by that the materials with K-edge as their characteristics are easier to distinguish and thus the inter-bin denoising operation is more functional on them. Thus, the improvement on the algorithm for the materials without K-edge is still a challenge in the future.

5.5 Conclusion

Firstly, we have proposed a simultaneous reconstruction and denoising method by the intre-bin information for sCT images. Four popular denoising methods, including the spatial method GF and NLM, transform method WT, mixed method BM3D, were

introduced in reconstruction. Their performances were evaluated using theoretical values, RMSE and SNR. Split Bregman algorithm was utilized to accelerate the convergence speed. The results of this method have smaller RMSEs, higher SNRs, and better performance in material decomposition.

Based on the above model, we introduced the post-processing operation in Chapter 4 into the objective function and built a simultaneous model of reconstruction and denoising utilizing both the intra- and inter-bin information. The results show better performances in the reconstruction and have some improvement in the image-based material decomposition, especially for the material with K-edge.

Conclusion and perspective

Conclusion

In this thesis, we attempt to explore the capabilities of sCT for potential applications and aim to acquire images from sCT with high quality. The main contributions of this thesis lie in the following three aspects: (1) we proposed to consider the ability of sCT to achieve simultaneously both aCT and fCT in one single acquisition through reconstruction and material decomposition; (2) we proposed a post-processing operation utilizing the multi-energy information to improve the image quality in sCT; (3) we proposed a simultaneous reconstruction and denoising method integrating the intra- and inter-bin information in sCT by iterative optimization.

Before presenting the achievements of this thesis, the basic principle of CT and sCT is introduced in Chapter 1. The most significant difference of conventional CT and sCT is the detectors equipped in the system (the former with the EIDs and the latter with the PCDs), which makes it possible to acquire more than two sets of measurement in one acquisition. This characteristic of sCT enables it to not only have the capability of reconstruction as the conventional CT, but also be utilized for material decomposition and image enhancement. Chapter 2 presents the reconstruction methods for sCT, including the analytical methods, iterative methods and learning methods. Each kind of method has its own advantages and shortcomings.

Acquainted with the general principles of sCT, we set up the present work following the above-mentioned three aspects:

- Multimodel imaging of sCT (Chapter 3).
  sCT has the multimodel imaging ability to achieve simultaneously both aCT and fCT in one single acquisition through reconstruction and material decomposition. aCT function of sCT is studied under the same configuration as that of conventional CT, and fCT function of sCT is investigated by applying material decomposition algorithms to the same acquired multi-energy data. In addition, the selection of energy bin number in the CT system is discussed to balance the quality of reconstruction and material decomposition.
- Reconstruction utilizing multi-energy information in sCT (Chapter 4).
  A post-processing operation which cooperates the relationship among each energy bin is proposed. This method projects several images for one energy bin from all the other energy bins and utilizes these projected images to improve the image quality. The method is validated on simulation, physical phantom and rabbit data to demonstrate its performance of reconstruction, monoE imaging and material decomposition imaging.
- Simultaneous reconstruction and denoising in sCT (Chapter 5).
  An iterative method integrating the denoising both within one energy bin and among all the energy bins is presented. The method is optimized by split

Bregman method, and validated on simulation and physical sCT by the performances of reconstruction and material decomposition.

Perspective

We have proposed the ability of sCT in multimodel imaging, and give quantitative comparison for the results. In addition, a post-processing operation is introduced by utilizing the multi-energy information, and is applied into the simultaneous reconstruction and denoising in sCT. Our experiments and methods also have some limitations.

- The limitation of the simulation.
  In the simulation, the measurements are added by Poisson noise to the ideal data. In practice, the CT system suffers from all kinds of noise, such as electronic noise for conventional CT, cross-talk and pile-up for sCT, which will all degrade their performance. These complex noises are difficult to model precisely. Thus, the simulation results have some differences with the physical CT. If conditions can be satisfied, the comparison between the aCT imaging of sCT and conventional CT can be made on physical CT system.
- The limitation of the phantom.
  The phantoms utilized in our experiment contain several regions with clear edges to the neighbours, and the concentration of the material within each region is averagely distributed. However, in the human body, the concentration of the materials usually vary gradually without clear bounds. In the future, more precise biological phantom can be developed for the research.
- The limitation of the post-processing operation.
  The key of the post-processing operation is to cluster pixels with similar attenuation characteristic into one class. The mistaken classified pixels will increase bring in errors to the results. Thus, choosing the proper features and stable clustering method are still the problems worth to further research.
- The limitation of the simultaneous reconstruction and denoising method.
  Time and space cost is still a significant consideration for this iterative method. The large space cost comes from two sources: the measurement for the sCT and the large system matrix. In the iterative process, the calculation also requires much time and space due to the large amount of data. In the future, more efficient ways can be developed to solve the inverse problem with multiple regularizations, such as decomposing the large data set into several ordered subsets, finding more proper optimization algorithms, and so on.

Therefore, several potential improvements can be carried out in the future, including more realistic noise in the simulation, more precise biological phantom, more accurate in the post-processing operation, and less time and space cost in the simultaneous reconstruction and denoising solution.

Publications

Journal article:

[1] P. Niu et al. “Simultaneous Multimodal Imaging Using Spectral Photon-Counting CT: a Simulation Study”, IEEE Transactions on Radiation and Plasma Medical Sciences (under review).

[2] P. Niu et al. “Image reconstruction using multi-energy information in spectral CT”, Medical Physics (to be summited).

[3] B. Xie, T. Su, V. Kaftandjian, P. Duvauchelle, P. Niu, M. Robini, Y. Zhu. Material Decomposition in X-ray Spectral CT Using Multiple Constraints in Image Domain[J]. Journal of Nondestructive Evaluation, 2019, 38(1): 16.

[4] B. Xie, T. Su, V. Kaftandjian, P. Duvauchelle, P. Niu, M. Robini, Y. Zhu, “ ROI-Wise Material Decomposition in Spectral Photon-Counting CT”, IEEE Transactions on Nuclear Science (under review).

Conferences:

[1] P. Niu, M. Robini, B. Xie, T. Su, V. Kaftandjian, F. Yang, Y. Zhu, P. Duvauchelle, “Simultaneous Reconstruction and Denoising of Spectral CT Images”, IEEE ICSP2018.

[2] M. Robini, P. Niu, F. Yang, Y. Zhu, “Image reconstruction by nonconvex inexact half-quadratic optimization”, Proc. IEEE—Nuclear Science Symposium and Medical Imaging Conference, 2017.

[3] B. Xie, T. Su, V. Kaftandjian, P. Duvauchelle, P. Niu, M. Robini, Y. Zhu, “Image Domain Local Joint Sparse Material Decomposition in Spectral CT”, iCT 2018.

Bibliography

Alvarez, Robert E. and Albert MacOvski. 1976b. “Energy-Selective Reconstructions in X-Ray Computerised Tomography.” *Physics in Medicine and Biology* 21(5):733–44.

Antoni Buades, Bartomeu Coll, Jean-Michel Morel. 2006. “A Non-Local Algorithm for Image Denoising.” *Proceedings - International Conference on Image Processing, ICIP* (0):1429–32.

Badea, Cristian T., Matthew Holbrook, and Darin P. Clark. 2018. “Multi-Energy CT Decomposition Using Convolutional Neural Networks.” (January 2019):59.

Beister, Marcel, Daniel Kolditz, and Willi A. Kalender. 2012. “Iterative Reconstruction Methods in X-Ray CT.” *Physica Medica* 28(2):94–108.

Birch, R. and M. Marshall. 1979. “Computation of Bremsstrahlung X-Ray Spectra and Comparison with Spectra Measured with a Ge(Li) Detector.” *Physics in Medicine and Biology* 24(3):505–17.

Bornefalk, Hans and Mats Danielsson. 2010. “Photon-Counting Spectral Computed Tomography Using Silicon Strip Detectors: A Feasibility Study.” *Physics in Medicine and Biology* 55(7):1999–2022.

Bouleti, Claire, Guillaume Baudry, Bernard Iung, Dimitri Arangalage, Jérémie Abtan, Gregory Ducrocq, Philippe Gabriel Steg, Alec Vahanian, Marie Cécile Henry-Feugeas, Nicoletta Pasi, Sylvie Chillon, Francesca Pitocco, Jean Pierre Laissy, and Phalla Ou. 2017. “Usefulness of Late Iodine Enhancement on Spectral CT in Acute Myocarditis.” *JACC: Cardiovascular Imaging* 10(7):826–27.

Buades, Antoni, Bartomeu Coll, Jean-michel Morel, and Jean-michel Morel A. 2010. “A Review of Image Denoising Algorithms , with a New One To Cite This Version :” 4(2):490–530.

Buzug, Thorsten. 2015. “Computed Tomography: From Photon Statistics to Modern Cone-Beam CT.” *Computed Tomography: From Photon Statistics to Modern Cone-Beam CT* 50(7):1–521.

Ch, Lucia B., Student Member, Leticia Ortega-m, and A. Mlem Reconstruction Method. 2015. “ML-EM Reconstruction Model Including Total Variation for Low Dose PET High Resolution Data.” (656).

Chambolle, Antonin and Pierre Louis Lions. 1997. “Image Recovery via Total Variation Minimization and Related Problems.” *Numerische Mathematik* 76(2):167–88.

Chen, Hu, Yi Zhang, Yunjin Chen, Junfeng Zhang, Weihua Zhang, Huaiqiang Sun, Yang Lv, Peixi Liao, Jiliu Zhou, and Ge Wang. 2018. “LEARN: Learned Experts’ Assessment-Based Reconstruction Network for Sparse-Data CT.” *IEEE Transactions on Medical Imaging* 37(6):1333–47.

Chen, Hu, Yi Zhang, Weihua Zhang, Peixi Liao, Ke Li, Jiliu Zhou, and Ge Wang. 2017. “Low-Dose CT via Convolutional Neural Network.” *Biomedical Optics Express* 8(2):679.

Chen, Yang, Luyao Shi, Qianjing Feng, Jian Yang, Huazhong Shu, Limin Luo, Jean Louis Coatrieux, and Wufan Chen. 2014. “Artifact Suppressed Dictionary Learning for Low-Dose CT Image Processing.” *IEEE Transactions on Medical Imaging* 33(12):2271–92.

Chun, Se Young, Yuni K. Dewaraja, and Jeffrey A. Fessler. 2014. “Alternating Direction Method of Multiplier for Tomography with Nonlocal Regularizers.” *IEEE Transactions on Medical Imaging* 33(10):1960–68.

Chun, Se Young, Kyeong Yun Kim, Jae Sung Lee, and Jeffrey A. Fessler. 2016. “TOF-PET USING ALTERNATING DIRECTION METHOD OF MULTIPLIER Ulsan National Institute of Science and Technology (UNIST) Seoul National University , ‡ University of Michigan - Ann Arbor.” (1):86–89.

Clark, Darin P. and Cristian T. Badea. 2014. “Spectral Diffusion: An Algorithm for Robust

Material Decomposition of Spectral CT Data." *Physics in Medicine and Biology* 59(21):6445–66.

Dac, Multi-bit A. X., Noise Shaping, and Dynamic Elements. 1997. "Dual-Energy (Spectral) CT: Applications in Abdominal Imaging." (2):1712–13.

Davob, Kostadin, Alessandro Foi, Vladimir Katkovnik, and Karen Egiazarian. 2007. "Image Denoising by Sparse 3-D Transform-Domain Collaborative Filtering." *IEEE Transactions on Image Processing* 16(8):1–2.

Duan, Xinhui, Jia Wang, Shuai Leng, Bernhard Schmidt, Thomas Allmendinger, Katharine Grant, Thomas Flohr, and Cynthia H. McCollough. 2013. "Electronic Noise in CT Detectors: Impact on Image Noise and Artifacts." *American Journal of Roentgenology* 201(4):626–32.

Duvauchelle, Philippe, Nicolas Freud, Valérie Kaftandjian, and Daniel Babot. 2000. "A Computer Code to Simulate X-Ray Imaging Techniques." *Nuclear Instruments and Methods in Physics Research, Section B: Beam Interactions with Materials and Atoms* 170(1):245–58.

Faby, Sebastian, Stefan Kuchenbecker, David Simons, Heinz-Peter Schlemmer, Michael Lell, and Marc Kachelrieß. 2014. "CT Calibration and Dose Minimization in Image-Based Material Decomposition with Energy-Selective Detectors." *Medical Imaging 2014: Physics of Medical Imaging* 9033(6221):903318.

Fletcher, Joel G., Lifeng Yu, Leng Shuai, and Cynthia H. McCollough. 2015. "Dual- and Multi-Energy CT: Principles, Technical Approaches, and Clinical Applications." *Radiology* 276(3):637–53.

Foygel Barber, Rina, Emil Y. Sidky, Taly Gilat Schmidt, and Xiaochuan Pan. 2016. "An Algorithm for Constrained One-Step Inversion of Spectral CT Data." *Physics in Medicine and Biology* 61(10):3784–3818.

Gordon, Richard, Robert Bender, and Gabor T. Herman. 1970. "Algebraic Reconstruction Techniques (ART) for Three-Dimensional Electron Microscopy and X-Ray Photography." *Journal of Theoretical Biology* 29(3):471–81.

Graser, Anno, Thorsten R. C. Johnson, Hersh Chandarana, and Michael Macari. 2009. "Dual Energy CT: Preliminary Observations and Potential Clinical Applications in the Abdomen." *European Radiology* 19(1):13–23.

Gravel, Pierre, Gilles Beaudoin, and Jacques A. De Guise. 2004. "A Method for Modeling Noise in Medical Images." *IEEE Transactions on Medical Imaging* 23(10):1221–32.

Greenspan, Hayit, Bram Van Ginneken, and Ronald M. Summers. 2016. "Guest Editorial Deep Learning in Medical Imaging: Overview and Future Promise of an Exciting New Technique." *IEEE Transactions on Medical Imaging* 35(5):1153–59.

Gullberg, Grant, Rolf Clackdoyle, Grant Gullberg, and Rolf Clackdoyle. 2009. "医学图像重建入门_曾更生着(中文版)."

Gupta, Harshit, Kyong Hwan Jin, Ha Q. Nguyen, Michael T. McCann, and Michael Unser. 2018. "CNN-Based Projected Gradient Descent for Consistent CT Image Reconstruction." *IEEE Transactions on Medical Imaging* 37(6):1440–53.

Han, Yo Seob, Jaejun Yoo, and Jong Chul Ye. 2016. "Deep Residual Learning for Compressed Sensing CT Reconstruction via Persistent Homology Analysis."

Hanson, Kenneth M. 1981. "Noise and Constrast Discrimination in Computed Tomography." 5(1):3941–55.

Hsieh, Jiang. 1998. "Adaptive Streak Artifact Reduction in Computed Tomography Resulting from Excessive X-Ray Photon Noise." *Medical Physics* 25(11):2139–47.

Hsieh, Jiang. 2009. *Computed Tomography: Principles, Design, Artifacts, and Recent Advances, 2nd Edition*. Vol. 1.

Hubbell J H, Seltzer S. M. 1995. *Tables of X-Ray Mass Attenuation Coefficients and Mass Energy-Absorption Coefficients 1 KeV to 20 MeV for Elements Z= 1 to 92 and 48*

Additional Substances of Dosimetric Interest. Gaithersburg, MD (United States).

Iwanczyk, J. S., E. Nygård, O. Meirav, J. Arenson, W. C. Barber, N. E. Hartsough, N. Malakhov, and J. C. Wessel. 2007. "Photon Counting Energy Dispersive Detector Arrays for X-Ray Imaging." 2741–48.

Jin, Kyong Hwan, Michael T. McCann, Emmanuel Froustey, and Michael Unser. 2017. "Deep Convolutional Neural Network for Inverse Problems in Imaging." *IEEE Transactions on Image Processing* 26(9):4509–22.

Jing Wang, Tianfang Li, Hongbing Ly, Zhengrong Liang. 2006. "Penalized Weighted Least-Squares Approach to Sinogram Noise Reduction and Image Reconstruction for Low-Dose X-Ray Computed Tomography." *IEEE Trans Med Imaging* 25(10):1272–83.

Johnson, Thorsten R. C., Bernhard Krauß, Martin Sedlmair, Michael Grasruck, Herbert Bruder, Dominik Morhard, Christian Fink, Sabine Weckbach, Miriam Lenhard, Bernhard Schmidt, Thomas Flohr, Maximilian F. Reiser, and Christoph R. Becker. 2007. "Material Differentiation by Dual Energy CT: Initial Experience." *European Radiology* 17(6):1510–17.

Kaiming He. 2012. "Guided Image Filtering." *IEEE Transactions on Pattern Analysis and Machine Intelligence* 35(6):1397–1409.

Karçaaltincaba, Muşturay and Aykut Aktaş. 2011. "Dual-Energy CT Revisited with Multidetector CT: Review of Principles and Clinical Applications." *Diagnostic and Interventional Radiology* 17(3):181–94.

Katsuyuki, Taguchi and Iwanczyk Jan S. 2013. "Vision 20/20: Single Photon Counting X-ray Detectors in Medical Imaging." *Medical Physics* 40(10):100901.

Kazantsev, Daniil, Jakob S. Jørgensen, Martin S. Andersen, William R. B. Lionheart, Peter D. Lee, and Philip J. Withers. 2018. "Joint Image Reconstruction Method with Correlative Multi-Channel Prior for x-Ray Spectral Computed Tomography." *Inverse Problems* 34(6).

Le, Huy Q. and Sabee Molloi. 2011. "Least Squares Parameter Estimation Methods for Material Decomposition with Energy Discriminating Detectors." *Medical Physics* 38(1):245–55.

Lee, Tae Hwan and Byung Cheol Song. 2011. "De-Noising Algorithm Using Sparse 3D Transform-Domain Collaborative Filtering and Adaptive Soft Thresholding." *Proceedings of the International Symposium on Consumer Electronics, ISCE* 16(8):128–31.

Li, Si. 2016. "Reducing Staircasing Artifacts in SPECT Reconstruction by an Infimal Convolution Regularization." m(November).

Li, Zhoubo, Shuai Leng, Lifeng Yu, Armando Manduca, and Cynthia H. McCollough. 2017. "An Effective Noise Reduction Method for Multi-Energy CT Images That Exploit Spatio-Spectral Features." *Medical Physics* 44(5):1610–23.

Li, Zhoubo, Shuai Leng, Lifeng Yu, Zhicong Yu, and Cynthia H. McCollough. 2015. "Image-Based Material Decomposition with a General Volume Constraint for Photon-Counting CT." *Medical Imaging 2015: Physics of Medical Imaging* 9412:94120T.

Liu, Xuejin, Mats Persson, Hans Bornefalk, Staffan Karlsson, Cheng Xu, Mats Danielsson, and Ben Huber. 2016. "Errata: Spectral Response Model for a Multibin Photon-Counting Spectral Computed Tomography Detector and Its Applications." *Journal of Medical Imaging* 3(4):049801.

Luo, Jianhua. 2010. "Reconstruction from Limited-Angle Projections Based on Spectrum Analysis." 19:131–40.

Luo, Jianhua, Jiahai Liu, Wanqing Li, and Yuemin Zhu. 2012. "Image Reconstruction from Sparse Projections Using S-Transform." 227–39.

M, Buzug T. 2008. "Computed Tomography: From Photon Stastics to Modern Cone-Beam CT." *Springer Science & Business Media*.

Macovski, A., R. E. Alvarez, J. L. H. Chan, J. P. Stonestrom, and L. M. Zatz. 1976. "Energy Dependent Reconstruction in X-Ray Computerized Tomography." *Computers in Biology and Medicine* 6(4):325–36.

Mallinson, Paul I., Chris Stevens, Clemens Reisinger, Savvas Nicolaou, Peter L. Munk, and Hugue Ouellette. 2013. "Achilles Tendinopathy and Partial Tear Diagnosis Using Dual-Energy Computed Tomography Collagen Material Decomposition Application." *Journal of Computer Assisted Tomography* 37(3):475–77.

Manley, Gerard. 2013. "Multi-Energy CT Based on a Prior Rank, Intensity and Sparsity Model (PRISM)." 27(11):1–30.

Marshall, W. H., R. E. Alvarez, and A. Macovski. 2014. "Initial Results with Prereconstruction Dual-Energy Computed Tomography (PREDECT)." *Radiology* 140(2):421–30.

Mechlem, Korbinian, Sebastian Ehn, Thorsten Sellerer, Eva Braig, Daniela Münzel, Franz Pfeiffer, and Peter B. Noël. 2018. "Joint Statistical Iterative Material Image Reconstruction for Spectral Computed Tomography Using a Semi-Empirical Forward Model." *IEEE Transactions on Medical Imaging* 37(1):68–80.

Morrison, Robert and Dan Mccammon. 1983. "Interstellar Photoelectric Absorption Cross Sections, 0.03-10 KeV." (1973):119–22.

Nien, Hung and Jeffrey A. Fessler. 2014. "A Convergence Proof of the Split Bregman Method for Regularized Least-Squares Problems." 1–11.

Noh, Joonki, Jeffrey A. Fessler, and Paul E. Kinahan. 2009. "Statistical Sinogram Restoration in Dual-Energy CT for PET Attenuation Correction." *IEEE Transactions on Medical Imaging* 28(11):1688–1702.

Palareti, G., C. Legnani, B. Cosmi, E. Antonucci, N. Erba, D. Poli, S. Testa, and A. Tosetto. 2016. "Comparison between Different D-Dimer Cutoff Values to Assess the Individual Risk of Recurrent Venous Thromboembolism: Analysis of Results Obtained in the DULCIS Study." *International Journal of Laboratory Hematology* 38(1):42–49.

Patel, Anish A., Patrick D. Sutphin, Yin Xi, Suhny Abbara, and Sanjeeva P. Kalva. 2019. "Arterial Phase CTA Replacement by a Virtual Arterial Phase Reconstruction from a Venous Phase CTA: Preliminary Results Using Detector-Based Spectral CT." *CardioVascular and Interventional Radiology* 42(2):250–59.

Persson, Mats, Ben Huber, Staffan Karlsson, Xuejin Liu, Han Chen, Cheng Xu, Moa Yveborg, Hans Bornefalk, and Mats Danielsson. 2014. "Energy-Resolved CT Imaging with a Photon-Counting Silicon-Strip Detector." *Physics in Medicine and Biology* 59(22):6709–27.

Rigie, David S. and Patrick J. La Rivière. 2015. "Joint Reconstruction of Multi-Channel, Spectral CT Data via Constrained Total Nuclear Variation Minimization." *Physics in Medicine and Biology* 60(5):1741–62.

Rigie, David S., Adrian A. Sanchez, and Patrick J. La Rivière. 2015. "Joint Reconstruction of Multi-Channel, Spectral CT Data via Constrained Total Nuclear Variation Minimization Related Content Assessment of Vectorial Total Variation Penalties on Realistic Dual-Energy CT Data." *Phys. Med. Biol* 60:1741.

La Rivière, Patrick J. 2005. "Penalized-Likelihood Sinogram Smoothing for Low-Dose CT." *Medical Physics* 32(6):1676–83.

Roessl, E. and R. Proksa. 2007. "K-Edge Imaging in x-Ray Computed Tomography Using Multi-Bin Photon Counting Detectors." *Physics in Medicine and Biology* 52(15):4679–96.

Rudin, Leonid I., Stanley Osher, and Emad Fatemi. 1992. "Nonlinear Total Variation Based Noise Removal Algorithms." *Physica D* 60:259–68.

Schirra, Carsten O., Bernhard Brendel, Mark A. Anastasio, and Ewald Roessl. 2014. "Spectral CT: A Technology Primer for Contrast Agent Development." *Contrast Media and Molecular Imaging* 9(1):62–70.

Shikhaliev, Polad M. 2012. "Photon Counting Spectral CT: Improved Material Decomposition with K-Edge-Filtered x-Rays." *Physics in Medicine and Biology* 57(6):1595–1615.

Shikhaliev, Polad M., Tong Xu, and Sabee Molloi. 2005. "Photon Counting Computed Tomography: Concept and Initial Results." *Medical Physics* 32(2):427–36.

Sidky, Emil Y. and Xiaochuan Pan. 2008. “Image Reconstruction in Circular Cone-Beam Computed Tomography by Constrained, Total-Variation Minimization.” *Physics in Medicine and Biology* 53(17):4777–4807.

Sukovic, P. and N. H. Clinthorne. 2002. “Penalized Weighted Least-Squares Image Reconstruction for Dual Energy X-Ray Transmission Tomography.” 19(11):23/16,-23/20.

Sukovle, P. and N. H. Clinthorne. 2003. “Basis Material Decomposition Using Triple-Energy X-Ray Computed Tomography.” 1615–18.

Symons, Rolf, Tyler E. Cork, Manu N. Lakshmanan, Robert Evers, Cynthia Davies-Venn, Kelly A. Rice, Marvin L. Thomas, Chia Ying Liu, Steffen Kappler, Stefan Ulzheimer, Veit Sandfort, David A. Bluemke, and Amir Pourmorteza. 2017. “Dual-Contrast Agent Photon-Counting Computed Tomography of the Heart: Initial Experience.” *International Journal of Cardiovascular Imaging* 33(8):1253–61.

Taguchi, Katsuyuki, Eric C. Frey, Xiaolan Wang, Jan S. Iwanczyk, and William C. Barber. 2010. “An Analytical Model of the Effects of Pulse Pileup on the Energy Spectrum Recorded by Energy Resolved Photon Counting X-Ray Detectors.” *Medical Physics* 37(8):3957–69.

Taguchi, Katsuyuki, Mengxi Zhang, Eric C. Frey, Jingyan Xu, W. Paul Segars, and Benjamin M. W. Tsui. 2007. “Image-Domain Material Decomposition Using Photon-Counting CT.” *Medical Imaging 2007: Physics of Medical Imaging* 6510(1):651008.

Tan, Shengqi, Yanbo Zhang, Ge Wang, Xuanqin Mou, Guohua Cao, Zhifang Wu, and Hengyong Yu. 2015. “Tensor-Based Dictionary Learning for Dynamic Tomographic Reconstruction.” *Physics in Medicine and Biology* 60(7):2803–18.

Ting, Su. 2019. “Quantitative Material Decomposition Methods for X-Ray Spectral CT To Cite This Version : HAL Id : Tel-01897337 Quantitative Material Decomposition Methods for X-Ray Spectral CT Méthodes de Décomposition Quantitative Des.”

Wang, Ge. 2016. “A Perspective on Deep Imaging.” *IEEE Access* 4:8914–24.

Willemink, Martin J., Mats Persson, Amir Pourmorteza, Norbert J. Pelc, and Dominik Fleischmann. 2018. “Photon-Counting CT: Technical Principles and Clinical Prospects.” *Radiology* 289(2):293–312.

Xie, Bingqing, Ting Su, Valérie Kaftandjian, Pei Niu, Feng Yang, Marc Robini, Yuemin Zhu, and Philippe Duvauchelle. 2019. “Material Decomposition in X-Ray Spectral CT Using Multiple Constraints in Image Domain.” *Journal of Nondestructive Evaluation* 38(1).

Xu, Cheng, Mats Danielsson, and Hans Bornefalk. 2011. “Evaluation of Energy Loss and Charge Sharing in Cadmium Telluride Detectors for Photon-Counting Computed Tomography.” *IEEE Transactions on Nuclear Science* 58(3 PART 1):614–25.

Zhang, Yanbo, Xuanqin Mou, Ge Wang, and Hengyong Yu. 2017. “Tensor-Based Dictionary Learning for Spectral CT Reconstruction.” *IEEE Transactions on Medical Imaging* 36(1):142–54.

Zhang, Yi, Yan Xi, Qingsong Yang, Wenxiang Cong, Jiliu Zhou, and Ge Wang. 2016. “Spectral CT Reconstruction with Image Sparsity and Spectral Mean.” *IEEE Transactions on Computational Imaging* 2(4):510–23.

FOLIO ADMINISTRATIF

THESE DE L'UNIVERSITE DE LYON OPEREE AU SEIN DE L'INSA LYON

NOM : NIU
(avec précision du nom de jeune fille, le cas échéant)

DATE de SOUTENANCE : 24/03/2020

Prénoms : Pei

TITRE : Multi-energy image reconstruction in spectral photon-counting CT

NATURE : Doctorat

Numéro d'ordre : 2020LYSEI022

Ecole doctorale : E.E.A. (Électronique, Électrotechnique, Automatique)

Spécialité : Traitement du Signal et de l'Image

RESUME :

Le scanner CT spectral à comptage de photons (sCT) est apparu récemment comme une nouvelle technique d'imagerie présentant des avantages fondamentaux par rapport au scanner CT classique et au scanner CT à double énergie. Cependant, en raison du nombre réduit de photons dans chaque bande d'énergie du scanner sCT et des artéfacts divers, la reconstruction des images devient particulièrement difficile. Cette thèse se concentre sur la reconstruction d'images multi-énergie en sCT. Tout d'abord, nous proposons d'étudier la capacité du scanner sCT à réaliser simultanément une imagerie anatomique (aCT) et fonctionnelle (fCT) en une seule acquisition par reconstruction et décomposition des matériaux. La fonction aCT du scanner sCT est étudiée dans la même configuration que celle du scanner CT classique, et la fonction fCT du scanner sCT est étudiée en appliquant des algorithmes de décomposition de matériaux aux mêmes données multi-énergie. Ensuite, comme le bruit est un problème particulièrement aigu en raison du nombre largement réduit de photons dans chaque bande d'énergie du scanner sCT, nous introduisons un mécanisme de débruitage dans la reconstruction de l'image pour effectuer simultanément un débruitage et une reconstruction. Enfin, pour améliorer la reconstruction de l'image, nous proposons de reconstruire l'image à une bande d'énergie donnée en exploitant les informations dans toutes les autres bandes d'énergie. La stratégie clé de cette approche consiste à regrouper les pixels similaires issus de la reconstruction de toutes les bandes d'énergie en une seule classe, à les ajuster dans la même classe, à projeter les résultats de l'ajustement dans chaque bande d'énergie, et à débruiter les informations projetées. Elle est utilisée à la fois comme une opération post-débruitage pour démontrer son efficacité et comme un terme de régularisation ou un terme de régularisations combinées pour la réalisation simultanée du débruitage et de la reconstruction. Toutes les méthodes ci-dessus sont évaluées sur des données de simulation et des données réelles provenant d'un scanner sCT préclinique.

MOTS-CLÉS : X-ray computed tomography, Spectral photon-counting CT, anatomical CT, functional CT, reconstruction, denoising.

Laboratoire (s) de recherche : Centre de Recherche en Acquisition et Traitement de l'Image pour la Santé (CREATIS), CNRS UMR 5220, INSERM U1206.

Directeur de thèse: Yuemin ZHU

Président de jury : KAFTANDJIAN Valérie

Composition du jury: HELBERT David (Rapporteur), DESVIGNES Michel (Rapporteur), USSON Yves (Examinateur), KAFTANDJIAN Valérie (Examinatrice), DUVAUCHELLE Philippe (Examinateur), ZHU Yuemin (Directeur de thèse)